Iris Biomechanics in Health and Disease

A DISSERTATION

SUBMITTED TO THE FACULTY OF THE GRADUATE SCHOOL

OF THE UNIVERSITY OF MINNESOTA

BY

Rouzbeh Amini

IN PARTIAL FULFILLMENT OF THE REQUIREMENTS

FOR THE DEGREE OF

DOCTOR OF PHILOSOPHY

Victor H. Barocas, Adviser

June 2010

Acknowledgment

I do not think that I could ever ask for a better or kinder adviser. During the past five years, Victor Barocas has been a great mentor and a good friend to me. He has given me freedom to explore, experience, and learn independently but he has never been far nor afraid to step in when I needed his help and mentorship. My desire to pursue an academic career in research and teaching has been definitely influenced by the amazing experience that I have had with him. I keenly look forward to having Victor as my colleague in the future. *VB, Gratias multas! Tu es optimus!*

Barocas lab members have made my PhD experience an exceptional one. Devesh Amatya, Ram Balachandran, and Eric Huang made it an easier transition for me in the beginning. Mike Evans, Triantafyllos Stylianopoulos, and Masano Sugiyama have done much to help me and I consider them among my dearest friends. Ed Sander has never hesitated to say "yes" when I asked him for help. My first-two-year officemate, Kunlun Liu and I shared many wonderful moments discussing mathematics and fluid dynamics. My other officemate Julie Whitcomb, who is as equally excited about ocular biomechanics as I am, has undoubtedly contributed to my success as a graduate student and has shared in much laughter and fun. Julie is a brilliant scientist and a great friend. The wonderful undergraduate students, Alina Oltean and Tracy Powell, who assisted me in my research, are smart, hardworking, and ambitious individuals. Ramesh Raghupathy and new members of the group, Faisal Hadi, Sara Jouzdani, Victor Lai, and Spencer Lake

are all intelligent and friendly people and are always ready to help. Their presence makes for a healthy and educational working environment.

Bob Tranquillo, as the head of the department of biomedical engineering, along with other faculty members have substantially contributed to the excellence and wellbeing of graduate students. I would particularly like to thank Bob for giving me an opportunity to teach the undergraduate course of programming for biomedical engineers. It was a thrilling experience.

I would also like to thank my PhD committee members, Allison Hubel, Vincent Barnett, Mary Lawrence, and John Bischof for their help and support during the past five years. Vincent's extensive knowledge of physiology and his innovative experimental techniques were essential for me in completing my doctoral work.

Finally, I want to thank my loving family. My parents and my two brothers have always been there for me. I know how happy they are with every successful step that I take. In fact, whatever success that I have is theirs. I am who I am because of their encouragement and tirelessness. I love them all dearly. The person who deserves my utmost gratitude is my wife Jessica Brioso. She has endured a lot during these past years. I thank her for all those days that I worked late and she would kindly pick me up. I thank her for listening to my practice presentations and proofreading my drafts. I thank her for tolerating my frustration when my code was not working and I especially thank her for answering any research-related biology, physiology, and/or pharmacology questions that I have had with knowledge and excitement. I love her with all my heart.

Abstract

Computational models of the eye have been studied by various investigators. The main purpose of developing a computational model is to provide a better understanding of the normal function of the eye as well as the abnormalities causing ocular diseases. For instance, by using computational methods, new insights have been brought to the pathophysiology and anatomical risk factors of angle-closure glaucoma, a mysterious eye disease closely related to the mechanics of the iris. Unlike the clinical research, computational studies are neither hindered by experimental difficulties nor by patient health risks.

We developed computational models of the ocular tissues at three different levels to understand the mechanisms by which ocular globe deformation, iris-aqueous-humor interaction, and detailed iris structure affect the iris configuration. These models include

- A finite-element model of the whole ocular globe consisting of the iris, cornea, sclera, and limbus
- A finite-element model of iris-aqueous-humor interaction in the anterior eye
- A finite element model of the iris with its active (dilator muscle) and passive (stroma) constituent tissues.

Our whole-globe simulation showed that corneoscleral indentation, a diagnostic and/or treatment method in various glaucoma-related complications, would lead to changes in the anterior chamber angle. Our model showed that the limbus, due to its unique mechanical properties, plays an important role in the deformation of the whole ocular globe. Simulations performed using our anterior-segment model showed that the rapid changes (~ sec) in the iris-aqueous-humor system due to corneoscleral indentation may lead to long recovery times (~ min). We showed that a similar long recovery mechanism prevents the iris from drifting forward during normal blinking. Finally, simulations based on the detailed iris anatomy showed that the posterior location of the dilator muscle could contribute to the iris anterior bowing following dilation even in the absence of the aqueous humor pressure difference.

Clinical studies have emphasized the key role of the iris shape and configuration in physiology and pathophysiology of the eye. In the work, we showed that iris configuration is ultimately affected by many parameters including deformation of the whole ocular globe, interaction with aqueous humor flow, and activation of its constituent muscles.

List of Tables

List of Figures

Chapter 1: Introduction

Glaucoma is a leading cause of blindness and affects millions of people worldwide. It is estimated that by 2020, there will be 79.6 million people worldwide with glaucoma, 11.2 million of them be bilaterally blind [1]. In spite of much study, the mechanisms leading to the onset of glaucoma remain poorly understood. As stated by Epstein [2]:

> *The study of glaucoma can be both clinically satisfying and intellectually stimulating. Yet it is also the most humbling of the disciplines, both because of our clinical failures but even more, our lack of real understanding. In truth, if one looks at ophthalmic knowledge in the last century, the field of glaucoma has shown the least progress.*

Part of this difficulty lies in the complex behavior of the tissues that make up the eye. Computational models provide a new way to study the complicated interactions between the ocular tissues, and they easily lend themselves to simulating abnormalities associated with glaucoma. A better understanding of the physiology of the eye and the pathophysiology of glaucoma provided by such models can be used to better design animal and/or human studies. They can also provide new insights to assess safety and

efficacy of current therapeutic and diagnostic techniques and lay the groundwork for future developments.

Three mathematical models were designed in the current research to answer some of glaucoma-related question. The iris, which plays an important role in certain types of glaucoma, is a major component of all models in the current study. In a first model, the importance of ocular globe deformation in relation to the iris and the intraocular pressure was studied (Chapter 2 and 3). A second model was further developed explore aqueous-humor-iris interaction (Chapter 4 and 5). Finally, a third model was created to study detailed structure of the iris (Chapter 6). The models along with additional experimental studies produced interesting results presented in this thesis.

1.1.Anatomy and physiology of the Eye

The human eye is a complex and interesting organ that has been subject of much study by a wide range of engineers in various fields such as optics, ocular imaging, ocular biomechanics and biotransport, and ocular tissue engineering. In this section, we present a brief introduction to ocular anatomy and physiology necessary for understanding of the mathematical models.

The human ocular globe is roughly spherical (Figure 1.1). The pressure inside the eye or, intraocular pressure (IOP), is slightly higher than the outside pressure. A positive IOP is important for the eye to maintain its shape and normal function. The mechanical

strength of the globe is provided by the corneoscleral shell composed of the sclera, cornea, and limbus (Figure 1.1). A plane, approximately passing through the ocular lens and limbus and perpendicular to the corneal axis, divides the ocular globe into two sections: anterior segment and posterior segment (Figure 1.1).

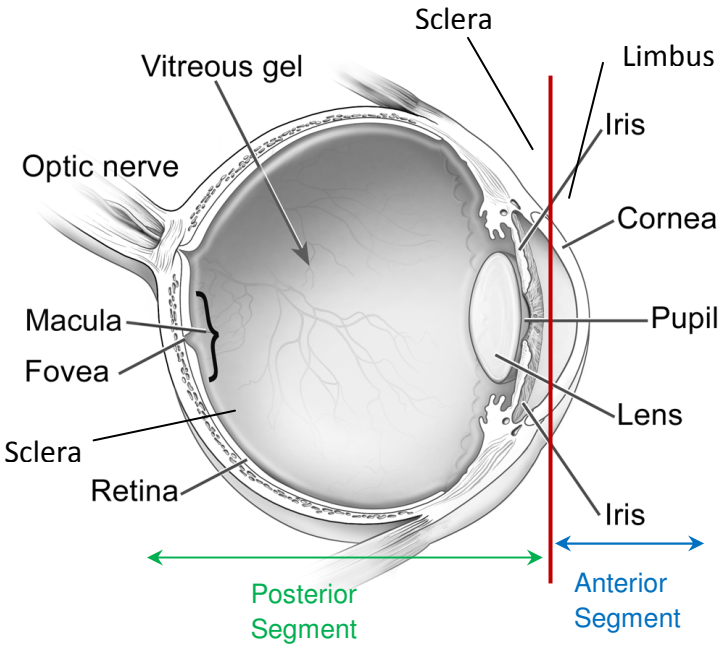

Figure 1.1 Anatomy of the eye composed of the anterior and posterior segments (image courtesy: National Eye Institute, NIH, Bethesda, MD).

The posterior segment includes a clear gel-like structure known as the vitreous humor and a solid section composed of the retina, choroid, sclera and optic nerve. The visual cells are located on the retina which is covered by the choroid, a thin layer consisting of the blood vessels that provide the visual cells with nutrients and oxygen. The sclera encapsulates the choroid and extends from the optic nerve to the cornea. Highly compacted bundles of collagen fibers make the sclera a mechanically strong structure.

The anterior segment is bounded by the lens and cornea. The cornea, similar to the sclera, is composed of the collagen fibers. The cornea, however, is clear and avascular. Similar to the cornea, the lens is also avascular and clear. Positioned posterior to the iris, the lens refracts the light entering the eye to create images on the retina.

The anterior segment is further divided to anterior and posterior chambers by the iris and pupil (Figure 1.2). The iris, which is composed of smooth muscle, controls the amount of light passing through the lens by changing the diameter of the pupil.

In the following sections a more detailed overview of anatomy, physiology, and mechanical properties of the ocular tissues are discussed.

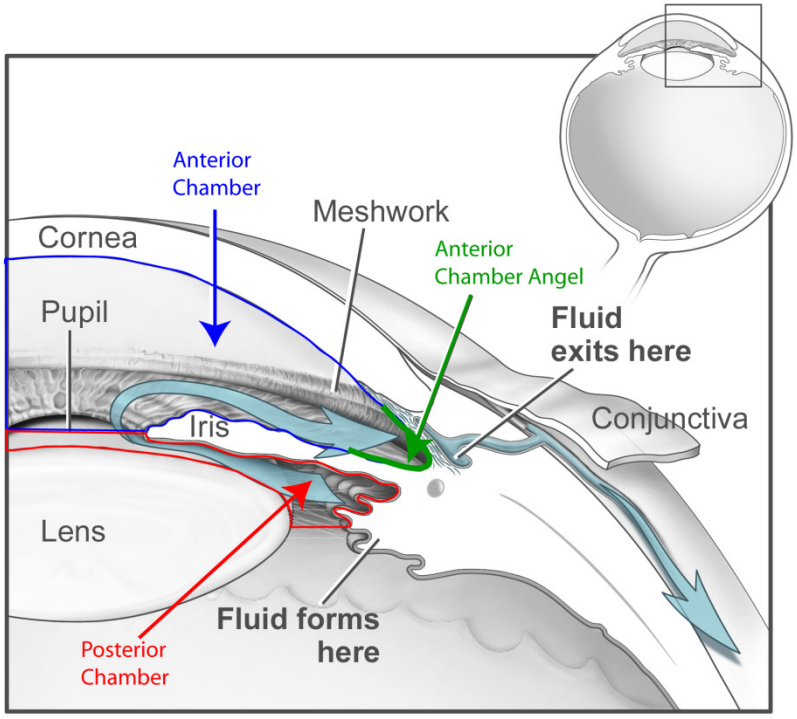

Figure 1.2 Anatomy of the anterior segment and flow of aqueous humor (image courtesy: National Eye Institute, NIH, Bethesda, MD).

1.1.1. Cornea

The cornea is the transparent tissue comprising almost one-six of the outer tunic of the eye. The anterior corneal surface, with approximately 48 diopters of refractive power, is the major component of ocular optic function in producing images on the retina. The cornea is roughly elliptical, with the average horizontal and vertical diameters of 12.8 mm and 11.7 mm, respectively. It has an average radius of curvature of 7.8 mm. The central portion of the cornea is thinner (0.52 mm) compared to its periphery (0.65 mm) [3].

The cornea is composed of six layers as shown in Figure 1.3. The remarkable transparency and mechanical strength of the cornea are due to the highly organized collagen fibers in the corneal stroma [4,5], accounting for approximately 90% of the corneal thickness [6]. The tightly-packed type I and V heterotypic collagen fibrils [7], comprising the stroma, are similar in thickness (between 22.5 and 32 nm) [3]. They are preferentially oriented in the meridional, horizontal, and circumferential directions [8]. The resultant is a transparent and mechanically strong tissue capable of bearing membrane loads due to IOP.

At the larger scale, the cornea protects the eye from external mechanical and chemical insults. As shown by numerous experimental studies [9-16], the cornea is anisotropic, viscoelastic, and highly nonlinear. An approximate elastic modulus of the cornea is calculated to be 19.1 MPa [9,10].

1.1.2. Sclera

The sclera is the white fibrous tissue that encapsulates most of the eye. It is roughly spherical with the average radius of curvature of 12.5 mm [17-19]. The scleral thickness changes along the anterior-posterior axis of the eye. It is thicker in the regions near the optic nerve head (1 mm [20,21]) and near the limbus (0.65 mm [20]) in comparison to the region near the equator (0.5 mm [20]).

The sclera is composed of circumferentially oriented Type I and III collagen fibers [22]. The fibers, unlike those in cornea, vary in width and have an irregular arrangement

leading to lack of transparency in the sclera. At the macroscale, the mechanical behavior of the sclera is viscoelastic, anisotropic, and nonlinear [22-24]. The average value of the scleral Young modulus measured experimentally is within the range of 5-13 MPa [22,25].

The optic nerve cells leave the eye from a mesh like structure, namely the lamina cribrosa, located at the posterior sclera, and form the optic nerve head. The biomechanics of the optic nerve head has been the subject of many studies [26] .

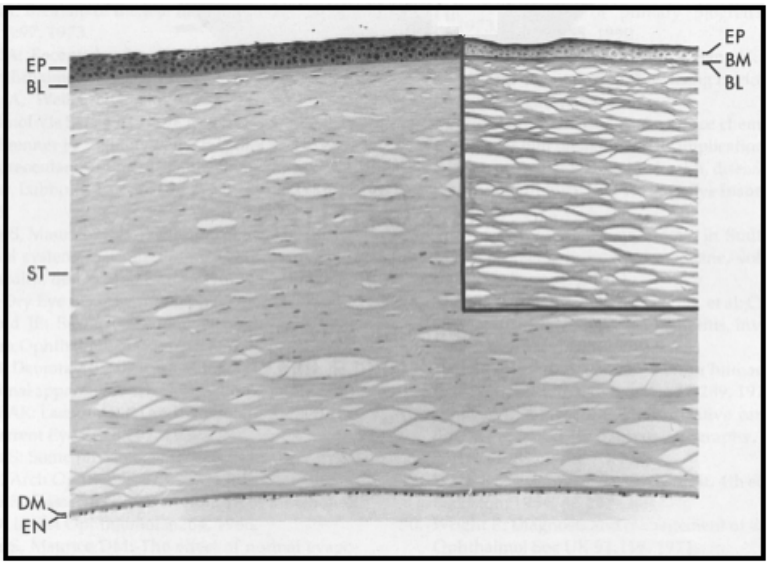

Figure 1.3 Histological cross-section of the human cornea showing its six comprising layers: epithelium (EP), basement membrane (BM), Bowman's layer (BL), stroma (ST), Descemet's membrane (DM), and endothelium (EN) (Image from Ref. [3] with permission).

1.1.3. Limbus

The limbus forms the boundary between the cornea and the sclera. X-ray scattering experiments [27] have shown that the preferred orientation of the collagen in the limbal region is circumferential. The microstructural anisotropy of the limbus is the cause of interesting mechanical behavior of the limbus observed experimentally [28-30]. The average elastic moduli of the limbal region, measured from the ocular globe inflation tests, are 3.4-13.1 MPa in the meridional direction and 5.92-27.5 MPa in the circumferential direction [10].

1.1.4. Iris

The iris is responsible for controlling the pupil diameter in response to changes in the ambient light. The iris is located anterior to the lens and posterior to the cornea. Its thickness varies from 372 ± 58 μm at the iris root to 645 ± 103 μm at its thickest point within the pupillary margin [31].

The iris is comprised of two smooth muscles: the *Sphincter Iridis* and the *Dilator Pupillae* (Figure 1.4). The sphincter and dilator muscle fibers are aligned in the circumferential and radial directions, respectively. The contraction and relaxation of the iris muscles controls the pupil diameter from 1mm at the complete pupil constriction to 9mm at the complete pupil dilation. Both muscles are enervated via autonomic nervous system [32].

Passive tensile tests on the bovine iris [33] have shown that it behaves in an elastic and incompressible manner up to 20% strain. The elastic modulus of 27 kPa in the radial direction is calculated from the bovine experiments. The radial elastic modulus of 24.7 kPa is also calculated from porcine irides inflation tests [34].

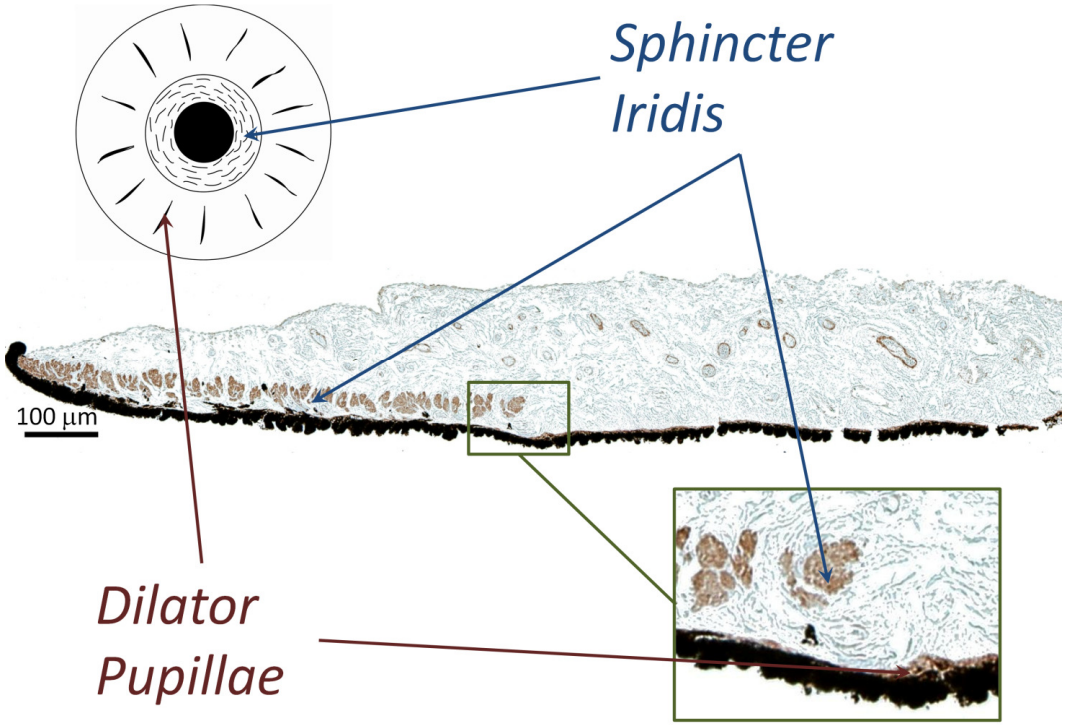

Figure 1.4 Histological cross-section of the porcine iris showing its three comprising segments: active smooth muscles-the *Sphincter Iridis* and the -along with the passive iris stroma (histology image is from Julie E Whitcomb)

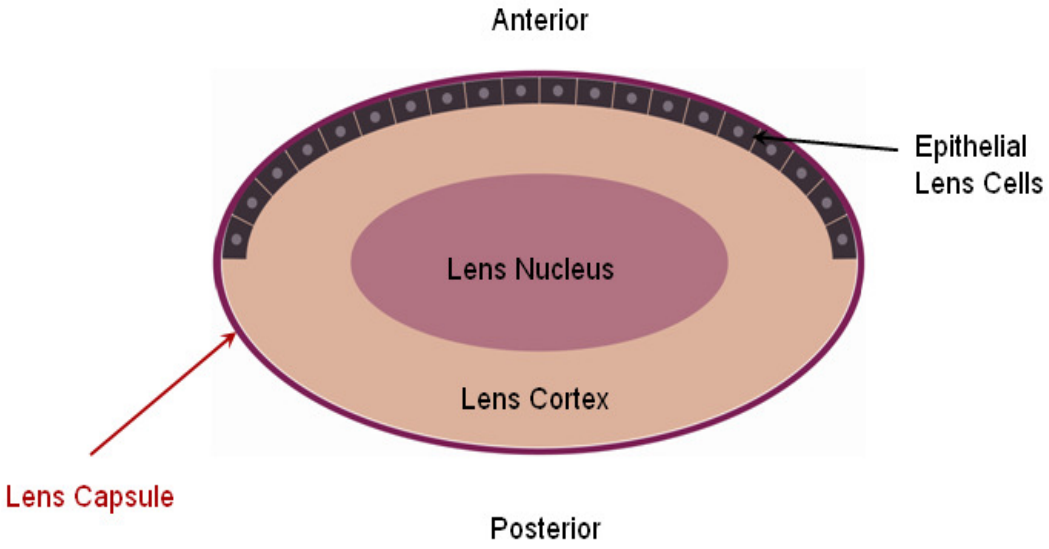

Figure 1.5 Schematic of different components comprising the lens.

It should be noted, however, that recent clinical observations indicate that activation of dilator muscle changes the cross-sectional area and the total volume of the iris [35,36]. In addition, ex vivo pharmacological and electrical stimulation of the iris has shown that the mechanical stiffness of the iris is subjected to significant changes following iris smooth muscle activation [37,38].

1.1.5. Lens

The ocular lens is located posterior to the iris and pupil. The major role of the ocular lens is to focus light on the retina and create a clear image. The refraction index of the lens is related to the curvature of the anterior and posterior surfaces of the lens. The posterior lens has a smaller radius of curvature (between 4.5 and 7.5 mm) in comparison to the anterior surface (between 8 and 14 mm) [39]. The equatorial diameter of the lens is approximately 9 mm in adults with a minimal change with the age [39]. The lens thickness, however, increases by 0.02 mm each year [39]. The

distance along the corneal axis between the anterior surface of the lens and the cornea, also known as the anterior chamber depth, is approximately 3 mm [40,41].

To create a clear image on the retina, the ocular refractive power needs to be adjusted based on the distance of the target objects from the cornea. The phenomenon of adjusting the refractive power is defined as accommodation and is mediated by changing the position and curvature of the ocular lens. The lens is kept in its position by the zonular fibers, which connect the outer layer of the lens to the ciliary muscles (section 1.1.7). During accommodation, contraction of the ciliary muscle reduces the tensile strain on the zonular fibers which consequently changes the location and curvature of the lens. [39,42-44].

The lens capsule (Figure 1.5) is composed of mainly type IV collagen. Mechanical properties of the lens capsule have been measured using various experimental techniques such as ring pulling [45], strip pulling [46], and controlled inflation [47]. A summary of these methods is presented in Table 1.1. A new method of measuring lens capsule mechanical properties by using osmotic swelling is presented in Appendix B.

Table 1.1 Comparison of the experimental studies of the lens capsule

Investigator	Tissue tested	Methods	Modulus of elasticity
Fisher 1967 [48]	Human lens	Anterior surface of the lens capsule, clamped in a glass apparatus, was pressurized from one side. The relation between the pressure and shell-like displacement was studied.	2-6 MPa
Krag and Andreassen 2003 [45]	Porcine lens	A ring made of the posterior lens capsule was uniaxially stretched by two mechanical pins. Modulus of elasticity was obtained from the stress-strain.	0.3-2.3 MPa
Wollensak *et al.* 2004 [46]	Porcine lens	A strip of the lens was clamped between two jaws and uniaxially stretched. The stress-strain curve was obtained.	3.2-12 MPa
Danielsen 2004 [49]	Rat, bovine, porcine, and human lens	Anterior surface of the lens capsule clamped in a glass apparatus was pressurized from one side. The relation between the pressure and shell-like displacement was studied.	Rat 0.54-23 MPa Cow 1.2-0.35 MPa Sow 1.26-38 MPa Human 2.4-9.9 MPa
Heistand *et al.* 2005 [47]	Porcine lens	The lens capsule was expanded by the injection of an isotonic solution. The deformation was reconstructed from the projected view of two cameras taking pictures from two different angles. The pressure-strain curves were obtained.	0.45 MPa†

† The value is approximated from Heistand's data and pressure vessel theory.

1.1.6. Aqueous humor flow

The aqueous humor flows constantly from the posterior chamber into the anterior chamber in order to bring oxygen and nutrients for the avascular ocular tissues, notably the cornea and lens. The aqueous humor, which is 98% water, carries electrolytes, oxygen, glucose, lactate, and various amino acids. The absence of large molecules in the aqueous humor makes it a transparent colorless medium between the cornea and the lens [50].

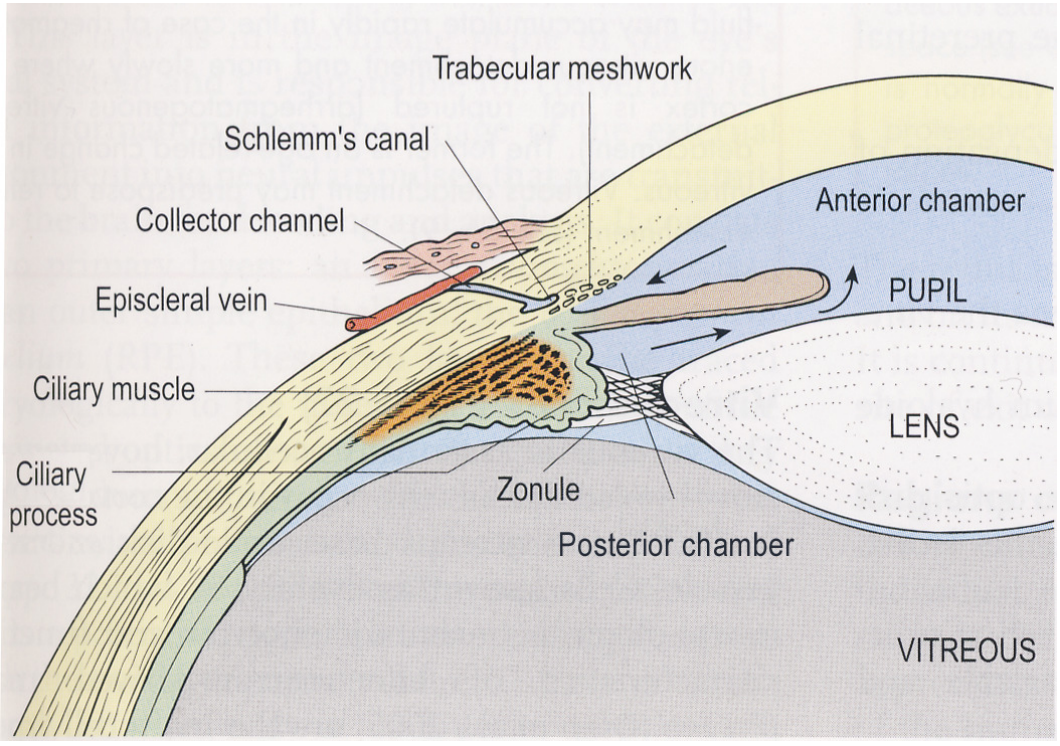

Figure 1.6 Schematic of the anterior segment showing the ciliary body and trabecular meshwork (image modified from Ref.[51] with permission).

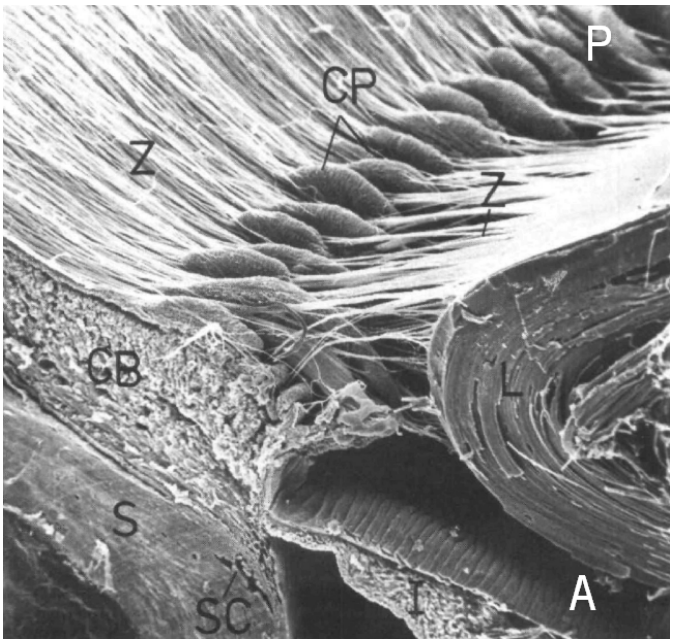

Figure 1.7 Scanning electron microscopy of the anterior segment of a monkey eye showing the zonular fibers (Z), ciliary processes (CP) , ciliary body (CB), sclera (S), Schlemms canal (SC), iris (I), and lens(L). Anterior-posterior directions are marked on the picture by A and P (image from Ref. [44] with permission (Association for Research in Vision and Ophthalmology as the copyright holder is acknowledged)).

The pathway of the aqueous humor is shown in Figure 1.2. The aqueous humor is secreted from the ciliary body into the posterior chamber. It then flows around the lens and through the iris-lens gap into the anterior chamber. The aqueous humor drains into the venous circulation system mostly via trabecular meshwork (section 1.1.8), located between the cornea and iris, and later through the Schlemm's canal. Since the aqueous humor is composed 98% from water, its viscosity and density are similar to those of water [52,53].

Not only does the flow of the aqueous humor provide the avascular tissues with oxygen and nutrients, but resistance to this flow also generates the intraocular pressure

(IOP). The dominant resistance to the flow is caused by outflow pathway (trabecular meshwork). The normal IOP of approximately 15 mmHg (2100 Pa) [54] is essential for the proper shape and optical functions of the eye globe.

1.1.7. Ciliary body

The ciliary body is a 5-6 mm wide ring-like tissue which is attached to sclera along the inner wall of the posterior chamber (Figure 1.6) [51]. The largest mass of ciliary body is the ciliary smooth muscle [50]. The contraction and relaxation of the ciliary smooth muscle is important in the process of accommodation. When ciliary muscle is relaxed, the zonular fibers are more stretched and the lens is flattened. A flatter lens has a smaller refractive index. When the ciliary muscle contracts, it moves inward and forward and consequently reduces some of the zonular fiber tension. Less stretched fibers lead to a less flattened lens and higher refractive power [43,44].

The other comprising section of the ciliary body is the ciliary process, a highly involuted tissue (Figure 1.7). Every single process is about 1 mm high, 2 mm long, and 0.5 mm wide [55]. The main function of the ciliary processes is aqueous humor formation. The ciliary processes produce aqueous humor and secrete it into the posterior chamber with approximate rate of 1.5-3 μL/min [56,57].

Three mechanisms have been proposed for aqueous humor secretion from the epithelial cells on the ciliary processes: diffusion, ultrafiltration, and active transport. Diffusion is highly unlikely as the solute contents of aqueous humor and cell plasma do

not create a favorable concentration gradient for the diffusion process [58,59]. Ultrafiltration has held by some to be responsible for up to 70% of aqueous humor formation [60-62]. There are, however, multiple reasons that ultrafiltration is not the dominant mechanism of aqueous humor formation:

- Inhibiting the active mechanism of aqueous humor formation leads to substantial reduction in aqueous humor formation [63-65]. Had ultrafiltration been the major contributor to aqueous humor formation, the change from turning off the active transport would not have been significant.
- Changes in the systemic blood pressure do not alter aqueous formation rate significantly [66].
- The capillary pressure necessary for the proposed formation rate of aqueous humor due to ultrafiltration should be 49-57 mmHg [60] much larger than values of 25-33 mmHg measured experimentally [64,67].

It is now widely accepted [50,68] that the active transport mediated by Na^+/K^+ ATPase pumps on the epithelial cell membrane of the ciliary processes is responsible for 70-80% of aqueous humor formation. Over a reasonable range of IOP, the aqueous humor formation rate is constant [69]. There, however, exists pseudofacility, a decrease in aqueous inflow with increased IOP [70,71].

1.1.8. Trabecular meshwork

The trabecular meshwork is located at the periphery of the anterior chamber, near the apex of the anterior chamber angle, the angle between the posterior cornea and anterior iris. The trabecular meshwork is the principal aqueous humor outflow pathway. It provides the aqueous humor with a passage from the anterior chamber to the Schlemm's canal, and mediates its final return to the circulatory system via the episcleral veins (Figure 1.6 and 1.7) [72]. The outflow rate via the trabecular mesh work is defined by [57,72]:

$$Q = \mu(P - P_e) \tag{1.1}$$

with Q being the outflow rate, μ being the aqueous humor outflow facility, P being the intraocular pressure, and P_e being the episcleral venous pressure. Typical values of μ and P_e are 0.25 μL/min/mmHg [56,57,73] and 9 mmHg [57,74], respectively.

The second principal pathway of the aqueous humor drainage from the anterior chamber is the uveoscleral outflow. The uveoscleral flow is defined as the outflow of the aqueous humor via intermuscular space of the ciliary muscle at the iris root at the anterior chamber apex [75]. At the normal levels of IOP, the uveoscleral flow accounts for 10% of the total outflow and, unlike trabecular meshwork outflow, is not sensitive to IOP changes [75,76] .

Figure 1.8 Normal (a) versus glaucomatous (b) vision

1.1.9. Vitreous humor

The vitreous humor is a gel-like material constituting about 80% of the ocular globe volume. The vitreous is comprised mostly water (98%), Type II collagen, and hyaluronic acid [77]. It acts as an incompressible structure in the posterior segment and provides mechanical support for the ocular tissues surrounding it during ocular movements [77]. Although the vitreous is a permeable medium [78], the flow across the aqueous-vitreous boundary is negligible in comparison to the outflow through the trabecular meshwork [79,80].

1.2.Pathophysiology of glaucoma

Glaucoma is a major public health concern. It affects 50 million people worldwide and bilaterally blinds more than 7 million [81]. Glaucoma is the second leading cause of blindness after cataract [1,82]. Further, it mainly affects the elderly [83,84], and its prevalence is expected to increase as the population ages. In the following sections, first some general information about glaucoma is presented. Then,

the characteristics of angle-closure glaucoma, a type of glaucoma closely related to the iris contour and the anterior chamber angle, is discussed. Finally, various cases of corneoscleral indentation used to change the anterior chamber angle (mainly in relation to angle-closure) are discussed.

1.2.1. Characteristics and classifications of glaucoma

Glaucoma describes a wide variety of the potentially blinding ocular diseases. The central event in all types of glaucoma is the irreversible damage to the retinal ganglion cells of the optic nerve head, which leads to programmed cell death (apoptosis). Loss of retinal cells leads to progressive loss of vision (Figure 1.8). Increased IOP, although no longer considered a defining criterion for glaucoma [81], is widely accepted as a major glaucoma risk factor [85-88]. A normal eye has an IOP of 15 mmHg [54]. Any value of IOP greater than 21 mmHg increases the risk of glaucoma development [87]. It has also been shown that IOP reduction is beneficial in the management of glaucoma patients [86,87,89,90], while a small fraction of patients continue to progress even with treatment [86,89]. The mechanism by which increased IOP leads to irreversible damage of the retinal ganglion cells of at the optic nerve head is still unknown. There have been, however, theories proposed to explain the mechanisms of IOP-induced optic nerve head neuropathy (e.g. [26]).

The iris configuration, closely related to the mechanism by which IOP increases, has been used to classify different types of glaucoma. Two major categories of

glaucoma are open-angle and angle-closure glaucoma with angle being referred to the anterior chamber angle (Figure1.2).

Primary open angle glaucoma is the most common form of glaucoma [81]. In pigmentary glaucoma, a mysterious type of open angle glaucoma, the iris is abnormally bowed towards the posterior. The posterior bowing of the iris is caused by "reverse pupillary block" [91], a transient elevation of the pressure in the anterior chamber. It is widely accepted [91-93] that in pigmentary glaucoma, pieces of the iris pigment separate from the iris surface and enter the aqueous humor flow when the iris posterior pigment epithelium is mechanically rubbed against the zonular fibers. Being carried by the aqueous humor flow, the pigment granules are further deposited in the trabecular meshwork. It could be postulated that continuous deposition of the pigment particles decreases the permeability of the trabecular meshwork and consequently decreases the outflow. Decreased outflow, not accompanied with decreased inflow, would increase IOP. It has been experimentally proven [94] , however, that the increase in IOP is not caused by an excessive amount of particle deposition in the trabecular meshwork. The reason causing pigmentary glaucoma has remained unknown.

In angle-closure glaucoma, the aqueous humor outflow pathway is directly blocked by anterior bowing of the iris periphery. The pathophysiology of angle-closure glaucoma is discussed in more detail in the next section (section 1.2.2). It should be also noted that IOP may reach higher values due to reasons unrelated to the iris contour. An

example could be expansion of the post-surgical intravitreal gas bubbles following an altitude increase (discussed in Chapter 3).

1.2.2. Angle-closure glaucoma

As shown in Figure 1.9, in primary angle-closure glaucoma, the periphery of iris mechanically blocks the outflow pathway of aqueous humor. Angle closure drives its name from the closed or narrowed anterior chamber angle caused by anterior bowing of the iris. Pupillary block is considered an underlying mechanism of the iris anterior bowing and angle-closure. Due to a narrow gap between the iris tip and the lens, the aqueous humor pressure in posterior chamber is slightly higher than the pressure in the anterior chamber. In reverse pupillary block, the higher pressure in the posterior chamber generates a net force that pushes the iris periphery towards the anterior, leading to a significant narrowing or complete closure of the anterior chamber angle and consequently blockage of the outflow pathway [95-97]. Certain physiological phenomena such as pupil constriction [98,99], pupil dilation (discussed in Chapter 6), and accommodation [100,101] can affect the iris profile and possibly change the anterior chamber angle.

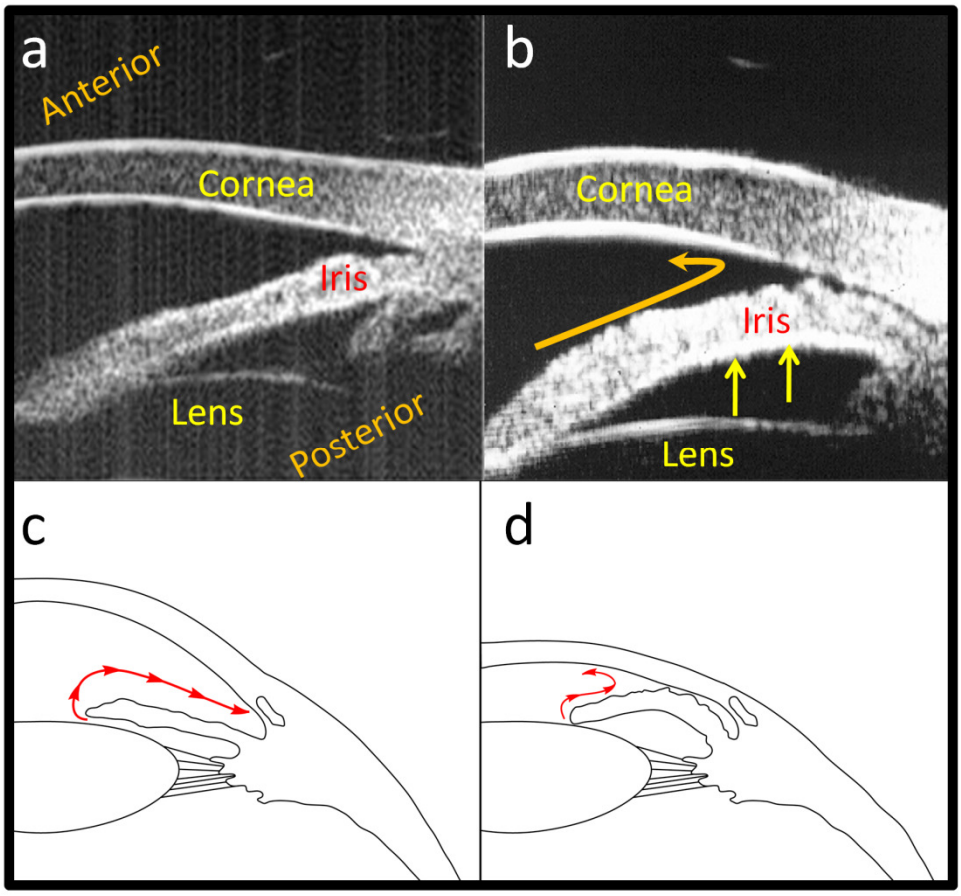

Figure 1.9 Ultrasound biomicroscopy (UBM) and schematic of the anterior chamber of a normal (a and c) eye in comparison with primary angle-closure glaucoma(b and d) (UBM images are from Dr. Ritch, New York Eye & Ear Infirmary and schematics are modified from National Eye Institute, NIH, Bethesda, MD)

Peripheral laser iridotomy is a common surgical method to treat pupillary block and angle-closure [102-104]. In this method, a surgical hole is made on the periphery of the iris to equalize the pressure between the anterior and posterior chambers. When the pressure is equalized in the two chambers, the net force pushing the iris forward decreases, the iris moves towards the posterior, the anterior chamber angle opens, and the outflow pathway blockage is removed. Peripheral laser iridotomy is also a useful treatment option for reverse pupillary block associated with pigmentary glaucoma

(section 2.1.1) [105]. The same mechanism of equalizing the pressure between the anterior and posterior chambers moves the iris forward and removes the reverse pupillary block.

1.2.3. Corneoscleral indentation

Iris contour and anterior chamber angle can also be altered by ocular globe deformation caused by corneoscleral indentation. During corneoscleral indentation an object, pushed against the surface of the cornea and/or sclera, deforms the ocular globe. Although the purpose and application of each procedure may be different from other ones, in all of them applying pressure against the corneal and/or scleral surfaces leads to anterior chamber angle alteration. These methods are discussed in detail in Chapter 2.

1.3.Theoretical modeling of the eye

Theoretical models have provided a better understanding of the physiology and pathophysiology of the eye. For example, mathematical models of aqueous-humor-iris interaction [99,106,107] have brought about new insights not only into the glaucoma risk factors and mechanisms, but also about the normal ocular physiological phenomena such as pupil constriction and accommodation. Mathematical models could be used as tools to improve the diagnosis and treatment methods. Here are some of the key advantages of using mathematical models:

- Theoretical simulation, in comparison to human and animal studies, has lower costs and minimized risks. It also helps to design future human and animal experiments.

- Mathematical models can provide detailed predictions of quantities that cannot otherwise be acquired experimentally. For example, the pressure difference between the posterior and anterior chambers cannot be measured using clinical methods. The models create a more locally comprehensive map of pressure or other biomechanical data.

- In the field of tissue biomechanics, mathematical models have gained tremendous popularity in interpretation of experimental data on tissue response to loading (e.g. [108,109]). These models have enabled the researcher to capture the structural anisotropy of the tissue from the large-scale mechanical tests and quantify the complex behavior of the ocular tissue.

- An important feature of theoretical models is the ease of performing parametric studies [110]. When a computational model is developed, changing simulation parameters are often not that costly. Parametric studies are strong tools in performing sensitivity analysis or predicting risk factors associated with ocular disorders (e.g. [111]). In addition, computer simulations can provide an opportunity to study changes in

every single parameter while the other parameters remaining unchanged.

- The ability of the finite element method to handle complex geometries along with the advent of advanced ocular imaging modalities such as optical coherence tomography (OCT) and ultrasound biomicroscopy (UBM) have made it possible to develop subject-specific models. Such models could provide valuable information to reduce future clinical examinations and/or asses the successfulness of certain treatments based on anatomical and physiological characteristics of single patients.

Numerous models of the ocular globe have been developed to understand how mechanical deformation of the globe changes the optical functions of the eye. Asejczyk-Widlicka *et al.* [29] created a model of corneoscleral shell to study the contribution of the ocular tissue mechanical properties of to the quality of the image produced by the eye. By using a simple model consisting of the cornea, sclera, and limbus, they showed that the ocular focal point moves axially following changes in the IOP. An important conclusion of their study was the important role of limbus anisotropy in the mechanical behavior of the ocular globe. The mechanical contribution of the lens [112], zonular fibers [112], and outer layer of the globe [113] were further added to the model for the same purpose of studying mechanically-induced changes in the optical function of the eye.

Table 1.2 Comparison of the theoretical models of the anterior segment

Investigator	Methods		Fluid-structure interaction	Other information
	Aqueous Humor	Iris		
Mapstone 1968 [98]	Excluded	Active	Excluded	2-D vector analysis used to describe Pupil-blocking force.
Friedland 1978 [114]	Steady state Stokes flow	Rigid boundary	Excluded	Analytical solution for the flow profiled was obtained. The flow through the pupil was excluded.
Tiedeman 1991 [115]	Excluded	Thin structure, Passive	Excluded	Iris deformation was simulated.
Silver and Quigley 2004 [116]	Steady-state Navier-Stokes flow	Rigid boundary	Excluded	Only the flow passing through the iris-lens gap was modeled.
Kumar *et al.* 2006 [117]	Steady-state Navier-Stokes flow	Rigid boundary	Excluded	Aqueous humor flow in the anterior segment and through the trabecular meshwork is modeled
Fitt and Gonzalez 2006 [118]	Steady- state lubrication flow	Rigid boundary	Excluded	Flow generated by sources other than the secretion from the ciliary bodies is also studied.
Kapnisis *et al.* 2009[119]	Transient Navier-Stokes flow	Rigid boundary	Excluded	Aqueous humor collection from the human eye during needle aspiration.
Heys *et al.* 2001 [120]	Transient Navier-Stokes flow	Linear elastic, Passive	Included	Mechanics of the healthy eye, iris constriction†, blinking‡, and iris bombé were studied.
Heys and Barocas 2002 [121]	Transient Navier-Stokes flow	Linear elastic, Passive	Included	Accommodation in healthy eye and pigmentary glaucoma was studied. The lens was considered as a moving rigid boundary.
Huang and Barocas 2004 [99]	Steady-state Navier-Stokes flow	Nonlinear elastic, Active	Included	Pupil constriction in the healthy eye and PCGA eye along with the PCGA anatomical risk factors were studied.
Huang and Barocas 2006 [107]	Transient Navier-Stokes flow	Nonlinear elastic, Passive	Included	The accommodative micro fluctuations were studied. The lens was considered as a moving rigid boundary.

† The iris constriction was simulated in a passive model.

‡ The whole-globe deformation was excluded in the simulation.

Due to its importance in pathophysiology of glaucoma, biomechanics of the anterior eye have been studied thoroughly via theoretical models. A summary of these models is presented in Table 1.2. The first fluid dynamics model dealing with aqueous humor flow was developed by Friedland [114]. Ignoring the solid deformation of the iris, Friedland solved for the aqueous humor flow profile by assuming all tissues to be rigid. In Friedland's model, the geometry was simplified in order to obtain an analytical solution for the Stokes equation. In addition, flow through the pupil was ignored, and the analytical solution was obtained only for the anterior and posterior chambers. On the other hand, Tiedeman [115] studied the solid mechanics of the iris without solving for the aqueous humor flow. In Tiedeman's model, the edges of iris were fixed, uniform pressure was applied on the posterior surface of the iris, and finally tension was applied on the tip of the iris. Since Tiedeman did not account for the fluid dynamics, no shear force resulting from the aqueous humor flow was applied on the iris boundary. Tiedeman also assumed that the iris was an infinitely thin structure.

Several computational studies have been conducted solely on the flow of aqueous humor. Silver and Quigley [116] solved the Navier-Stokes flow passing through the iris-lens channel. They found that the channel length and aqueous humor flow rate have a significant effect on the magnitude of posterior to anterior pressure difference. Kumar *et al*. [117] studied the steady-state flow of the aqueous humor in the anterior chamber. They obtained the solution to the Navier-Stokes equation with the help of a commercial finite element package. Kumar *et al*. neglected the iris deformation and modeled the iris as a rigid boundary. Recently, Kapnisis *et al.* [119] simulated the flow

of aqueous humor through an aspiration using commercial finite element software. The model treats the iris as a rigid boundary but it accounts for the transient nature of the flow during the aspiration process.

More detailed models were developed by Heys *et al.* [101,106,120-122] to simulate the mechanical interaction of the aqueous humor flow and the iris. Considering the outcomes of experimental tests on the bovine iris [33], Heys *et al.* used a linear elastic formulation in order to simulate the iris deformation. The aqueous humor was modeled as a Newtonian fluid. While the calculated Reynolds number of the flow was rather small in their study, Heys *et al*. preferred to use the full Navier-Stokes equations to deal with the transient phenomena. Not only did they model the fluid-structure interaction of the aqueous humor and iris, but they also considered quite detailed boundary conditions such as a deformable corneal surface and a rigid but moving lens surface in their studies. With the help of their model, Heys *et al*. brought new insights to mechanics of healthy eyes as well as phenomena such as accommodation, iris constriction and blinking. They also studied eye disorders such as pigmentary glaucoma and iris bombé, an extreme anterior bulging of the iris.

To enhance the study of Heys *et al*., Huang and Barocas [121] altered the linear elastic iris to a neo-Hookean solid. In addition, they introduced active iris stress in order to model pupil constriction. The study of Huang and Barocas confirmed the hypotheses of the iris force vector analysis formerly proposed by Mapstone [98]. Huang and Barocas [121] also examined the anatomical risk factors associated with pupillary block.

The study of Huang and Barocas, however, was performed in a steady state manner and did not account for the transient nature of the anterior segment mechanics during the pupil constriction; it was also based on idealized geometry, and the detailed structure of the iris was not included in the simulation. Huang and Barocas [107] also studied the computational model of accommodative microfluctuations.

The mechanical models have brought considerable insights into several aspects of physical and physiological phenomena in the eye. Nevertheless, none of them have fully captured the complex problems of transient aqueous humor flow, fluid-structure interaction of the aqueous humor and the iris, and the complex iris structure. Moreover, to our knowledge, the effect of whole ocular globe deformation on the mechanics of the anterior segment was not investigated previously.

1.4.Open questions

Computational models of ocular mechanics have been extensively studied by numerous investigators. Although several important issues have been addressed, there exist various questions that have remained unanswered:

- Clinical studies have proven that, regardless of the methods used, corneoscleral indentation changes the anterior chamber angle. *Is there a unifying explanation for how ocular globe deformation leads to changes in the anterior chamber angle? What is the effect of anterior chamber*

angle opening due to corneoscleral indentation on the iris-aqueous-humor interaction?

- Clinical studies have shown that IOP rises when a patient with an intraocular gas bubble travels to higher altitudes. Further, changes in IOP alter aqueous humor inflow and outflow rates. *What medical options might mitigate this effect?*

- Experimental observations have shown that prevention of blinking would shift the iris to the anterior. *What is the mechanism by which blinking alters the iris profile and IOP?*

- The iris muscle has a complex geometry with three main components (the dilator, sphincter, and stroma). *How can relative position of these components affect the iris function?*

The remainder of this document consists of six more chapters. The answers to the questions posed above are provided in the next five chapters. The final chapter discusses the conclusion of the thesis and proposes future plans to modify the method and implement additional computational and experimental explorations.

Chapter 2: Mathematical Model of Ocular Globe Deformation during Corneoscleral Indentation

(This work was part of the paper "Anterior chamber angle opening during corneoscleral indentation: the mechanism of whole eye globe deformation and the importance of the limbus" by R. Amini and V.H. Barocas, Invest Ophthalmol Vis Sci 2009; 50:5288-5294 [123] (Association for Research in Vision and Ophthalmology as the copyright holder is acknowledged))

2.1.Summary

The purpose of this study was to determine how mechanical interaction among iris, cornea, limbus, sclera, and IOP contribute to angle opening during indentation of the cornea or sclera. A finite-element model of the globe was developed. The model consisted of three elastic isotropic segments – iris, cornea, and sclera – and a two-component anisotropic segment representing the limbus. The model was tested against data from published *in vitro* experiments and then applied to angle opening during indentation *in vivo*. Indentation of the central cornea with a cotton bud, indentation with a small or large eye cup during ultrasound biomicroscopy, indentation with a gonioscopy lens, and scleral indentation during goniosynechialysis were modeled.

The anisotropic limbus model matched published data better than any isotropic model. Simulation of all clinical cases gave results in agreement with published observations. The model predicted angle opening during indentation by a cotton bud or small eye cup, but angle narrowing when the sclera was indented by a large eye cup. The model of indentation gonioscopy showed narrowing of the angle on the indentation side and opening of the angle on the opposite side. Non-uniform opening of the angle was predicted when the scleral surface was indented. The two-component model of the

stiff fibers embedded in a soft matrix captured the mechanical properties of the complex limbal region effectively. The success of this model suggests that, at least in part, corneoscleral mechanics drive angle opening rather than aqueous humor pressurization.

2.2.Introduction

There are numerous instances in which intentional or unintentional pressure upon the corneoscleral junction results in the opening or narrowing of the anterior chamber angle. These include

- Indentation gonioscopy of angle-closure glaucoma [57,124-126].
- Inadvertent opening of the angle during UBM [127,128].
- Manual indentation of the central cornea to open the angle and alleviate acute angle-closure [126,129-131].
- Scleral indentation to improve angle visualization during goniosynechialysis [132].
- Anterior Drift of the Iris when Blinking is Prevented [100,133].

These cases are discussed in detail in the following sections

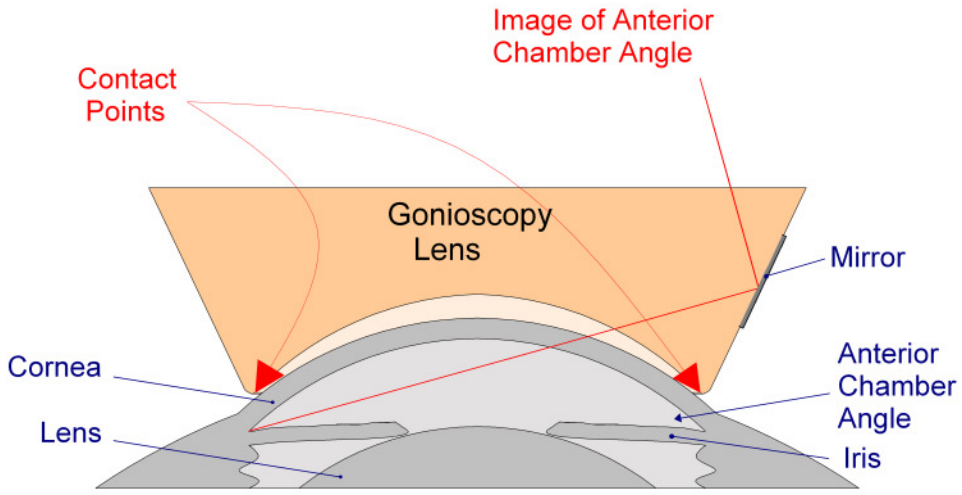

Figure 2.1 Gonioscopy lens used to visualize the anterior chamber angle

2.2.1. Indentation gonioscopy

Gonioscopy lenses are used to visualize the anterior chamber angle [125]. In normal eyes, the trabecular meshwork can be seen via gonioscopy (Figure 2.1). In a patient with angle-closure, all or parts of trabecular meshwork is covered by the iris and consequently not visible during gonioscopy. The examiner, by applying focal pressure to the lens opposite the region of interest (e.g., pressure in the superior region when viewing the inferior region), can induce opening of the angle and uncover the trabecular meshwork [124-126].

Indentation gonioscopy is a useful method to differentiate between appositional angle-closure and peripheral synechial angle-closure [126]. In peripheral synechial closure the iris periphery is attached to the trabecular mesh work. Similar to appositional angle-closure, in peripheral synechial closure, trabecular meshwork cannot

be seen during gonioscopy. Unlike appositional angle-closure, however, indentation gonioscopy does not open the anterior chamber angle in patients with peripheral synechial angle-closure. Unless otherwise mentioned, in this document we use angle-closure to mean appositional angle-closure.

2.2.2. Indentation during ultrasound biomicroscopy (UBM)

Because of its *in vivo* anatomical and functional imaging capability, UBM has been used by clinicians in diagnosis of angle-closure [95]. In particular, UBM images can produce a cross-sectional view of the anterior chamber with a detailed image of the iris contour and anterior chamber angle. It has been reported that pressure applied to the eye cup during UBM can produce artifactual opening of the anterior chamber angle if a small cup is used (Figure 2.2), but not if a large cup is used [127]. This effect has been subsequently exploited deliberately [128] to design a new eye cup for indentation UBM gonioscopy to open the anterior chamber angle.

2.2.3. Manual indentation of the central or peripheral cornea

Increased IOP from acute attacks of angle-closure can be alleviated by corneal indentation. Clinicians use several different instruments such as squint hook, cotton bud, glass rod, and gonioprism to indent the central or peripheral surface of the cornea [126,129-131]. Following the corneal indentation, the anterior chamber angle opens and the aqueous humor outflow pathway is unblocked leading to a drop in IOP.

Masselos *et al.* [129] recently reported that central corneal indentation led to a significant reduction in IOP in six of seven acute angle-closure cases studied.

2.2.4. Scleral indentation

Goniosynechialysis is a surgical method used to treat synechial angle-closure [134]. In this method, the angle closed by peripheral anterior synechiae (discussed in section 1.2.3.1) is mechanically opened. Scleral indentation has been developed as a technique to directly visualize the anterior chamber angle during goniosynechialysis [132]. Using UBM, Takanashi *et al.* [132] have shown that indenting the sclera with a cotton bud, 2 mm from the limbus, would induce a significance opening of the anterior chamber angle.

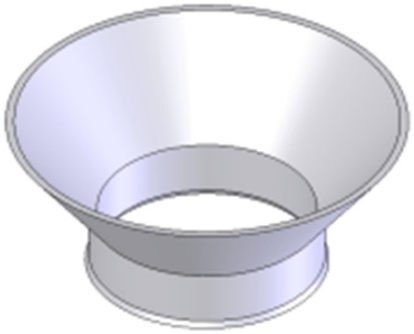

Figure 2.2 Schematic of an eye cup used to indent scleral or corneal surfaces during UBM

2.2.5. Blinking

Spontaneous blinking is one of the three major types of blinking (spontaneous, reflex, and voluntarily blinking). The mechanism of the spontaneous blinking is still debatable. It is, however, known that the lower eyelid is stationary during each blink and the closure is done by the higher eyelid [135]. Although no external object indents the corneoscleral surface, blinking-related changes in the iris contour [100,133] and in IOP [136,137], observed experimentally, suggest that mechanism of blinking is similar to that of other types of corneoscleral indentation. In particular, in eyes with pigmentary glaucoma [100,133], narrow angles [100], and healthy controls [100], it was found that when blinking was prevented by the presence of an eye cup for UBM examination, the iris bowed progressively more to the anterior (or, in the pigmentary glaucoma case, progressively less to the posterior). The phenomenon suggests that blinking, possibly by pressing the higher eyelid against the corneoscleral shell, provides a mechanism to push the iris to the posterior.

2.2.6. Corneoscleral indentation and ocular globe deformation

The various instances of corneoscleral indentation, taken collectively, point to a complex mechanical system in which pressures applied in one location cause effects in others, and in which the interaction among the cornea and sclera must be considered in order to understand the underlying mechanism for angle-opening during indentation.

The purpose of this project was to determine how a variety of indentation techniques alter the angle differently; this goal was accomplished by means of a unifying finite-element model of the corneoscleral shell during indentation. Although previous models have been developed with emphasis on the effect of IOP on lamina cribrosa [26,111,138-141] or on corneal mechanics [12,108,109], the latter with a high degree of structural accuracy, to our knowledge no such model has been applied to indentation.

In developing the model, particular attention had to be paid to the limbus, in which collagen fibers are highly aligned around the circumference of the cornea [27,142]. The obvious consequence of this alignment is that the limbus provides purse-string-like support and prevents expansion of the cornea when the IOP is increased [29,30,108,143]. For the purpose of our studies, however, it must also be recognized that the high alignment of the fibers in the circumferential direction renders the limbus *more* compliant in the meridional direction [10]. That is, the structural anisotropy of the limbus produces mechanical anisotropy, which plays a role in the response of the angle.

2.3.Methodology

2.3.1. Study design

A finite-element model of the corneoscleral shell was created as described in the next section. Three different sets of simulations were performed:

Model validation studies using simulated inflation of the isolated (human) cornea and the isolated (porcine) globe. These studies were designed to test whether our model could match experimental observations regarding corneoscleral mechanics. Specifically, it has been reported that when the isolated cornea is inflated, the central cornea stretches considerably less than the limbus [28], and that when the whole (porcine) globe is inflated, the sclera changes curvature significantly but the cornea does not [30]. We simulated those two experiments to assess the validity of our model before continuing to our studies of indentation.

Parametric studies on the support of the posterior eye. The interaction between the eye and the surrounding tissue is quite complex [144], but because of our focus on the anterior segment, we simplified the posterior-segment model as a fixed boundary on part of the sclera. A series of simulations were performed to assess the effect of the size of the fixed boundary on the results. Since we found no significant effect on the results, we subsequently chose an intermediate value for the application studies described in the next paragraph.

Application studies on the different modes of indentation. We simulated the various indentation scenarios described in section 2.2, calculating the amount of predicted angle opening in each case. It is noted here that the actual amount of angle opening would depend on interactions among the iris, aqueous humor, and lens. Aqueous-humor-iris interaction and lens-iris interaction were not considered in the current model and will be discussed in Chapter 4. Rather, we calculated the amount of

angle opening that would arise at the iris root absent interaction with aqueous humor and lens, using that quantity as a measure of how strongly the indentation compels the angle to open.

2.3.2. Finite-element simulation

A finite-element model of the corneoscleral shell was created using the software ABAQUS (SIMULIA, Providence, RI) and mechanical and geometric data from the literature (summarized in Table 2.1 and Table 2.2). The model consisted of four sections: iris, cornea, sclera, and limbus (Figure 2.3). The Iris, cornea, and sclera were treated as homogeneous, elastic, nearly-incompressible solids.

Because of the special architecture and properties of the limbus, a two-component model was introduced (Figure 2.3b), in which multiple high-stiffness (Young's modulus $E \approx 15 * E_{cornea}$) rings were embedded in a more compliant ($E \approx 1/20 * E_{cornea}$) surrounding matrix. The consequence of this geometry was that the limbus was stiff in circumferential loading because of the rings, but compliant in meridional loading because of the matrix. Thus, the two-component limbus constituted a highly idealized simplification of the complex anatomy that captured the key feature for this study, the large degree of anisotropy in the limbus. The number and cross-sectional area of fiber and the compliance of the matrix and fiber network were designed using the theory of composite materials [145] to produce a model that matched the measured elasticity of the limbus [10].

The boundary conditions on the inflation models were as follows. The interior surface of the corneoscleral shell was set to an elevated pressure (the IOP, which was published in the experimental studies [28,30]), and the exterior surface was set to zero pressure. For corneal inflation, only the extreme anterior of the sclera was simulated, and the edge of it was fixed to simulate mounting in the testing apparatus. The pressure was increased progressively, and the finite-element solution was compared to the experimental data. For the corneal inflation case [28], displacement was reported and easily compared between model and experiment. For the whole-globe inflation case [30], the relationship among IOP, volume change, and curvature change was reported. IOP was the input parameter to our model, so we needed to calculate final volume and corneal and scleral radius of curvature. Volume change was determined by subdividing the interior space of the model into triangles (in axisymmetric cases) or tetrahedrals (in non-symmetric cases) and using standard geometric formulae to calculate the volume. Radii of curvature were calculated by fitting a circle to the final position of the exterior surface. In addition to the fiber-matrix model, in both cases the limbus was modeled as an isotropic section with different elastic modulus, and the results were compared with the experimental studies.

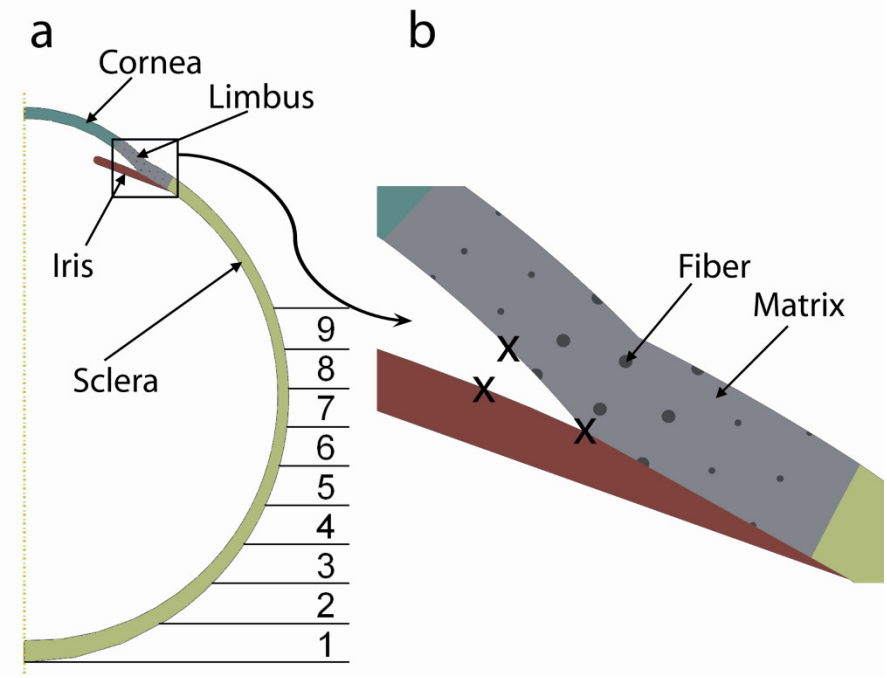

Figure 2.3 Model of Globe Deformation. (a) Axisymmetric model of the whole globe and nine different regions used as the supports on the sclera. Regions are cumulative, so region 7, for example, includes the entire posterior half of the globe. (b) Detailed fiber-matrix structure of the limbal section, showing the high-stiffness rings embedded in a low-stiffness matrix. The three-dimensional model geometry was specified by revolving the axisymmetric profile around the corneal axis. The angle was calculated using the three points marked with x's.

For the indentation simulations, zero displacement was imposed over a region at the posterior of the sclera to represent the support from the surrounding tissue. As can be seen in Figure 2.3a, the size of the region was varied from very small (region 1) to just over half of the globe (region 9). The results were insensitive to the choice of region (less than 3% variation when different regions were fixed), so it was concluded that the approximation was acceptable; subsequent simulations were performed using region 1-

4. Exterior surfaces of the cornea and sclera that were not in the fixed region or directly under the indenter were set to zero pressure.

In simulating indentation of the intact globe, we required that the volume of the globe remain unchanged. This stipulation was based on the incompressibility the material inside the eye and the relatively small amount of outflow. For a patient with a normal outflow facility of 0.2 μl/(mmHg•min) and a "lid squeeze" IOP of 120 mmHg [146,147], the outflow rate would be only 0.4 μl/sec; since indentation is typically on the order of a few seconds, only a few microliters of volume would be expected to be lost.

In order to do the simulations, we needed to specify one of the IOP, the total force of indentation, or the total distance of indentation. Lacking good data on any of the three, we chose to specify an IOP of 120 mmHg, a level measured during a hard lid squeeze [146,147]. That is, we assumed that all modes of indentation produced roughly the same IOP as a hard lid squeeze. Although this was a considerable simplification, it provided a consistent basis for the different models. Once the IOP was set, an initial indentation force was guessed, and the simulations were performed. The results were analyzed to determine the total volume, and the indentation force was modified, keeping the same indentation area, until the results gave a volume change of less than 2.5 μl. Once the appropriate indentation force had been determined, the results were further analyzed to calculate iris root rotation. Specifically, angle opening was calculated by taking the angle formed by the trabecular meshwork and two points, one

on the anterior iris surface and one on the posterior cornea surface, 500 μm from the trabecular meshwork (Figure 2.3b).

The axisymmetric model was used in the central corneal, large UBM eye cup, and small UBM eye cup indentation simulations. To simulate central corneal indentation with a cotton bud, pressure was applied on a circle, 2.5 mm in diameter centered on the corneal apex. The diameters of eye cups simulated were 13 and 18 mm [127]. To simulate the eye cup indentation, we applied pressure on a section, 0.35 mm wide, on the corneal or scleral surfaces 6.5 mm and 9 mm from the corneal axis. To simulate indentation gonioscopy with a Sussman lens (D_{lens} = 9 mm), we applied pressure on a section, 0.35 mm wide and 4.7 mm long located 4.5 mm from the corneal axis. To model the asymmetric scleral indentation, pressure was applied 2 mm from the limbus on a section 0.35 mm wide and 5.5 long.

Table 2.1 Mechanical properties of the ocular tissue used in the model

Parameter	**Value**	**Reference**
Modulus of elasticity (MPa)		
Cornea	19.1	[9,10]
Sclera	6	[22,25]
Limbus		
Fiber	300	†
Matrix	1	†
Iris	0.027	[33]
Poisson's ratio		
Cornea	0.5	[148]
Sclera	0.49	[24]
Limbus		
Fiber	0.5	†
Matrix	0.5	†
Iris	0.5	[33]

† The mechanical properties of the fiber and matrix sections in the limbus model were chosen to match the circumferential and meridional stiffness measured by Hjortdal [10].

Table 2.2 Geometric parameters of the ocular tissue used in the model

Parameter	**Value**	**Reference**
Thickness (mm)		
Cornea (average value)	0.55	[3]
Human Sclera		
Near the optic nerve head	1	[20,21]
Near the equator	0.5	[20]
Near the limbus	0.65	[20]
Porcine Sclera		
Near the optic nerve head	0.8	[149]
Near the equator	0.8	[149]
Near the limbus	1.12	[149]
5 mm from the limbus	0.4	[149]
Limbus	0.65	[149,150]
Iris	0.34	[151]
Radius of curvature (mm)		
Cornea (average value)	7.8	[3]
Human Sclera	12.5	[17-19]
Porcine Sclera	8.1†	[149]
Limbal length	2.8	[150]
Anterior chamber diameter (mm)	10.4	[152]
Anterior Chamber Angle (°)	25	[103,151,153,154]

† The scleral profile was obtained from the histology images presented by Olsen *et al*.[149]

2.4.Results

2.4.1. Validation studies

Figures 2.4 and 2.5 show the results of model validation. Simulation of corneal inflation showed that when the posterior corneal surface is pressurized, the displacement of a point midway from the corneal apex to the limbus was 92% of the corneal apex displacement (Figure 2.4a). Since very low pressures are not physiological [28], we measured our displacements with 3KPa (22 mmHg) as the reference point. The results, shown in Figure 2.4a, compare favorably with Figure 9 of Boyce *et al.*[28] . When the limbus was modeled as isotropic, the ratio of the midperiphery to apex displacement changed dramatically (Figure 2.4b). When the limbus was made stiff (E= E_{cornea}, E= E_{sclera}, or E= E_{fibers}), the predicted displacement in the midperiphery dropped considerably. In the stiffest case (E= E_{fibers}), the displacement of the midperipheral point was less than 40% of the apex displacement. In contrast, when the limbus was modeled as a compliant isotropic material (E= E_{matrix}), the midperipheral point moved as much as 95% of the apex.

Figure 2.5a shows the changes in the radius of curvature of the cornea and the sclera when the whole globe is pressurized. Consistent with published experimental data (Figure 3 of Ref. [30]), the corneal radius of curvature did not change dramatically, but the scleral radius of curvature changed by about 2 mm when the pressure increased from 15 to 60 mmHg. Figure 2.5b shows the ratio of change in the corneal radius of

curvature to change in the scleral radius of curvature when the pressures changed from 15 to 45 mmHg. The ratio is very small for the experimental case (0.02), a result of the annular support from the limbus and the geometry of the porcine globe. The stiff-limbus model ($E = E_{fibers}$) and the anisotropic-limbus model gave relatively small ratios (the stiff model actually predicted that the corneal curvature would *decrease*), whereas the other models ($E= E_{cornea}$, $E= E_{sclera}$, or $E= E_{matrix}$) did not give reasonable predictions for the curvature change ratio.

In examining the Figures 2.4b and 2.5b together, we see that only an anisotropic mechanical model of the limbus can capture both the meridional compliance (Figure 2.4b) and the circumferential stiffness and resulting maintenance of corneal curvature (Figure 2.5b). Thus, the anisotropic model was used for all simulations.

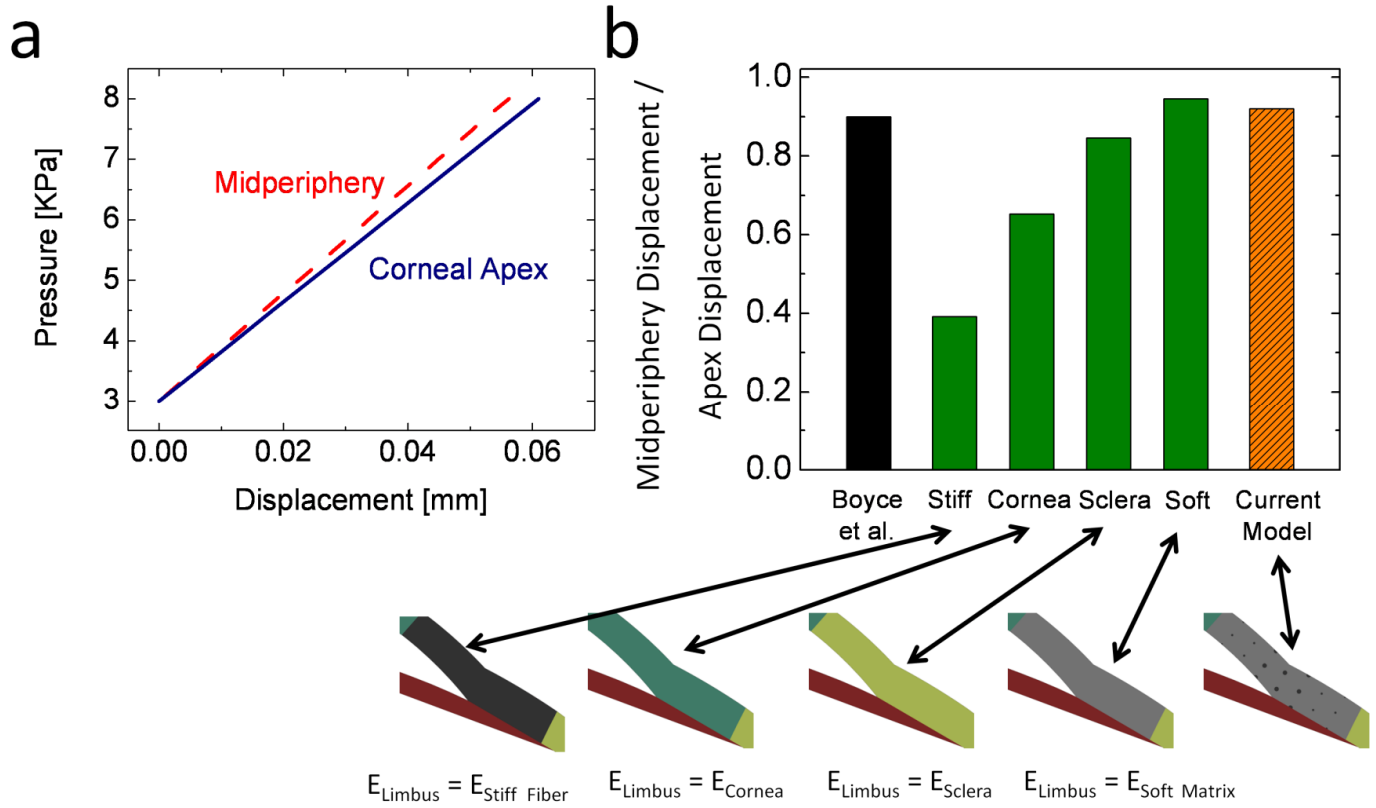

Figure 2.4 Comparison of Model with Published Experimental Studies. (a) Simulated pressure-displacement profile for the corneal apex and a point midway from the limbus to the apex. (b) Ratio of the displacement of midperipheral point to the displacement of the corneal apex compared for different models of limbal section and published experimental data [28]. The limbus was modeled as isotropic (green bars) with a modulus of either 300 MPa (STIFF), 19.1 MPa (CORNEA), 6 MPa (SCLERA), or 1 MPa (SOFT), and also as a fiber composite (striped bar) of STIFF fibers embedded in a SOFT matrix.

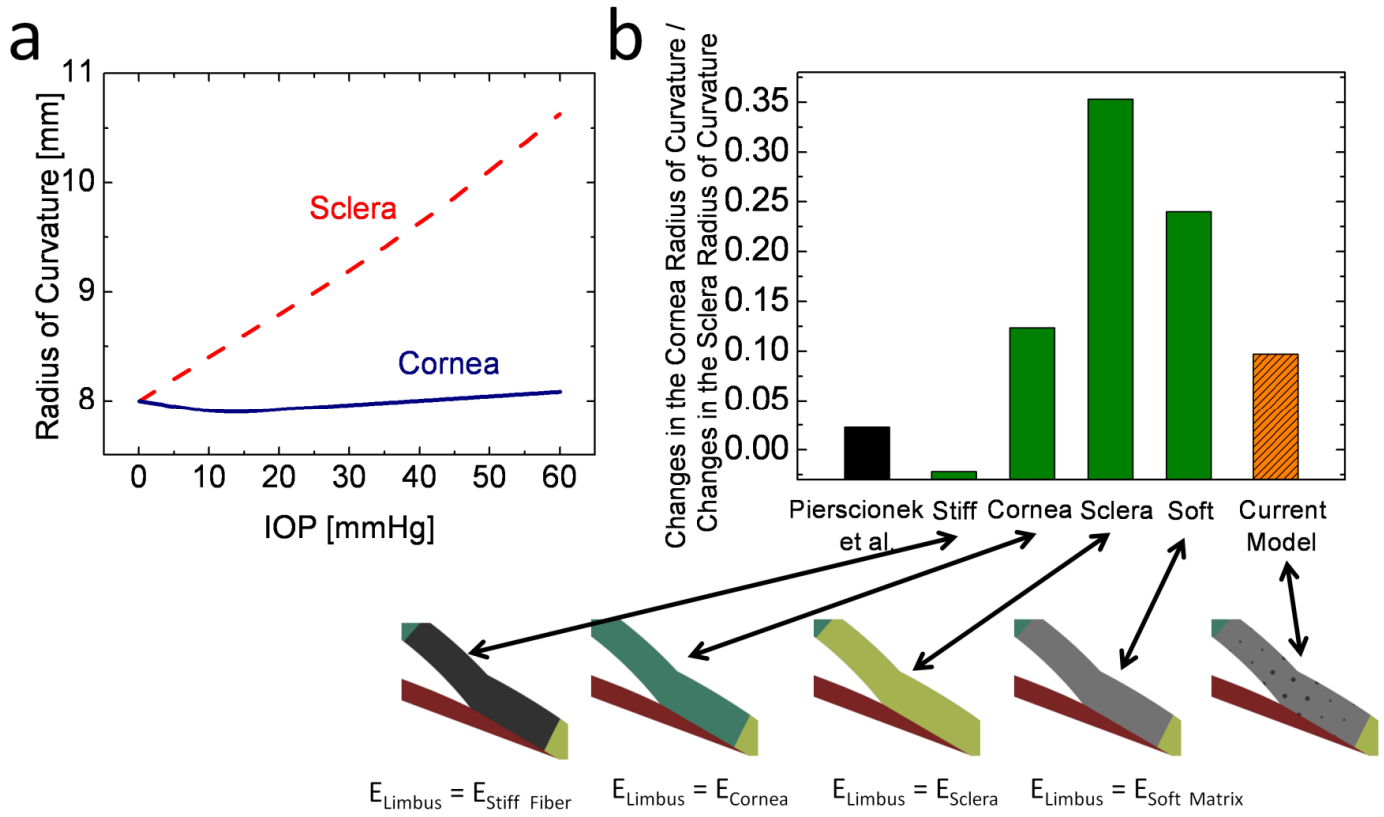

Figure 2.5 Comparison of Model with Published Experimental Studies. (a) Changes in the radius of curvature of cornea and sclera vs. pressure obtained from simulation of a porcine model. (b) Ratio of changes in cornea radius of curvature to changes in sclera radius of curvature when pressure changed from 15 to 45 mmHg for the different models of limbal section and published experimental data [30].

2.4.1. Simulation of indentation

Figure 2.6 shows the simulated eye globe before (Figure 2.6a) and after (Figure 2.6b-2.4f) each type of indentation studied. When indentation on the central cornea was simulated (Figure 2.6b), the eye remained symmetric about the corneal axis, and the angle opened 8.2° as the cornea flattened and the sclera bulged out slightly. The entire iris moved posteriorly, but we note that the motion would be less pronounced *in vivo* because of the restriction of the iris by the lens and zonules. This result is consistent with the well-established opening of the angle by central corneal indentation [126,129-131].

In the case of indentation with small eye cup (Figure 2.6c), the eye again remained symmetric, and the angle opened by as much as 24.5° as large rotations occurred at the iris root. This result is consistent with the experimental observation that indentation with a small eye cup opens the angle significantly [127]. When the large eye cup was simulated (Figure 2.6d), however, the angle narrowed by 6.7°. The cited study [127] reported no change in the angle when a large eye cup was used.

When corneal indentation with a Sussman gonioscope was simulated (Figure 2.6e), the angle narrowed by 9.7° on the indentation side and it opened by 12.5° on the opposite side. The opening of the opposite angle is observed clinically, but the narrowing at the indentation site is not observable because of the geometry of the gonioscope (Figure 2.1).

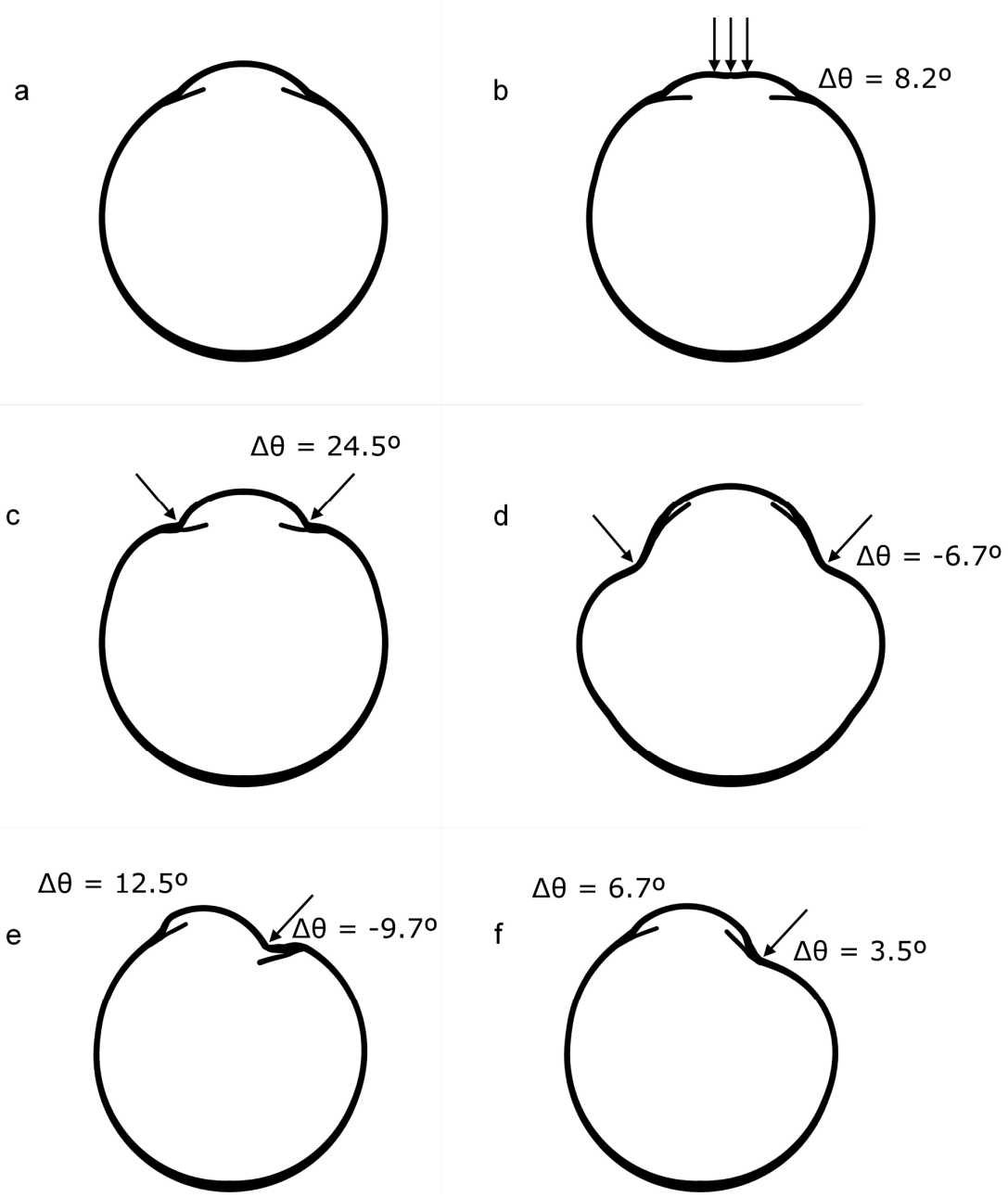

Figure 2.6 Simulation of Indentation. (a) Undeformed whole globe. (b) Axisymmetric indentation in the central cornea. (c) Axisymmetric indentation with small eye cup. (d) Axisymmetric indentation with large eye cup. (e) Asymmetric indentation with a gonioscopy lens on the corneal surface. (f) Scleral indentation during goniosynechialysis. Arrows show location of applied forces.

Finally, in the case of scleral indentation 2 mm away from the limbus (Figure 2.6f), the angle opened by a maximum of 6.7° at the point opposite the indentation site and by a minimum of 3.5° at a point nearest the indentation site.

We also calculated the total force applied to the corneal (or scleral) surface during each of the indentation cases. As can be seen in Figure 2.7, the amount of force required to produce an IOP of 120 mmHg varied greatly from just under 1 N (= 0.1 kg, or about 3.5 oz) in the case of asymmetric indentation by the gonioscope up to 7 N (= 0.7 kg, well over a pound) in the case of the large eye cup.

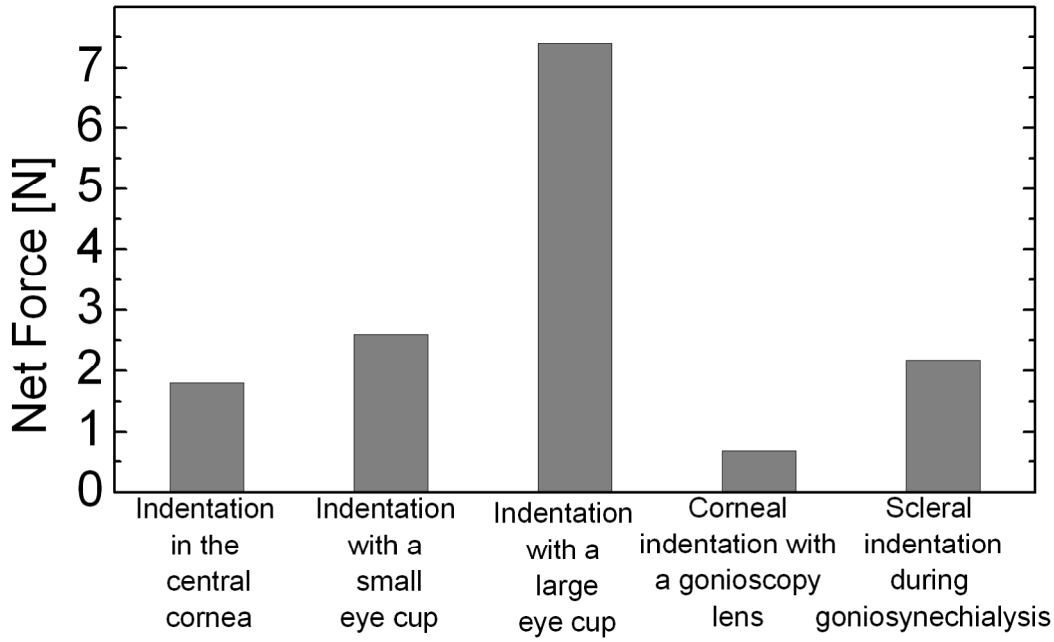

Figure 2.7 Net force was calculated for each case shown in Figure 2.6.

2.5.Discussion

The first major conclusion of this work is that the limbus, by virtue of its unique circumferential fiber alignment, is a major determiner of the deformation of the cornea and sclera. We found that a simplified model using rings to represent the collagen fibers in the limbus was able to capture its mechanical behavior, particularly the kinematics during indentation and inflation, effectively.

Turning to the simulations of indentation, the model correctly predicted angle opening under a variety of indentation scenarios. The largest amount of angle opening (24.5°) was observed during indentation with a small eye cup, followed by the asymmetric indentation of indentation gonioscopy (12.5° for the region of the angle directly opposite indentation site) and then central indentation (8.2°). Thus, if one's goal were to open the angle as much as possible with a minimum IOP increase, indentation with a small eye cup would appear to be the most effective method, but the potential advantage would have to be balanced against the inconvenience and mild patient discomfort of placing the eye cup.

The difference in force needed to generate the same IOP in different cases, which arises primarily due to differences in the contact area, is important because the examiner feels the force, not the IOP. A force of 1 N applied to one quadrant of the cornea during indentation gonioscopy would be sufficient to produce a high IOP and a significant change in the angle. The same force, however, would have only a small effect if applied to a large eye cup. Thus, it is important that the examiner be aware

that different indentation strategies can produce different IOPs and different amounts of angle opening with the same applied force. It is also possible that cushioning from saline or gel could affect the results.

While it is known that prevention of blinking leads to anterior drift of the iris, the mechanism by which this effect occurs is not known. The mechanics of blinking are extremely complex, and the force applied to the cornea or sclera by the lid is not well understood, so we did not attempt to model blinking *per se*. Rather, we observe that in all cases studied, application of pressure to the central or midperipheral cornea led to opening of the angle, so we conclude that it is highly likely that blinking causes posterior rotation of the iris by a similar mechanism. Further studies are presented in Chapter 5 to refine our understanding of aqueous-humor-iris interaction during blinking.

Some of the deformations in Figure 2.6 appear quite large and produce odd shapes in the simulated globe. These pronounced effects may be in part due to variations in indentation technique, with the note that our model assumed an IOP of 120 mmHg in all cases. The asymmetric scleral indentation (Figure 2.6f), for example, agrees reasonably well with the ultrasound image shown in Takanashi's paper [132] on the technique. On the other hand, Figure 2.6d clearly shows an artifact near the equator from our assumption about the supporting boundary condition, and the deformations of Figure 2.6e seem extremely pronounced. A more detailed and accurate account would require monitoring of force, contact area, and/or IOP during the

indentation, and the results of Figure 2.6 should be taken primarily as qualitative guides to the effect of indentation on the angle.

It is important to recognize that the model described here is consistent with all observations about indentation and angle opening *without* invoking a pressure drop between the anterior and posterior chambers. That is, the model predicts that the angle can open because of mechanical driving forces generated in the cornea and sclera, not because of aqueous humor being forced into the angle and opening it up. A mechanism involving aqueous humor and an effect similar to reverse pupillary block is certainly possible, perhaps even likely, but we conclude that the opening of the angle does not require an elevated aqueous humor pressure on the anterior surface of the iris. This prediction could be tested experimentally by repeating the Ishikawa study [127] on patients who had had successful peripheral iridotomies, eliminating any possible aqueous humor pressure difference across the iris.

Although the model described a number of experimental observations well, there are further considerations in our attempts to understand the mechanics of the globe. As mentioned in the introduction, other investigators [26,111,138-141] have attempted to explore globe mechanics to understand the mechanical environment of the optic nerve head at elevated IOP; the current model did not account for the different mechanical properties of the lamina cribrosa [26,141], for example, since we would expect different properties in the lamina to change the shape of the extreme posterior eye considerably but not to affect the angle. Perhaps more importantly, the

mechanical contribution of the lens, zonular fibers, and ciliary body was not included in the model. Since the combination of the lens, zonular fibers, and ciliary body creates an internal mechanical constraint on the deformation of the eye globe, adding them to the model could cause changes in the iris root rotation calculated by the current method. The importance of lens/zonule mechanics has been demonstrated experimentally [43] and clinically [155]. We would expect the tension in the zonules to act similarly to the limbus, resisting radial expansion but allowing anterior-posterior stretch.

Although we assumed that the volume of the globe was constant during the corneoscleral indentation, the intraocular blood volume will change when the IOP rises above the arterial perfusion pressure. When the IOP approaches 120mmHg, the ocular blood flow is significantly reduced [156] and the intraocular blood volume diminishes. Based on published data [157], we estimated the intraocular blood volume to be 2% of the total globe volume. To assess the importance of the ocular blood loss, we re-ran the central corneal indentation simulation. The same force was applied on the corneal surface but this time 2% of the globe volume was allowed to be lost. We found that the increase in the IOP was considerably lower (60 vs. 120 mmHg), but the kinematics of the iris root rotation, the primary concern of our study, changed only slightly (about 20% of the calculated value) with no qualitative change (i.e., the angle remained widened).

Another considerable simplification was the assumption that the complex interaction between the globe and the surrounding muscle, bone, and fat can be modeled as a fixed boundary around a certain region of the posterior eye. Based on the

small variations in our parametric studies and the success of the current model in describing the clinical and experimental observations, we conclude that detailed models of the surrounding tissue is necessary only if one wishes to understand specific, local interactions.

Chapter 3: Mathematical Model of Ocular Globe Deformation and Intravitreal Gas Bubbles

(This work was part of the paper "Computational simulation of altitude-change-induced intraocular pressure alteration in patients with intravitreal gas bubbles" by R. Amini , V.H. Barocas, H.P. Kavehpour, J.P. Hubschman, Retina, In review)

3.1.Summary

The purpose of this study was to explore the impact of altitude on IOP in an eye with an intravitreal gas bubble. A mathematical model was developed to simulate intravitreal gas bubble expansion caused by altitude variations. Mechanical deformation of the eye was simulated using the finite-element model of the ocular globe discussed in Chapter 2. IOP-driven changes in aqueous humor flow were also incorporated into the model. Two cases were considered: ascending from sea level to 3000 ft followed by return to sea level, and ascending to 3000 ft followed by prolonged exposure to 3000 ft. The effect of IOP-lowering medications was also studied by changing the model parameters.

The IOP increase was directly related to the initial bubble size when ascending to 3000 ft was simulated. When prolonged exposure to high altitude was modeled, loss of aqueous humor led to a lower value of intraocular pressure. In a typical simulated case, when the outflow facility was parametrically increased, the predicted IOP rise was reduced by 28%. Theoretical modeling of an eye with an intravitreal gas bubble helps ophthalmologist better evaluate the impact of altitude-induced IOP changes. Our model

suggests that IOP-lowering drugs could help managing altitude-induced IOP changes in presence of intravitreal gas bubbles.

3.2.Introduction

Retinal detachment is an ocular disorder in which parts of the retina, the light-sensitive membrane of the eye, separates from its supporting layers [158]. Retinal detachment may be a result of trauma, inflammatory disorder, or diabetes. Occasionally, retinal detachment is initiated by posterior vitreous detachment which leads to pilling off a piece of the retina and creating a small tear in it. One treatment option for retinal detachment is vitrectomy, in which the vitreous humor is removed from the eye and posterior segment is then filled with a gas bubble (SF_6 or C_3F_8). In some cases (e.g. in pneumatic retinopexy) even without removing the vitreous humor, gas bubbles are injected in the eye during retinal detachment surgeries. Intravitreal gas injection is widely used in retinal detachment surgeries [159-161]. The injected gas bubble eventually reabsorbs into the systemic circulation over 1-8 weeks [162].

The gas bubble may, however, expand when the ambient pressure drops [163-166]. It has been shown that a patient with an intraocular gas bubble who travels to high altitude or flies on an airplane, where the ambient pressure is reduced, experiences an increase in IOP due to bubble expansion [163,164]. Acute IOP increase may lead to discomfort and vision loss due to retinal artery occlusion [164,165] and also presents a risk factor for glaucoma [167].

Human and animal studies [163,166,168,169] have shown the following:

- IOP rises both in non-pressurized air flights [163] and simulated air flights in low-pressure (hypobaric) chambers [166,168,169]. Based on these experimental observations, one may postulate that following the altitude change, a drop in ambient pressure leads to intravitreal gas bubble expansion and subsequent increase in the IOP.

- The increase in IOP is a dynamic phenomenon, i.e., the rate of altitude change or prolonged exposure to low pressure affects the amount of IOP increase [163,166,168,169]. The dynamics of IOP alteration may be a result of aqueous-humor-mediated IOP regulation [57,70].

- The initial size of the intraocular bubble is important in determining the amount of IOP increase following altitude changes. Generally, the larger the initial bubble, the higher the IOP reaches [168].

A mathematical model of intravitreal gas expansion could provide a better understanding of the phenomena observed in experimental observations and help improve the post operative management of patients having to travel to higher altitudes. To our knowledge, this work is the first model on the dynamic behavior of elevation-induced IOP changes observed experimentally. Our mathematical model accounts for the intravitreal gas expansion, the mechanical structure of the corneoscleral shell, and the ocular volume changes due to aqueous humor flow.

3.3.Methodology

The corneoscleral deformation due to IOP changes was evaluated using a modified version of our previous mechanical model (discussed in Chapter 2) [123] created with the commercial finite-element software ABAQUS (Simulia, Providence, RI). Mechanical and geometric parameters were based on published experimental data and were unchanged from our previous work [123]. We increased the pressure on the interior surface of the corneoscleral shell, kept the outside pressure constant, and calculated the volume change. The compliance factor of the corneoscleral shell was then calculated from the linearized pressure-volume curve.

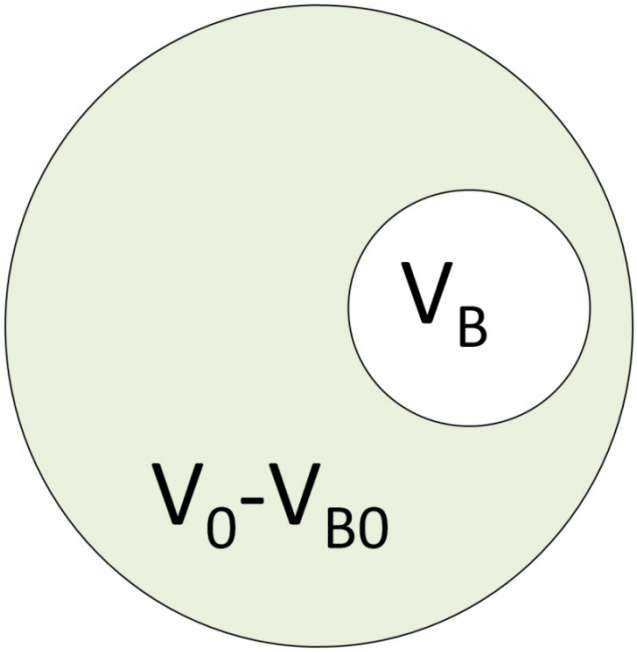

Figure 3.1 Simplified model of an eye in presence of an intravitreal gas bubble. V_B, and V_0-V_{B0} represent the compressible and incompressible components of the model respectively.

When considering elevation changes, it is important to note that there are two different measures of pressure. The *absolute* pressure is the force exerted (by the gas, in our case) on a surface per unit area. The *gauge* pressure is the absolute pressure minus the absolute ambient pressure. Absolute ambient pressure drops with increasing altitude [170]. A mathematical model was further developed to calculate IOP and bubble expansion as the ambient pressure dropped due to an altitude increase. As shown in Figure 3.1, the model was composed of two components: a compressible intravitreal gas bubble and an incompressible region representing the lens, aqueous humor, and vitreous humor. We incorporated the volume change due to bubble expansion and aqueous humor loss into our model.

In addition to expansion of the bubble, volume change in the globe may be effected by changes in aqueous humor inflow and/or outflow. The IOP self-regulatory mechanism, medicated by inflow and outflow variation, was also incorporated into our model. In particular, we introduced changes in the aqueous humor volume by adding two terms in our equations representing an increase in the aqueous humor outflow facility or a decrease in the aqueous humor secretion rate caused by increased IOP. The volume change due to aqueous humor loss was limited to 300 μL, an estimate for the average volume of aqueous humor filling anterior and posterior chambers [41]. A detailed derivation of our mathematical model is presented in the next section.

3.3.1. Derivation of the Model Equations

Following an altitude increase, bubble expansion ΔV_B is compensated by the elastic expansion of the globe ΔV_{globe} and the aqueous humor volume loss ΔV_{loss}:

$$\Delta V_B = \Delta V_{globe} + \Delta V_{loss} \tag{3.1}$$

By using the pressure-volume curve obtained from our finite element of the ocular globe, the compliance factor κ was calculated:

$$\Delta V_{globe} = \kappa \Delta P_{globe} \tag{3.2}$$

where ΔP_{globe} is the change in IOP, that is the gauge pressure of the eye ($P^{in} - P^{out}$). In the finite-element model, we kept the outside pressure constant ($P^{out} = P_0^{out}$) and increased the inside pressure ($P^{in} > P_0^{in}$). ΔP_{globe} was thus defined by

$$\Delta P_{globe} = \left(P^{in} - P^{out}\right) - \left(P_0^{in} - P_0^{out}\right) \tag{3.3}$$

or

$$\Delta P_{globe} = P^{in} - P_0^{in} \tag{3.4}$$

When altitude increased, however, the outside pressure changed:

$$P^{out} = P_0^{out} + \mathcal{P}(h) \tag{3.5}$$

where h was the altitude and $\mathcal{P}(h)$ was defined by barometric formula [170]:

$$\mathcal{P}(h) = (-2.25577 \times 10^{-5} P_0^{out}\, h)^{5.25588} \tag{3.6}$$

In the mathematical model of bubble expansion, for simplicity, we denoted the initial absolute normal IOP P_0^{in} as P_0, and the absolute IOP at high altitude P^{in} as P. Assuming that $P_0 - P_0^{out}$ was 15 mmHg, the normal gauge IOP at the initial altitude, the initial outside pressure P_0^{out} was rewritten:

$$P_0^{out} = P_0 - 15 \tag{3.7}$$

Substituting equation (3.7) into equation (3.5) gave

$$P^{out} = P_0 - 15 + \mathcal{P}(h) \tag{3.8}$$

Equation (3.8) was used to simplify equation (3.3):

$$\Delta P_{globe} = \big(P - P_0 + 15 - \mathcal{P}(h)\big) - (P_0 - P_0 + 15) \tag{3.9}$$

$$\Delta P_{globe} = P - P_0 - \mathcal{P}(h) \tag{3.10}$$

Equation (3.2) was then rewritten using equation (3.10):

$$\Delta V_{globe} = \kappa\big(P - P_0 - \mathcal{P}(h)\big) \tag{3.11}$$

Change in the bubble volume ΔV_B was

$$\Delta V_B = V_B - V_{B0} \tag{3.12}$$

where V_{B0} was the initial bubble volume or bubble volume at the low altitude ($h = 0$) and V_B was the bubble volume at the high altitude. The bubble volume was calculated using Boyle's Law (Robert Boyle, 1627-1691):

$$\frac{V_B}{V_{B0}} = \frac{P_0}{P} \tag{3.13}$$

Combining equations (3.12) and (3.13) gave

$$\Delta V_B = V_{B0}\left(\frac{P_0 - P}{P}\right) = \alpha V_0\left(\frac{P_0 - P}{P}\right) \tag{3.14}$$

with V_0 being initial volume of the globe and α being the ratio of initial bubble volume to initial globe volume.

The rate of changes in the total aqueous humor volume $\frac{d}{dt}\Delta V_{lost}$ was modeled as a sum of changes due to outflow facility [56,57,73] and pseudofacility [56,57]:

$$\frac{d}{dt}\Delta V_{loss} = \mu(P - P_e) - \left[Q_{Aqu} - \lambda\big(P - P_0 - \mathcal{P}(h)\big)\right] \tag{3.15}$$

with μ being aqueous humor outflow facility, P_e being absolute episcleral venous pressure, Q_{Aqu} being the normal aqueous humor inflow rate, and λ being the pseudofacility. The first term of the equation (i.e. $\mu(P - P_e)$) corresponded to aqueous humor outflow and second term of the equation (i.e. $\left[Q_{Aqu} - \lambda\big(P - P_0 - \mathcal{P}(h)\big)\right]$) corresponded to aqueous humor inflow respectively. Combining equations (3.1), (3.11), (3.14), and (3.15) yields the two equations

$$\begin{cases} \kappa P^2 - (\kappa P_0 - \kappa\mathcal{P}(h) - \alpha V_0 - \Delta V_{loss})P - \alpha V_0 P_0 = 0 \\ \frac{d}{dt}\Delta V_{loss} - \mu(P - P_e) + \left[Q_{Aqu} - \lambda\big(P - P_0 - \mathcal{P}(h)\big)\right] = 0 \end{cases} \tag{3.16}$$

To find P and ΔV_{loss}, the equation system (3. 16) was solved numerically using MATLAB ode45 function. Specifically, for a given ΔV_{loss}, the first equation was solved

for $P(\Delta V_{loss})$, and the second equation was used to update ΔV_{loss} over time. The parameters used in the model are listed in Table 3.1.

Table 3.1 Nominal values of parameters used in the mathematical model

Parameter	**Definition**	**Value**	**Unit**	**Reference**
κ	corneoscleral shell compliance	3.115	[μL/mmHg]	†
P_0	initial absolute IOP	775.6	[mmHg]	[54,56,171,172]
V_0	initial globe volume	7211	[mm^3]	‡
P_e	absolute episcleral venous pressure	769.6	[mmHg]	[57,74]*
μ	aqueous humor outflow facility	0.25	[μL/min/mmHg]	[56,57,73]
λ	aqueous humor pseudofacility	0.081	[μL/min/mmHg]	[71]
Q_{Aqu}	aqueous humor inflow rate	1.5	[μL/min]	[56,57]

†Corneoscleral shell compliance calculated from our finite-element model is within the range of published data [30,173,174]

‡Initial volume was calculated from our finite-element model as it was described in Chapter 2 and in our previous paper [123]

*The value reported here is absolute episcleral venous pressure at zero altitude. In higher altitudes, P_e is adjusted to be equal to 9 mmHg gauge pressure.

Table 3.2 Summary of the parameterization studies

Parameter Varied	**Range**	**Comment**
Duration at high altitude	90 min	Simulates a prolonged exposure to high altitude.
α bubble: eye volume ratio	0.25-0.9	Parametric study of bubble size
Outflow facility (% normal)	100-400	Kaufman [175] reports an increase in outflow facility as high as a factor of four when monkeys are treated with pilocarpine.
Aqueous humor secretion rate (% normal)	100-25	Apraclonidine (Iopidine, Alcon Ft. Worth, TX), an α-2 antagonist, lowers IOP by reducing aqueous humor formation.

3.3.2. Case studies

As a test of our model, we simulated a published experiment [163]. The ratio α of bubble volume to globe volume was set to 0.65, and the altitude was increased at a constant rate from zero to 3000 ft over 24 min, followed by a constant-rate descent to zero altitude over the next 24 min.

Once we were satisfied with the model, we performed a series of parametric studies to assess the importance of bubble size and the potential impact of pharmacologically manipulating aqueous humor dynamics. In the first parametric study, we modeled prolonged exposure to high altitude and changed the ratio α of bubble

volume to globe volume. In particular, we simulated flying to 3000 ft in 30 minute and staying in the high altitude for 90 minutes. Simulation was repeated for volume ratio α of 0.25, 0.5, 0.75, and 0.9. In the second study, the outflow facility was increased by 10%, 20%, 50%, 100%, and 300% while rising to 3000 ft was simulated. In the third study, the inflow was decreased by 10%, 20%, 30%, 50%, and 75%. The peak IOP at 3000 ft was calculated for each case. A summary of parametric studies is listed in Table 3.2.

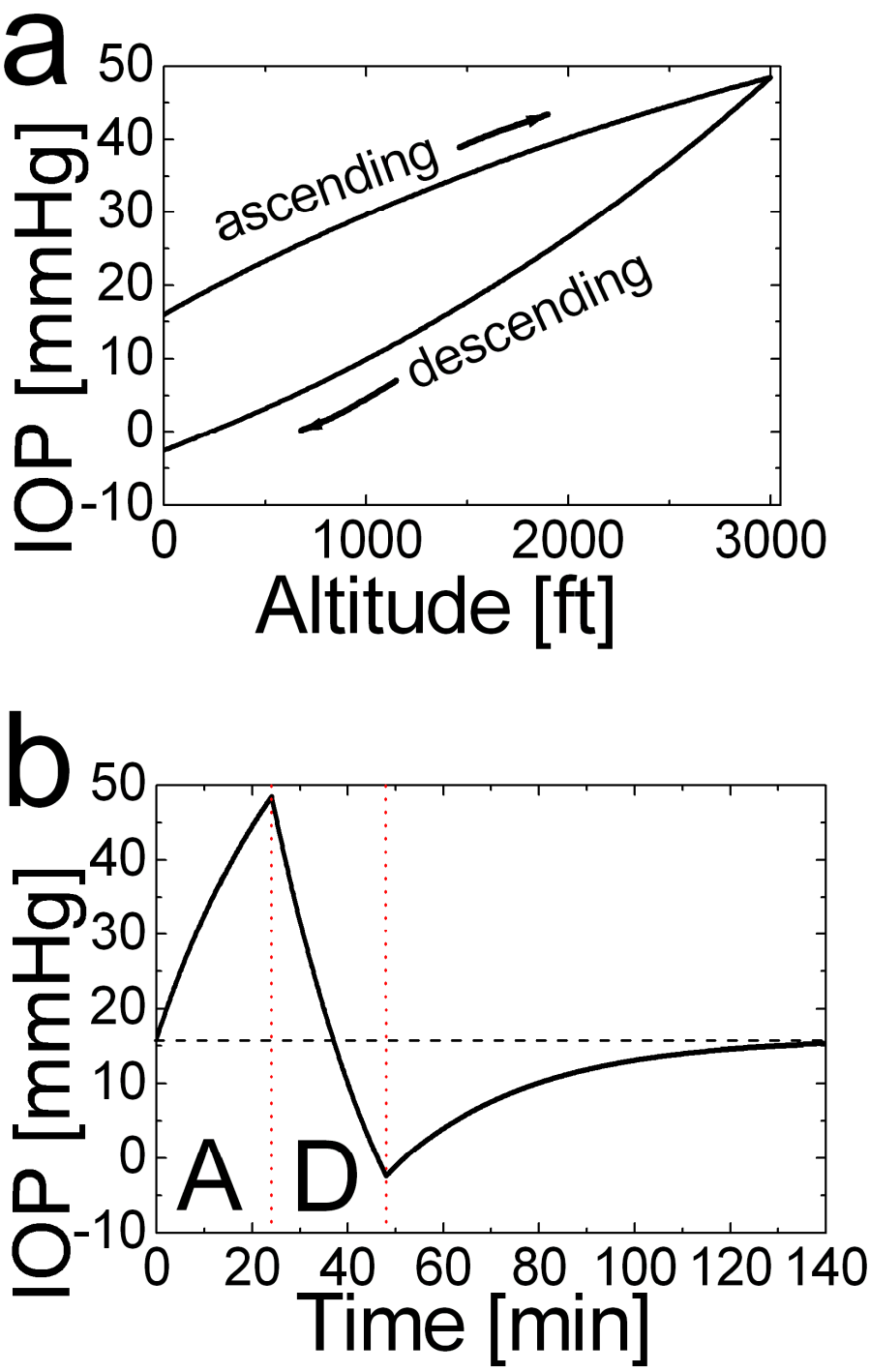

Figure 3.2 (a) IOP versus altitude for a patient with an initial bubble volume of 0.65% of vitreous cavity during ascending to 3000 ft and descending to sea level (b) IOP versus time of the same study during ascending to 3000 ft (A), descending to sea level (D), and prolonged exposure to sea level.

3.4.Results

Figure 3.2 shows the results of validation studies. When ascent to 3000 ft (α=0.65) was simulated, the predicted IOP reached 48.5 mmHg (Figure 3.2a). IOP reached a slightly negative value (ocular hypotony) after descent to sea level due to loss of aqueous humor. As aqueous humor continued to secrete into to the posterior chamber, predicted IOP gradually reached to 97% of its normal value after 96 min exposure to low altitude (Figure 3.2b).

When ascension to 3000 ft and prolonged exposure to high altitude was simulated, IOP reached its maximum value upon reaching maximum altitude but all or part of increase in IOP eventually recovered due to loss of aqueous humor (Figure 3.3). The maximum value of IOP was highly dependent on the initial bubble size. For a small bubble, initially filling 25% of the globe (α=0.25), the maximum IOP was 30.2 mmHg at 3000 ft. When the eye of a patient with a bubble filling 90% of the globe volume (α=0.90) was simulated, the maximum predicted IOP was 50.7 mmHg. As shown in Figure 3.3, for a small bubble (α=0.25), IOP eventually reached its normal value due to aqueous humor loss. The recovery from high IOP was, however, incomplete as the initial bubble size increased because the bubble continued expanding even after all of aqueous humor (300) had been lost from the eye.

Figures 3.4 and 3.5 show how changing our model parameters altered the peak IOP for simulated ascent to 3000 ft in 30 min. When aqueous humor outflow facility was increased, maximum IOP at high altitude was lower (Figure 3.4). For smaller

bubbles, the reduction in peak IOP was present as outflow facility increased for all cases. For the largest bubble (α=0.90), however, outflow increase was effective to reduce peak IOP only up to 100%; after that, due to limited aqueous humor loss, the peak IOP did not change (shown with * on Figure 3.4). Decreased formation of aqueous humor was also simulated. As shown in Figure 3.5, in all simulated cases, decreasing aqueous humor formation led to a slightly lower peak IOP upon reaching 3000 ft. It should be noted that decreasing IOP formation also caused smaller IOP values at the low altitude. In none of the simulated cases did reduced aqueous humor formation cause ocular hypotony.

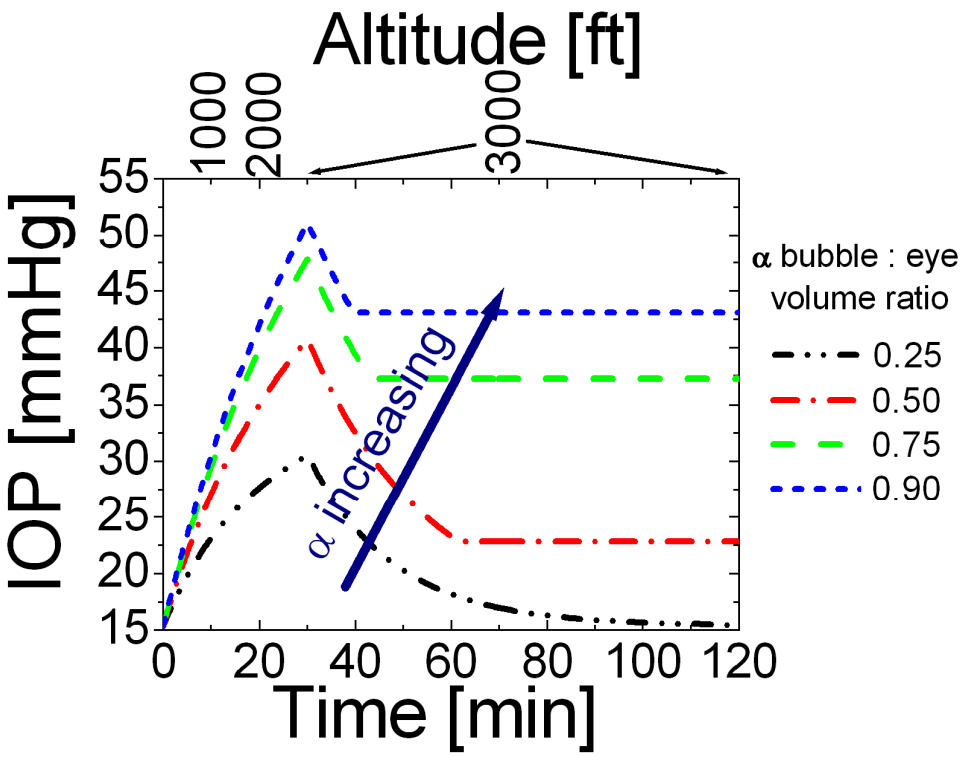

Figure 3.3 The effect of the initial bubble size on the IOP of a patient ascending to 3000ft and staying in high altitude indefinitely.

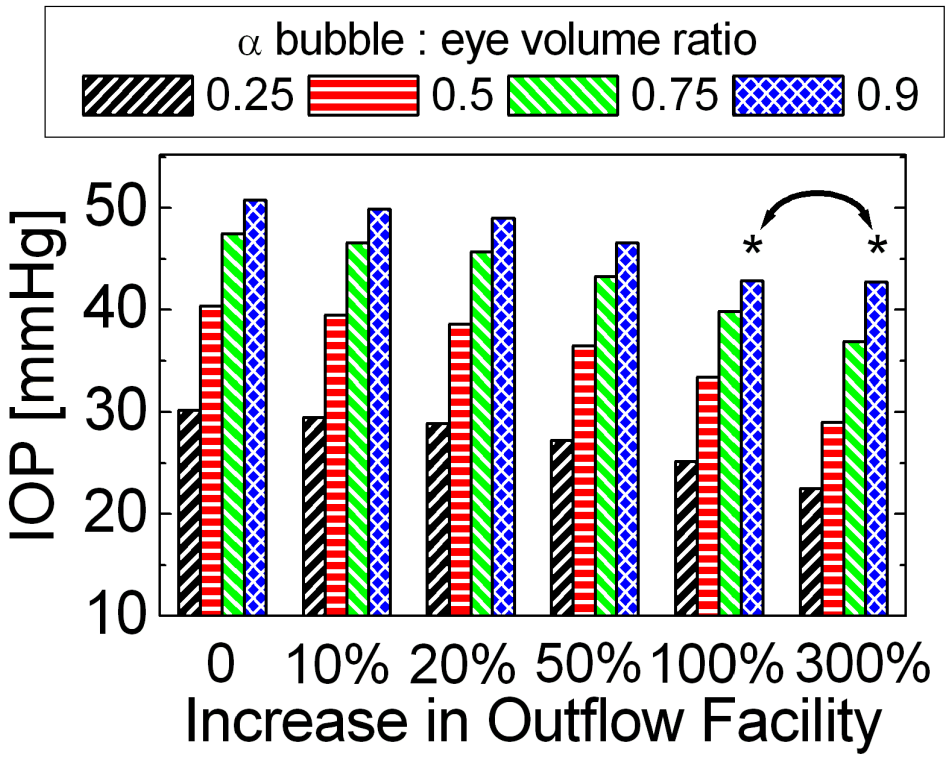

Figure 3.4 Changes in maximum IOP of a patient right after ascending to 3000 ft when aqueous outflow facility is increased

3.5.Discussion

During an altitude change, two driving forces affect the intravitreal gas bubble. As the ambient absolute pressure drops due to an altitude increase, the bubble expands according to Boyle's Law. The tendency for the gas bubble to expand is constrained by the elasticity of the corneoscleral shell causing the IOP to increase as the globe volume increases.

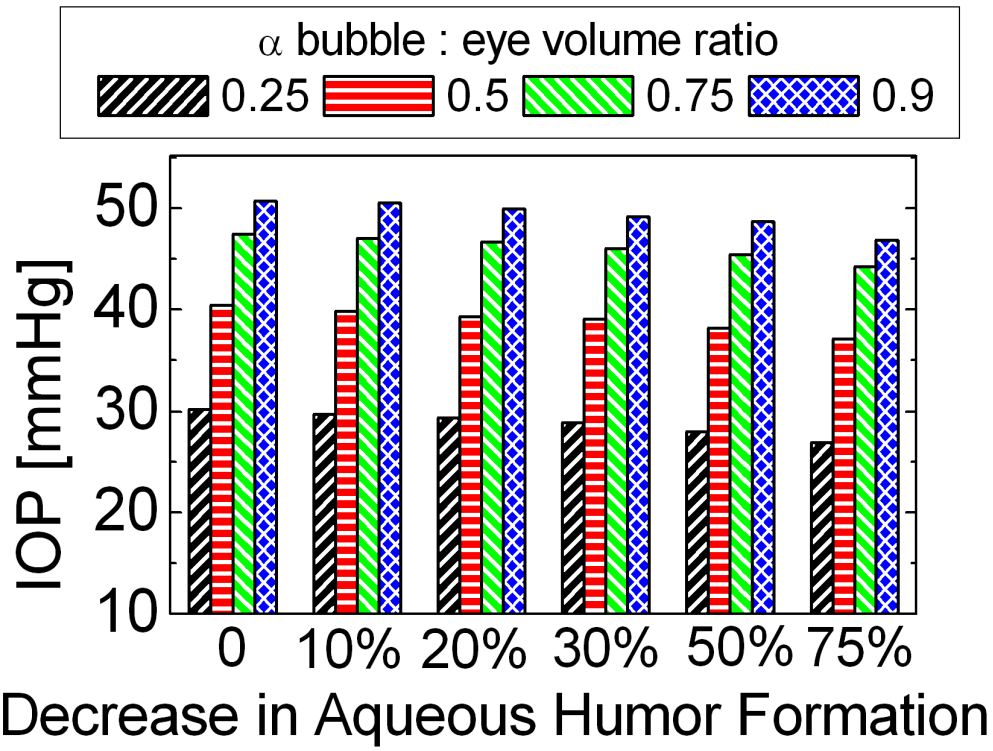

Figure 3.5 Changes in maximum IOP of a patient right after ascending to 3000 ft when aqueous humor formation rate decreased

In a hypothetical case, if the ocular globe were extremely compliant, the absolute IOP would drop to the level of the ambient absolute pressure, and the intravitreal bubble would expand according to Boyle's Law. Since clinical IOP is measured as a gauge pressure, i.e., the difference between the absolute IOP and the absolute ambient pressure, a similar drop in both pressure values leads to an unchanged IOP. In the other limit, if the ocular globe were extremely stiff, the intravitreal bubble would not expand and the absolute IOP would remain unchanged. A drop in absolute ambient pressure not accompanied with a similar drop in absolute IOP, would lead to an increased IOP. In summary, if absolute IOP drops as much as ambient pressure, IOP

remains unchanged, but if absolute IOP does not drop as much as absolute ambient pressure or drops less than absolute ambient pressure, IOP rises.

Our mathematical model was consistent with published experimental data [163]. In particular, the peak IOP during simulated flight was within 1% of the published experimental data [163]. In the published experiment [163], the subject flew in a low-altitude flight with a depressurized cabin. It is noted that the actual altitude at which an airplane flies is often considerably higher than 3000 ft, but the cabin is typically pressurized to a level comparable to the atmospheric pressure at 3000 ft [169].

In our simulations, the initial bubble size played an important role in both the peak IOP and the recovery from increased IOP following prolonged high-altitude exposure. In particular, the larger the initial bubble was, the more IOP increased. For smaller bubbles, following prolonged exposure to high altitude, IOP reached its normal value due to aqueous humor loss, but for larger bubbles, IOP recovery was incomplete due to the finite amount of aqueous humor (i.e., the model predicted that all of the aqueous humor would be driven out of the eye before IOP could return to normal). We concluded that large bubbles may put patients at high risk by keeping IOP at dangerous levels.

Our model showed that certain medications may help control IOP in patients with intravitreal gas bubbles by increasing the aqueous humor outflow facility or decreasing the aqueous humor inflow rate. Over a reasonable IOP range, the outflow facility may be assumed constant [57], so the outflow increases with increasing IOP.

There also exists pseudofacility, a decrease in aqueous inflow with increased IOP [70,71]. In the case of an expanding bubble, increased outflow and decreased inflow both allow the bubble volume to increase with less stretching of the corneoscleral shell. Kaufmann [175] has shown that the outflow facility can increase by a factor of four with intravenous pilocarpine in a monkey model. In our model, we showed that increasing outflow facility decreased peak IOP at high altitudes (Figure 3.4). Therefore, using pilocarpine or similar medications to increase outflow facility may help reduce IOP rise during high-altitude travel. Medications such as Apraclonidine (Iopidine, Alcon Ft. Worth, TX) that decrease aqueous humor formation may also be helpful as shown in Figure 3.5. Since the exact amount of decrease in aqueous humor formation is not experimentally quantified, we considered a range of 10-75% reduction in aqueous humor formation in our parametric studies.

Aqueous-humor-mediated IOP regulation is beneficial only as long as the total aqueous humor volume loss is smaller than the total volume of anterior and posterior chambers combined. In our model, the volume of the anterior and posterior chamber combined was estimated to be 300 μL based on published data [41]. It should, however, be noted that losing the total amount of aqueous humor, the limiting criterion in our modeling assumption, is physiologically unlikely. One should also note that losing aqueous humor could change the lens position, the iris contour, and the anterior chamber angle, which could subsequently lead to acute angle closure and affect IOP. In our model, due to computational limitations, we ignored changes in IOP caused by changes in the anterior chamber angle.

Although our predictions were consistent with published experimental data [163], in interpreting our results one should note that there are still factors that we have not addressed. As was explained in previous chapter, the complex mechanical behavior of peripapillary sclera [23] and optic nerve head [26,138,176] was ignored in the corneoscleral shell modeling. In addition, the mechanical contribution of the lens, zonular fibers, and ciliary bodies were not included in the model. The lens/zonule mechanics observed experimentally [43,155] and clinically [155] could alter our simulation outcomes.

We also assumed that the ocular globe volume change, constrained by the elastic deformation of the corneoscleral shell, was related only to the bubble expansion and aqueous humor loss. We ignored other factors affecting ocular volume following an increase in IOP. In particular, when IOP rises, the ocular blood flow is significantly reduced [156] leading to an ocular globe volume change. Since our current model predicts peak IOP values that are less than arterial perfusion pressure, we would expect that ocular volume changes caused by decreased blood flow would not affect our simulation results significantly.

Although certain limitations exist in our model, it can provide better understanding of the impact of altitude-induced IOP changes in patients with intravitreal gas bubbles. Our model predicted that larger intravitreal gas bubbles would cause a larger increase in IOP at higher altitudes. It also showed that IOP-lowering

drugs, which alter aqueous humor outflow and formation rates, could help in managing altitude-induced IOP changes in presence of intravitreal gas bubbles.

Chapter 4: Mathematical Model of Iris-Aqueous-Humor Interaction during Corneoscleral Indentation

(This work was part of the paper "Reverse Pupillary Block Slows Iris Contour Recovery from Corneoscleral Indentation" by R. Amini and V.H. Barocas, J. Biomech. Eng. doi:10.1115/1.4001256 (American Society of Mechanical Engineers as the copyright holder is acknowledged))

4.1.Summary

Corneoscleral indentation changes the iris contour and alters the angle between the iris and cornea. Although this effect has long been observed, the mechanism by which it occurs remains poorly understood. Previous theoretical research has shown that corneoscleral indentation can deform the eye globe and consequently rotate the iris root. In this work, we studied the fluid-structure interaction between the iris and aqueous humor driven by iris root rotation. The iris root rotation obtained from our previous whole-globe model was used as a boundary condition for a fluid-structure interaction finite-element model of the anterior eye. We studied the effect of two parameters - rotation angle and indentation speed - on the iris contour and aqueous humor dynamics.

We found that posterior rotation of the iris root caused posterior bowing of the iris. After the iris root was returned to its original orientation, the aqueous humor was trapped in the anterior chamber because the iris tip pinned against the lens (reverse pupillary block). After 0.5-2 minutes of simulation, aqueous humor secretion into the posterior chamber and outflow from the anterior chamber allowed the system to return to its original steady state flow condition. The faster or farther the iris root rotated, the

longer it took to return to steady state. Reverse pupillary block following corneoscleral indentation is a possible explanation for the clinical observation that prevention of blinking causes the iris to drift forward.

4.2.Introduction

As discussed in Chapter 1, in numerous cases, indentation of the corneoscleral shell opens the normal, narrowed, or closed anterior chamber angle. These cases include

- Indentation gonioscopy of angle-closure glaucoma [57,124-126].
- Inadvertent opening of the angle during UBM [127,128].
- Manual indentation of the central cornea to open the angle and alleviate acute angle-closure [126,129-131].
- Scleral indentation to improve angle visualization during goniosynechialysis [132].

Further, it has been shown that prevention of blinking leads to anterior drifting of the iris [100,133]. The similarities among these cases suggest a single underlying mechanism. In Chapter 2, we showed theoretically that deformation of the ocular globe during corneoscleral indentation rotated the iris root and subsequently opened the anterior chamber angle. Our whole-globe model, however, did not account for aqueous-humor-iris interaction and lens-iris interaction. In this chapter, we explore the

effect of aqueous humor dynamics on the iris contour and anterior chamber angle when the iris root is rotated, focusing on the hypothesis that reverse pupillary block plays a key role in post-indentation dynamics.

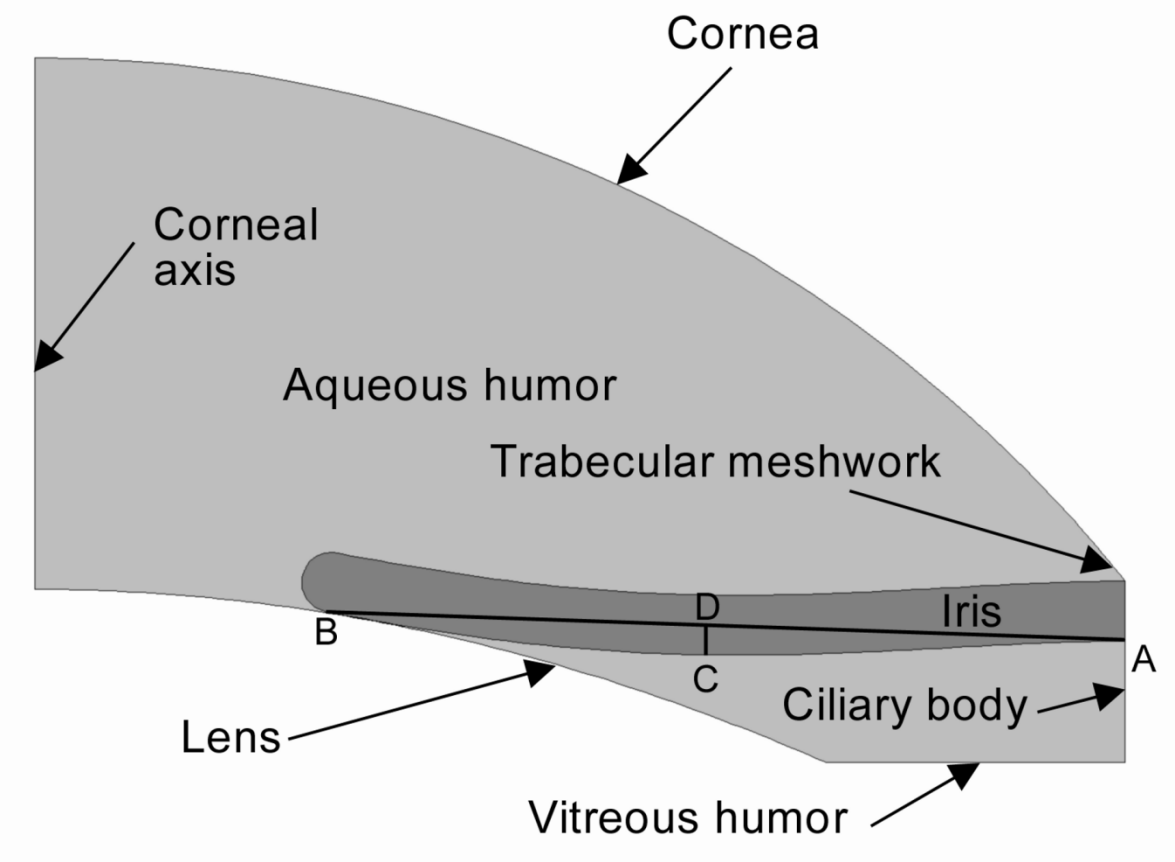

Figure 4.1 Axisymmetric model of the anterior segment. The aqueous humor and iris domains colored light grey and dark grey respectively. The iris concavity [133] (CD) is defined as the maximum distance between the iris pigment epithelium and a reference plane (AB), which connects the most peripheral points of the iris pigment epithelium to the most central ones.

Table 4.1 Mechanical and geometric parameters used in the model

Parameter	**Value**	**Reference**
Cornea radius of curvature (average value)	7.8 mm	[3]
Iris thickness	0.34 mm	[177]
Anterior chamber diameter	12.37 mm	[152]
Anterior lens curvature	10.29 mm	[178]
Lens diameter	9.0 mm	[39]
Iris-zonule distance	0.69 mm	[177]
Modules of elasticity of the iris	27 kPa	[33]
Poisson's ratio of the iris	0.5	[33]
Aqueous humor viscosity	7.5×10^{-4} Pa.s	[52]
Aqueous humor density	1000 kg/m^3	[52]

4.3.Methodology

A computational model of the anterior segment was developed previously [99,120,121] Rotation of the iris root obtained from the whole-globe deformation described in Chapter 2 was employed as an input for the modified version of the code.

4.3.1. Model domains

As shown in Figure 4.1, the model had two physical components: iris and aqueous humor. The governing equations of each component are presented in the following sections. The mechanical and geometric parameters of the iris and aqueous humor for a healthy individual are listed in Table 4.1.

4.3.1.1. The iris: solid domain

The iris was modeled as an incompressible neo-Hookean solid. The governing equations for the iris were

$$\det \mathbf{F} = 1 \tag{4.1}$$

$$\nabla \cdot \boldsymbol{\sigma} = 0 \tag{4.2}$$

where $\mathbf{F}$, the deformation gradient and $\boldsymbol{\sigma}$, the Cauchy stress tensor, were defined by

$$\mathbf{F} = \frac{\partial \mathbf{x}}{\partial \mathbf{X}} \tag{4.3}$$

$$\boldsymbol{\sigma} = -p\mathbf{I} + \mathrm{G}(\mathbf{F}\mathbf{F}^{\mathrm{T}}) \tag{4.4}$$

with $\mathbf{x}$ being the current position of a material point, $\mathbf{X}$ being its rest position, and G being the shear modulus. Gradient and divergence were with respect to the current coordinates. The active contraction of the iris muscles was excluded from the model.

4.3.1.2. Aqueous humor: fluid domain

The aqueous humor was considered an incompressible Newtonian fluid described by the continuity and momentum equations:

$$\nabla \cdot \mathbf{v} = 0 \tag{4.5}$$

$$\nabla \cdot \mathbf{T} = \rho \frac{\partial \mathbf{v}}{\partial t} + \rho \mathbf{v} \cdot \nabla \mathbf{v} \tag{4.6}$$

where $\mathbf{v}$ is AH velocity, ρ is density, and the traction tensor $\mathbf{T}$ is defined by

$$\mathbf{T} = -p\mathbf{I} + \mu(\nabla \mathbf{v} + (\nabla \mathbf{v})^{\mathrm{T}}) \tag{4.7}$$

with p being AH pressure, $\mathbf{I}$ being the identity matrix, and μ being viscosity.

4.3.1.3. Aqueous humor: pseudo-solid domain

Since this model dealt with the free-surface fluid-structure interaction between iris and aqueous humor, the fluid domain changed with the deformation of the iris. In order to determine the fluid domain at each iteration step, the displacement of the fluid domain was calculated via a pseudo-solid method [179]. In this method, the fluid mesh was represented as a linear elastic solid with the flowing governing equations:

$$\nabla \cdot \mathbf{T} = 0 \tag{4.8}$$

$$\mathbf{T} = \boldsymbol{\lambda}\, \mathbf{tr}\,(\mathbf{e})\mathbf{I} + \boldsymbol{\alpha}(\boldsymbol{\nabla}\mathbf{u} + (\boldsymbol{\nabla}\mathbf{u})^{\mathbf{T}}) \tag{4.9}$$

where $\boldsymbol{\lambda}$ and $\boldsymbol{\alpha}$ are Lamé coefficients, and $\mathbf{u}$ the displacement from the rest position, and $\mathbf{e}$ is Eulerian strain tensor are defined by:

$$\mathbf{u} = \mathbf{x} - \mathbf{X} \tag{4.10}$$

$$\mathbf{e} = \frac{\nabla\mathbf{u}+(\nabla\mathbf{u})^{\mathrm{T}}}{2} - \frac{(\nabla\mathbf{u})^{\mathrm{T}}(\nabla\mathbf{u})}{2} \tag{4.11}$$

Gradient is with respect to the current coordinates.

The unknowns for which these equations were solved consisted of $\mathbf{x}$ and p in the solid domain, $\mathbf{v}$ and p in the fluid domain, and $\mathbf{u}$ in the pseudo-solid domain.

Since the rest position $\mathbf{X}$ is known, equation (4.9) could have been written in terms of $\mathbf{x}$ by using equation (4.10) combined with an alternative definition of the Eulerian strain tensor:

$$\mathbf{e} = \frac{\mathbf{1}}{\mathbf{2}}\mathbf{I} - \frac{\mathbf{1}}{\mathbf{2}}(\mathbf{F}\mathbf{F}^{\mathrm{T}})^{-\mathbf{1}} \tag{4.12}$$

4.3.2. Boundary conditions

The boundary conditions of the governing equations of the system are discussed in the following Sections.

4.3.2.1. Iris root

At the iris root, a rotation was imposed as a Drichlet boundary condition. In Chapter 2, we found a range of rotations from 9.7° anterior to 24.5° posterior for various indentation methodologies and forces. As a base case for this study, the iris root

was rotated 10°posteriorly in 50 ms and held at the maximum rotated configuration for another 50 ms. The iris was then rotated back to the pre-indentation position in 50 ms.

4.3.2.2. Axis of symmetry

The corneal axis (shown in Figure 4.1) was the axis of symmetry in the model. The radial displacement of the pseudo-solid mesh $\mathbf{u}_r$ at this axis was set to zero. The symmetry condition dictated that the radial derivative of the axial displacement be zero on the corneal axis. The boundary conditions of the pseudo-solid mesh on the corneal axis were thus

$$\mathbf{u}_r = 0 \tag{4.13}$$

$$\frac{\partial \mathbf{u}_z}{\partial r} = 0 \tag{4.14}$$

In the fluid domain, $\mathbf{v}_r$ the velocity normal to the axis of symmetry was zero, which meant that there was no flow crossing the symmetry axis. The symmetry condition also required that the derivative of the axial velocity $\mathbf{v}_z$ to be zero with respect to the radial direction. These two conditions are shown in the following equations (4.15) and (4.16):

$$\mathbf{v}_r = 0 \tag{4.15}$$

$$\frac{\partial \mathbf{v}_z}{\partial r} = 0 \tag{4.16}$$

Since the iris did not reach the corneal axis, no boundary condition on the iris was necessary here.

4.3.2.3. Cornea

The cornea was modeled as a rigid boundary in the pseudo-solid domain:

$$\mathbf{u} = \mathbf{0} \tag{4.17}$$

No-slip boundary condition was imposed to the flow domain. Since corneal surface was not moving, the no-slip boundary condition yielded to zero velocity on the corneal surface:

$$\mathbf{v} = \mathbf{0} \tag{4.18}$$

There was no boundary condition necessary for the iris since it did not reach the corneal surface.

4.3.2.4. Trabecular meshwork

Similar to the cornea, the trabecular meshwork was modeled as a rigid surface in the pseudo-solid domain:

$$\mathbf{u} = \mathbf{0} \tag{4.19}$$

For the fluid domain, the outflow of 2.5 $\mu L/min$ was strongly imposed on the trabecular meshwork boundary to satisfy the following equation

$$\int_{\Gamma} \mathbf{v} \cdot \mathbf{n} dA = 2.5\ \mu L/min \tag{4.20}$$

There was no boundary condition necessary for the iris at the trabecular meshwork.

4.3.2.5. Ciliary body

Since ciliary muscle is anatomically connected to the iris, a rotation similar to that of the iris root (discussed in section 4.3.2.1) was imposed as a Drichlet boundary condition to the pseudo-solid domain on the ciliary boundary. The only exception was the corner point at which the ciliary and vitreous boundaries connect. For this corner point zero-displacement boundary was imposed.

The ciliary body is the inflow boundary for the fluid domain. Since the pseudo-solid mesh is moving on the boundary, a net inflow of 2.5 $\mu L/min$ was strongly imposed to satisfy the following equation:

$$\int_{\Gamma} \left(\mathbf{v} - \frac{\mathrm{D}\mathbf{u}}{\mathrm{D}\mathbf{t}}\right) \cdot \mathbf{n} dA = 2.5\ \mu L/min \tag{4.21}$$

There was no boundary condition necessary for the iris at the ciliary bodies.

4.3.2.6. Vitreous humor

The vitreous humor was also modeled as a fixed rigid boundary in the pseudo-solid domain:

$$\mathbf{u} = \mathbf{0} \tag{4.22}$$

Rotation of the iris root caused changes in the posterior chamber volume. Since the whole-globe volume was constant, posterior inflow and outflow from the vitreous humor boundary were introduced to make up for domain volume changes due to the rotation. Posterior inflow and outflow during anterior volume change were allowed by imposing a free normal traction condition on the vitreous:

$$\nabla \cdot \mathbf{T} = 0 \tag{4.23}$$

Since the iris did not reach the vitreous humor, no boundary condition on the iris was necessary here.

4.3.2.7. Lens

The lens was treated as a rigid solid surface. Since no accommodation was included in the current model, the total displacement of pseudo-solid domain was zero at this boundary. In order to minimize the numerical errors caused by the extreme mesh distortion around the iris-lens gap, however, there was an additional constraint on the lenticular surface that is discussed in the numerical method section (4.3.3).

The no-slip condition dictated that the velocity of the aqueous humor be zero:

$$\mathbf{v} = \mathbf{0} \tag{4.24}$$

4.3.2.8. Aqueous-humor-iris interface

On the iris-aqueous interface, the no-slip boundary condition was imposed on the flow, and the traction in the fluid was set equal to the traction in the solid domain:

$$(\mathbf{n} \cdot \boldsymbol{\sigma})_{solid} = (\mathbf{n} \cdot \mathbf{T})_{fluid} \tag{4.25}$$

$$\mathbf{v} = \frac{\mathrm{D}\mathbf{x}}{\mathrm{D}t} \tag{4.26}$$

Equation (4.25) is enforced naturally by substituting the fluid for the solid stress in the boundary integral along the iris-aqueous interface. Equation (4.26) is enforced strongly by specifying the aqueous velocity to be equal to the velocity of the iris at the boundary.

4.3.3. Numerical solution

The Galerkin finite element method was used for spatial discretization of the mathematical model. Velocity and displacement were discretized using piecewise biquadratic basis functions, and pressure was discretized using piecewise bilinear basis functions. Finite element meshes were generated using the paving mesh generation software GAMBIT (Fluent Inc., Lebanon, NH). Newton-Raphson iteration and the direct linear solver MUMPS [180] were employed in the solving scheme, and the implicit Euler method was used to solve the initial value problem.

4.3.3.1. Galerkin finite element method

In the Galerkin finite element method, the exact solution of the unknown functions is estimated by a linear combination of finite number of basis functions. For example, in the fluid domain, in which the governing equations are continuity (equation (4.5)) and balance of linear momentum (equation (4.6)), the unknown pressure and

velocity fields are approximated by using the basis functions and series of unknown coefficients:

$$p(\mathbf{x}) \approx p^*(\mathbf{x}) = \sum_{i=1}^{m} p_i \Psi^i(\mathbf{x}) \tag{4.27}$$

$$\mathbf{v}(\mathbf{x}) \approx \mathbf{v}^*(\mathbf{x}) = \sum_{j=1}^{n} \mathbf{v}_j \Phi^j(\mathbf{x}) \tag{4.28}$$

where p^* and $\mathbf{v}^*$are the approximated functions which are defined by the basis functions Ψ^{i} and Φ^{j} along with unknown coefficients p_i and $\mathbf{v}_j$.

By using the method of weighted residuals the equations (4.5) and (4.6) are integrated over a finite domain, Ω.:

$$\mathrm{R}_p^i = \int_\Omega \mathrm{W}^i (\nabla \cdot \mathbf{v}^*)\, \mathrm{d}\Omega = 0 \tag{4.29}$$

$$\mathrm{R}_{\mathbf{v}}^j = \int_\Omega \mathrm{W}^j \left(\rho \frac{\mathrm{D}\mathbf{v}^*}{\mathrm{D}t} - \nabla \cdot \mathbf{T}^*\right) \mathrm{d}\Omega = 0 \tag{4.30}$$

where W^i and W^j are weighting functions and $\mathbf{T}^*$ is approximated value of the stress tensor expressed in term of p^* and $\mathbf{v}^*$.

Equations (4.29) and (4.30) are called the weak forms of the partial differential equations (4.5) and (4.6). In the standard Galerkin finite element method, the weighting functions are the same as the basis functions:

$$\mathrm{R}_p^i = \int_\Omega \Psi^i (\nabla \cdot \mathbf{v}^*)\, \mathrm{d}\Omega = 0 \tag{4.31}$$

$$\mathrm{R}_{\mathbf{v}}^j = \int_\Omega \Phi^j \left(\rho \frac{\mathrm{D}\mathbf{v}^*}{\mathrm{D}t} - \nabla \cdot \mathbf{T}^*\right) \mathrm{d}\Omega = 0 \tag{4.32}$$

Equation (4.32) is rewritten using divergence theorem:

$$\mathrm{R}_{\mathbf{v}}^{j} = \int_{\Omega} \Phi^{j} \left(\rho \frac{\mathrm{D}\mathbf{v}^{*}}{\mathrm{D}t}\right) \mathrm{d}\Omega + \int_{\Omega} \left(\nabla \Phi^{j}\right) \cdot \mathbf{T}^{*} \, \mathrm{d}\Omega - \oint_{\Gamma} \Phi^{j} (\mathbf{n} \cdot \mathbf{T}^{*}) \, \mathrm{d}\Gamma = 0 \qquad (4.33)$$

where $\Gamma = \partial\Omega$.

Similarly, solid and the pseudo-solid equations can be rewritten in weak form:

$$\mathrm{R}_{p}^{i} = \int_{\Omega} \Psi^{i} (\det \mathbf{F}^{*} - 1) \, \mathrm{d}\Omega = 0 \qquad (4.34)$$

$$\mathrm{R}_{\mathbf{x}}^{j} = \int_{\Omega} \left(\nabla \Phi^{j}\right) \cdot \boldsymbol{\sigma}^{*} \, \mathrm{d}\Omega - \oint_{\Gamma} \Phi^{j} (\mathbf{n} \cdot \boldsymbol{\sigma}^{*}) \, \mathrm{d}\Gamma = 0 \qquad (4.35)$$

$$\mathrm{R}_{\mathbf{u}}^{j} = \int_{\Omega} \left(\nabla \Phi^{j}\right) \cdot \mathbf{T}^{*} \, \mathrm{d}\Omega - \oint_{\Gamma} \Phi^{j} (\mathbf{n} \cdot \mathbf{T}^{*}) \, \mathrm{d}\Gamma = 0 \qquad (4.36)$$

where all the terms with "*" are expressed in terms of approximated functions $\mathbf{u}^{*}$and $\mathbf{x}^{*}$.

Piecewise bi-quadratic functions are employed to discretize the velocity and displacement functions. Piecewise bi-linear functions are used to discretize the pressure function.

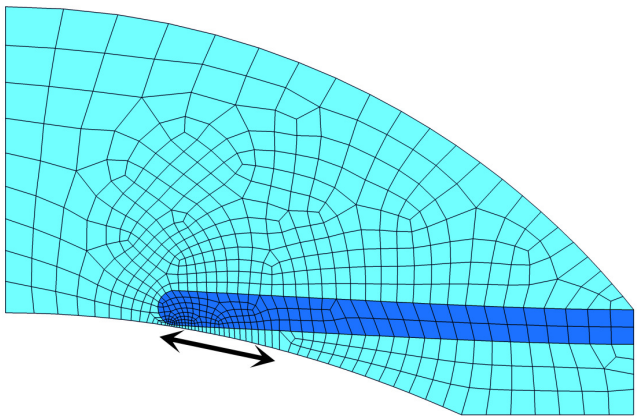

Figure 4.2 Typical mesh generated using GAMBIT (Fluent Inc., Lebanon, NH). The area close to the iris-lens gap, marked with an arrow, is made of only one row of the elements.

4.3.3.2. Solution of the algebraic equation

Spatial discretization of the governing partial differential equations created a set of algebraic equations. The only differential terms remaining were the temporal derivatives of the velocity vector (i.e. $\frac{\partial \mathbf{v}}{\partial t}$). An implicit difference scheme was employed to convert the temporal derivatives to algebraic terms. In the implicit Euler method, the temporal derivatives were approximated by a first-order difference between the values of function at the two consequent time steps:

$$\frac{\partial \mathbf{v}_i^k}{\partial t} \approx \frac{\mathbf{v}_i^k - \mathbf{v}_i^{k-1}}{\Delta t} \tag{4.37}$$

where "i" and "k" are the nodal and temporal indices, respectively.

The resulting nonlinear algebraic equation was solved using the Newton-Raphson method direct solver MUMPS [180].

4.3.3.3. Meshing

The finite element meshes were generated using the commercial software GAMBIT (Fluent Inc., Lebanon, NH). Quadrilateral elements with nine nodes per each (matching the basis functions) were used. Since the geometry of the domain is complex, the paving method was employed in the mesh generation (Figure 4.2), except for the area close to the iris-lens gap. In the fluid domain, in the proximity of the iris-lens gap (marked by an arrow in Figure 4.2) only one layer of elements was used. Since the flow profile is approximately quadratic across the gap, it can be approximated only by one layer of quadratic elements. Using one layer of elements was essential in order to prevent numerical divergence due to the extreme mesh distortion around the iris-lens gap.

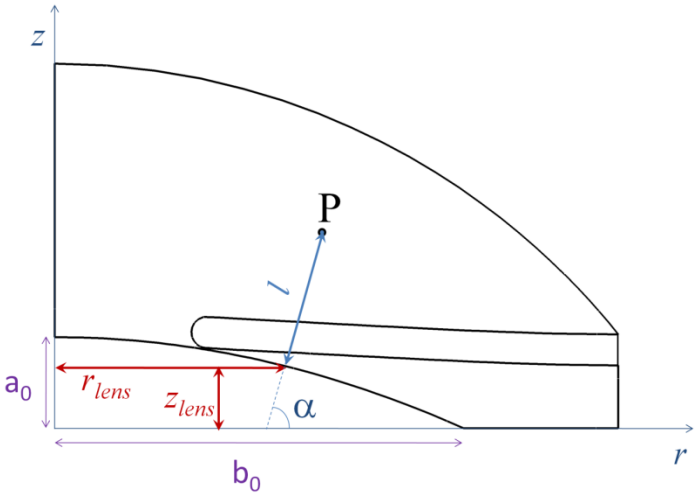

Figure 4.3 Position of the point P, instead of r and z, can be expressed in terms of its distance from the lenticular surface (l) and the radius of the closet point on the lenticular surface to P (r_{lens}).

4.3.3.4. Artificial iris-lens contact force

When the iris root rotates posteriorly, the iris tip moves towards the lens. In theory, the iris tip and the lens would never be in contact due to the infinite lubrication pressure created by aqueous humor in the contact area. During the Newton iteration, however, the iris tip and lens can overlap, leading to failure of the numerical method. To prevent iris-lens overlap, an artificial normal stress was introduced to keep the iris away from the lens at all times [121]. The stress, which enforced a no-contact zone between the lens and iris, was defined by

$$\sigma_{ps} = Ae^{-\frac{d}{\epsilon}}(\mathbf{n}_{lens} \otimes \mathbf{n}_{lens}) \tag{4.38}$$

where d is the shortest distance between the lens and iris, $\mathbf{n}_{lens}$ is a unit vector normal to the lens surface at the shortest iris-lens distance, A and ϵ are adjustable coefficients. The coefficients A and ϵ correspond to how strongly and how far the no-contact region is enforced respectively. A and ϵ can affect the accuracy of the numerical simulation [121]. In this study, they were set in such way that they had the minimal effect on the outcome. The maximum artificial force on the iris during the simulation was less than 0.01 μN, roughly equivalent to a 10^{-4} Pa pressure drop across the gap. As described in the results section, the physical pressure change, when the gap is at its smallest size, is about 1.2 Pa, so the error caused by the artificial contact force is less than 0.01%. Varying A and ϵ by 10% caused no significant change in the results.

4.3.3.5. Coordinate transformation

As discussed in section 4.3.3.4, during the Newton iteration the iris tip and lens can overlap, leading to failure of the numerical method. In addition to iris-lens contact force, a coordinate transformation was employed before every Newton iteration to ensure that the distance of all nodes from the lenticular surface was always a positive number (i.e. none of the nodes would ever enter the lens).

As shown in Figure 4.3, the position of each node P in the domain was expressed using l, its shortest distance from the lens, and r_{lens}, the radius of the closest point on the lens surface to P. To make sure that l was always a positive number new variable $\mathcal{d}$ was defined:

$$\mathcal{d} = \ln(l) \tag{4.39}$$

The initial coordinate system (r, z) was related to the new coordinate system $(r_{lens}, \mathcal{d})$:

$$r = r_{lens} + \exp(\mathcal{d})\cos\alpha \tag{4.40}$$

$$z = z_{lens} + \exp(\mathcal{d})\sin\alpha \tag{4.41}$$

As can be seen in equations (4.40) and (4.41), the distance from the lens (i.e. $\exp(\mathcal{d})$) was always positive in this formulation. Since the lenticular surface was defined as quadratic function, z_{lens} and α were not independent variables and were defined by

$$z_{lens} = a_0 - \frac{a_0}{b_0^2} r_{lens}^2 \tag{4.42}$$

$$\alpha = \arctan\left(-\left(-\frac{2a_0 r_{lens}}{b_0^2}\right)^{-1}\right) \tag{4.43}$$

where a_0 and b_0, the dimension of the lens are shown in Figure 4.3. The coordinate transformation was performed only during the Newton iteration. In particular, the following steps were taken in solving the nonlinear system using Newton iteration and coordinate transformation:

Step 1. An initial guess for the unknown vector $\mathbf{X}$ expressed in terms of the new coordinates (i.e. r_{lens} and d) was chosen

Step 2. The unknown vector $\mathbf{Y}$ expressed in terms of original coordinates (r and z) was calculated from $\mathbf{X}$, using equations (4.40-4.43)

Step 3. The Jacobean matrix $\mathbf{J}$ and the residual vector $\mathbf{R}$ were calculated using the unknown vector $\mathbf{Y}$.

Step 4. $\delta\mathbf{Y}$, the update value for $\mathbf{Y}$ were calculated:

$$\delta\mathbf{Y} = -\mathbf{JR} \tag{4.44}$$

Step 5. $\delta\mathbf{X}$ was calculated from $\delta\mathbf{Y}$ using coordinate transformation:

$$\begin{bmatrix} \delta r_{lens} \\ \delta d \end{bmatrix} = \begin{bmatrix} \frac{\partial r}{\partial r_{lens}} & \frac{\partial r}{\partial d} \\ \frac{\partial z}{\partial r_{lens}} & \frac{\partial z}{\partial d} \end{bmatrix}^{-1} \begin{bmatrix} \delta r \\ \delta z \end{bmatrix} \tag{4.45}$$

Step 6. The unknown vector $\mathbf{X}$ was updated using $\delta\mathbf{X}$

Step 7. Steps 2 to 6 were repeated until convergence.

4.3.3.6. Sliding nodes on the lenticular surface

When the iris root rotates and the iris tip moves, the element along the narrow iris-lens gap may distort extremely. In general, to ensure the accuracy of numerical calculation, rectangular elements are preferred to the angular elements. Extremely angular elements may lead to failure of isoparametric mapping from the physical domain to numerical domain.

As shown in Figure 4.4, to prevent extreme element distortion, we moved the nodes on the lenticular surface to maintain the rectangular shape of the element. In particular, a node on the iris tip was defined as the master node (marked with "M" in Figure 4.4a). A new set of residual equations was defined for the displacement of the follower node (marked with "F" in Figure 4.4a) on the lenticular surface to ensure that F is always at the closest distance to M:

$$\mathrm{R}_r^F = 2(r_F - r_M) - 2\frac{a_0}{b_0^2} r \left(a_0 - \frac{a_0}{b_0^2} r_M^2 - z_M\right) \tag{4.46}$$

$$\mathrm{R}_z^F = z_F - \left(a_0 - \frac{a_0}{b_0^2} r_M^2\right) \tag{4.47}$$

Equation (4.46) was obtained from minimizing the distance l_{FM} between F and M defined by

$$l_{FM} = \sqrt{(r_F - r_M)^2 + (z_F - z_M)^2} \tag{4.48}$$

Equation (4.47) was set to ensure that the F stayed on the quadratic curve defined as the lenticular surface. The remaining nodes on the lenticular surface followed F as defined by the following equations

$$\mathrm{R}_r^i = (r_i - R_i) - c^*(r_F - R_F) \tag{4.49}$$

$$\mathrm{R}_z^i = z_i - \left(a_0 - \frac{a_0}{b_0^2} r_i^2\right) \tag{4.50}$$

where R denotes the original (unreformed) radial position of the nodes and $c^*$was defined by:

$$c^* = \begin{cases} \frac{R_i}{R_F} & \text{if} \quad 0 \le R_i < R_F \\ \frac{b_0 - R_i}{b_0 - R_F} & \text{if} \quad R_F \le R_i \le b_0 \end{cases} \tag{4.51}$$

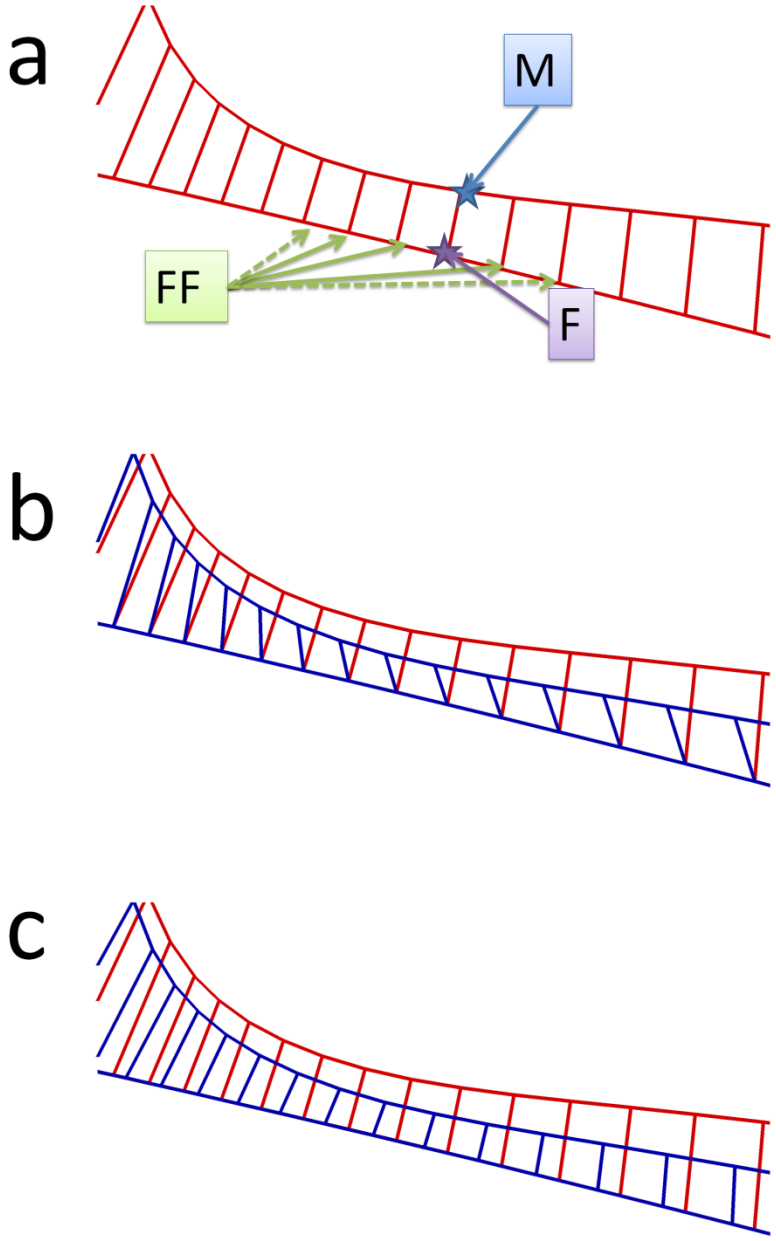

Figure 4.4 (a) The follower node (F) follows the movement of the master node (M) on the iris. The other nodes slide on the lens surface (FF) following the follower node. (b) The elements along the gap distorts dramatically if the nodes do not slide on the lenticular surface. (c) The elements maintain their rectangular shapes when sliding is allowed on the lenticular surface.

4.3.4. Parametric studies

To study the effect of rotation angle and indentation speed, a series of parametric studies was performed. Specifically, in one group of simulations the iris was rotated 6°, 8°, and 12° with the same indentation speed as the base case (10°). In another group of simulations, the iris root rotation was unchanged from the base case, but the indentation was either 50% slower, 33% slower, or two times faster than the base case (50 ms).

We calculated anterior chamber angle (ACA), apparent iris-lens contact, pressure drop ΔP between posterior and anterior chambers, flow through the iris-lens gap, iris concavity, and pupil diameter. To determine iris concavity [133], first the iris chord was drawn from the most central to the most peripheral point of iris epithelium (line AB in Figure 4.1). Then, the maximum distance between the iris chord and the iris pigment epithelium was defined as the iris concavity (line CD in Figure 4.1). The negative sign was assigned to iris concavity when the iris pigment epithelium was posterior to the reference line. Apparent contact length, used by many UBM researchers [31,133], is the distance over which there is no resolvable space between the iris and lens in the UBM image. In the computational model, we estimated the apparent contact as the distance over which the iris was at most 50μm from the lens.

To compare different cases in the parametric studies, we also calculated system recovery time. The recovery time was defined as the amount of time that it took for the

pressure drop ΔP between posterior and anterior chambers to reach 99% of its pre-indentation value after the iris root had returned to its pre-indentation position.

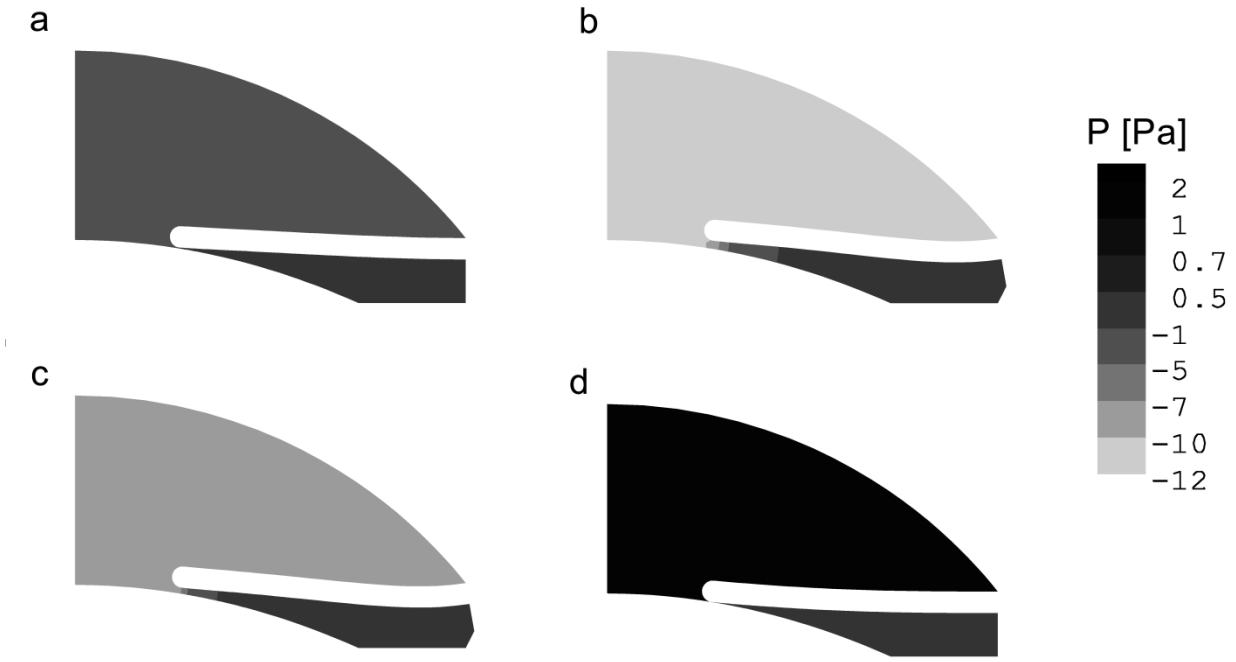

Figure 4.5 Iris profile and aqueous humor pressure distribution (a) before indentation (t = 0) (b) iris root rotated 10° (t = 50 ms) (c) iris root held on the maximum rotated configuration for 50 ms (t = 100 ms) (d) iris rotated back to pre-indentation configuration (t = 300 ms).

4.4.Results

Figure 4.5 shows the aqueous humor pressure distribution and iris profile during the simulation. Before the iris was rotated, there was a slight pressure difference between the posterior and anterior chambers, and the iris was slightly bowed towards the posterior (Figure 4.5a). When the iris root was posteriorly rotated to the maximum value of 10°, the pressure was elevated in the posterior chamber, and the iris bowing was more pronounced towards the iris periphery (Figure 4.5b). After the iris root was kept in the rotated configuration for 50 ms, aqueous humor pressure reached a new value (Figure 4.5c). When the iris root was rotated back to its original position, the posterior chamber pressure became less than that in the anterior chamber. The shape of the iris also changed, with the regions of maximum posterior displacement shifting from the periphery Figure 4.5c) towards the pupil margin (Figure 4.5d).

Figure 4.6 shows the time evolution of calculated parameters for the base case (10° iris root rotation). When the iris root was rotated (t = 0 - 50 ms, marked by "**I**" in Figure 4.6a-f), the ACA increased from 50.3° to 57.8° (Figure 4.6a). During this period of simulation, the iris-lens apparent contact decreased dramatically and reached zero after 22.5 ms. (Figure 4.6b). The pressure applied to the posterior chamber by the iris caused the pressure drop ΔP between posterior and anterior chambers to go up to almost nine times its pre-indentation value (Figure 4.6c). Aqueous humor flow through the gap increased dramatically from 2.5 to 2500 $\mu L/min$ when the iris root was rotated (Figure 4.6d). Since the aqueous humor secretion rate was held constant at 2.5 $\mu L/min$, and

the pressure changes in the simulation (~Pa) were negligibly small compared to the intraocular pressure (~kPa), a gap flow larger than 2.5 $\mu L/min$ indicates volume shift from the posterior to the anterior chambers. Iris concavity also shifted from -0.027 to -0.112 mm showing a more pronounced iris posterior bowing. There was also a slight change in the pupil diameter (0.07 mm) when the iris root was rotated.

When the iris root was held at 10° for 50 ms (t = 50 - 100 ms, marked by "**II**" in Figure 4.6a-f), the ACA increased slightly to 58.0° (Figure 4.6a). Some of other parameters, including apparent contact, iris concavity, and pupil diameter did not change dramatically (Figure 4.6b,e, and f). The pressure drop ΔP between the posterior and anterior chambers also decreased slightly to 9.6 Pa (Figure 4.6c). The rate of aqueous humor flow across the iris-lens gap decreased when the iris was held at 10°for 50 ms, but it was still much larger than its pre-indentation value (2.5 $\mu L/min$), indicating that the volume shift from the anterior to the posterior chamber continued (Figure 4.6d).

When the iris root was rotated back to its pre-indentation location (t = 100 - 150 ms, marked by "**III**" in Figure 4.6a-f), the ACA decreased from 58.0° to 50.7° (Figure 4.6a). Apparent iris-lens contact increased dramatically, showing that a large portion the iris was extremely close to the lens (Figure 4.6b). As the iris rotated forward and pushed on the aqueous humor in the anterior chamber, ΔP dropped to negative values (Figure 4.6c). Had the tight iris-lens contact not been present in the system, the negative ΔP would have caused aqueous humor to flow from anterior to posterior chamber. In

the presence of the contact, however, the iris tip was tightly pinned on the lens (reverse pupillary block [91]), and flow from anterior to posterior chamber was prevented. Therefore, as shown in (Figure 4.6c), the flow across the gap was near zero. A small negative flow occurred because of the artificial force preventing iris-lens contact. The iris concavity was also increased from -0.113 mm to -0.669 mm, showing a less posteriorly bowed configuration (Figure 4.6e). Rotating the iris root forward to its pre-indentation value decreased the pupil diameter (Figure 4.6f).

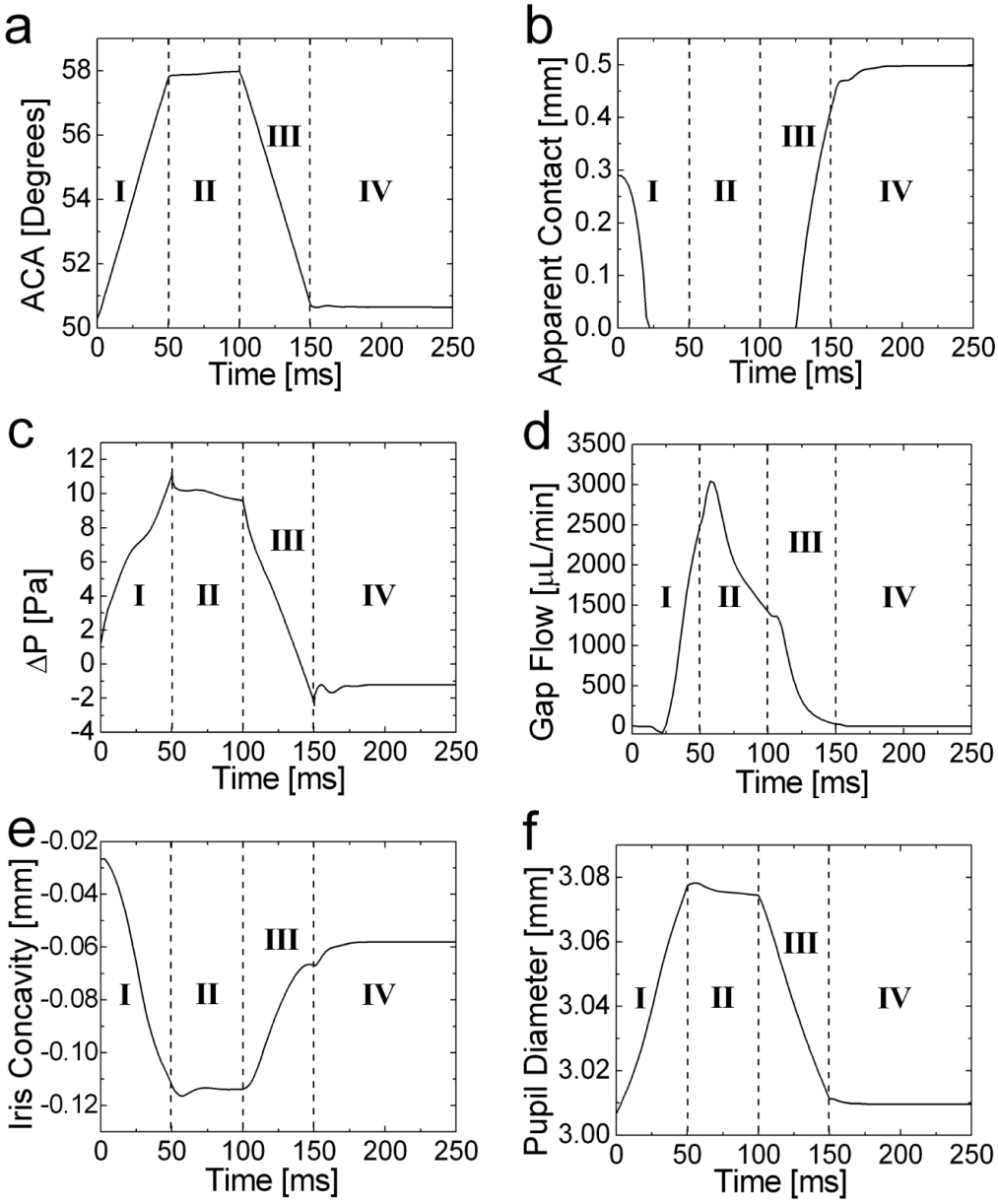

Figure 4.6 Changes in (a) ACA, (b) apparent iris-lens contact, (c) pressure difference between the anterior and posterior chambers, (d) flow through iris-lens gap, (e) iris concavity, (f) and pupil diameter versus time. **I** = posterior rotation of the iris root during indentation; **II** = hold; **III** = anterior rotation of iris root after pressure removed; **IV** = beginning of recovery.

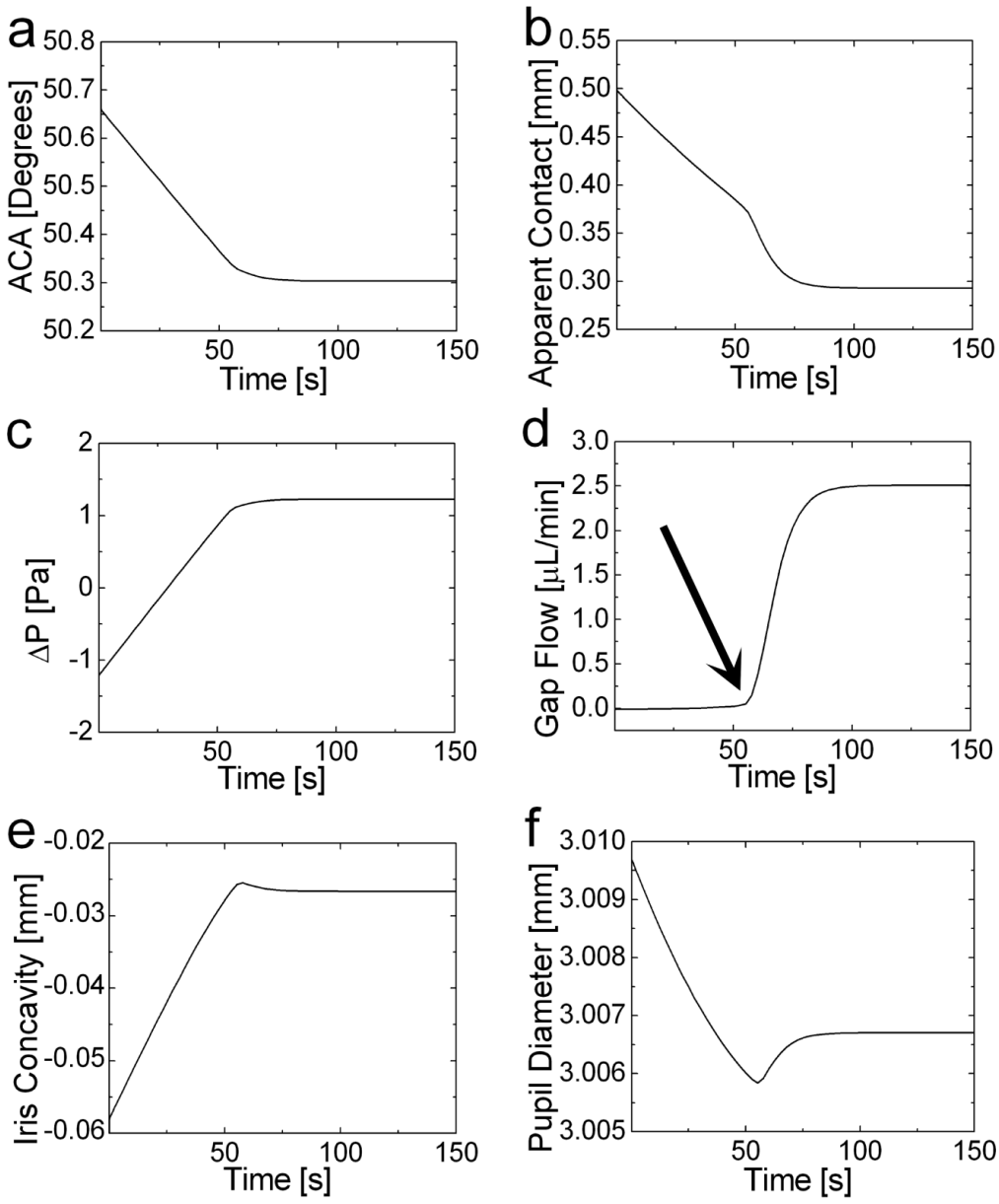

Figure 4.7 Recovery of (a) ACA, (b) apparent iris-lens contact, (c) pressure difference between the anterior and posterior chambers, (d) flow through iris-lens gap, (e) iris concavity, (f) and pupil diameter to their pre-indentation values. Arrow in (d) shows that the pupil remained blocked (negligible gap flow) for almost 55 s after the iris root returns to its pre-indentation position.

All of the calculated parameters returned to their pre-indentation steady-state values over long time (Figure 4.7a-f). The recovery time scale (min), however, was much

larger than the indentation time scale (ms). Therefore, at the beginning of the recovery period ((t ≥150 ms, marked by "**IV**" in Figure 4.6a-f), the calculated parameters were not changing dramatically. A small oscillation in the pressure drop ΔP was caused by the fluid inertia. During the recovery time, all of the parameters returned gradually to steady state values. The only exception was flow across the iris-lens gap, which remained zero due to reverse pupillary block as long as ΔP remained negative. When ΔP became positive due to build up of aqueous humor in the posterior chamber, the reverse pupillary block was removed, and the gap flow rate rose quickly to its steady-state value of 2.5 $\mu L/min$ (marked by an arrow in Figure 4.6d).

Figure 4.8 shows the results of parameterization. Both rotation angle and rotation speed changed the outcome. Figure 4.8a shows that for larger rotation angles, ΔP dropped to lower values when iris root was rotated to its original location. Recovery time was also increased when the rotation angle was larger (Figure 4.8b). When the indentation speed was decreased or increased, minimum ΔP was different for every case. In particular, the faster the iris root was rotated, the smaller ΔP was. As shown in Figure 4.8c and Figure 4.8d, the recovery time was also shorter when the indentation was faster.

Figure 4.9 shows that recovery time versus the total change in the posterior chamber volume for all cases. The slope of the line fitted to data was 2.44 $\mu L/min$, close to the constant aqueous humor secretion rate of 2.5 $\mu L/min$ imposed to the model as the inflow boundary condition.

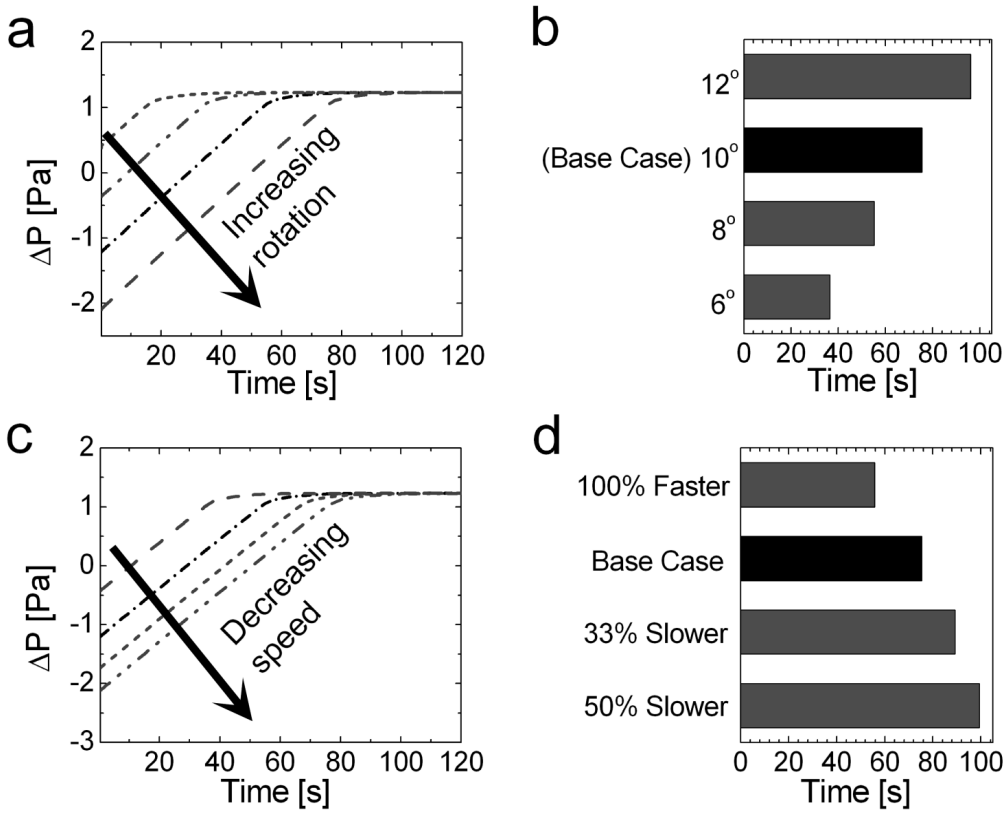

Figure 4.8 (a) Pressure difference between the anterior and posterior chambers versus time with different iris root rotation. Lines are 6°, 8°, 10°, and 12° maximum rotation. (b) Recovery time versus rotation angle. (c) Pressure difference between the anterior and posterior chambers versus time with different indentation duration. Lines are 50%, 67%, 100$%, and 200% of base case rotation speed. (d) Recovery time versus indentation speed.

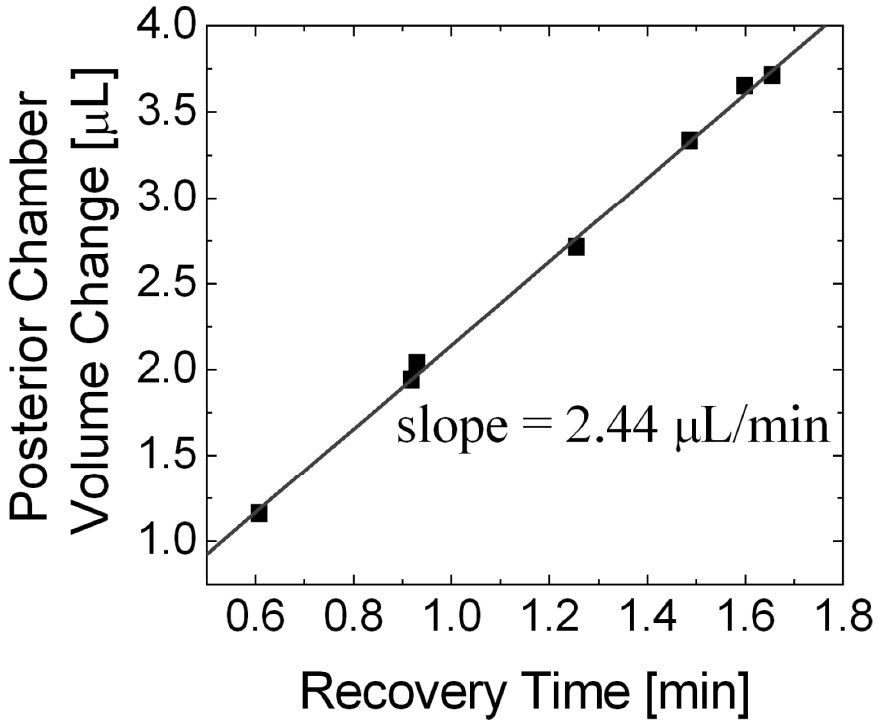

Figure 4.9 Change in the posterior chamber volume versus recovery time. Data points correspond to different cases shown in Figure 4.8.

4.5.Discussion

To our knowledge, this was the first study in which a computational model of iris-aqueous-humor interaction during corneoscleral indentation was created. The posterior rotation of the iris root caused by corneoscleral indentation led to reverse pupillary block. The recovery time from reverse pupillary block was long, on the order of a minute. Since the pupil was nearly completely blocked during anterior rotation and beyond, recovery time was highly dependent on how much volume was displaced during posterior rotation phase.

Our modeling assumptions are based on many simplifications of the complex architecture the iris and the anterior eye. In particular, the active contraction of iris sphincter and dilator muscles was ignored. Activation of the iris smooth muscles can alter the iris contour [99,181] and aqueous humor flow through the iris-lens gap [99] and could change the results of current model. In addition, the inhomogeneity of the iris structure [182] may also alter the outcome. The other major simplification was the exclusion of the lens movement caused either by whole-globe deformation or by accommodation. The fixed position of the lens may introduce some errors to the simulation of corneoscleral indentation. We would expect all of these factors to have quantitative effects on our results (e.g. accelerate or decelerate the recovery) but not to alter the conclusion that reverse pupillary block occurs during recovery from indentation.

Spontaneous blinking occurs on a similar time scale to that of the corneoscleral indention presented in this chapter. Each blink is roughly 80 ms closing, almost no hold, and 200 ms opening [183]. Blinks occur every 2-4 seconds [183-185]. It has been established that prevention of blinking causes the iris to drift forward [100,133]. Similar to corneoscleral indentation, pressurization of the corneoscleral surface during a blink could lead to iris root rotation via whole-globe deformation, and blinking can cause reverse pupillary block. The recovery time is much slower than the frequency of blinking (every 2-4 s), and our results combined with the experimental evidence suggest that some finite-recovery-time process is occurring during blinking and that the prevention

of blinking allows full recovery. Simulation of blinking is discussed in more detail in the next chapter.

Chapter 5: Mathematical Model of Iris-Aqueous-Humor Interaction during Spontaneous Blinking

(This work was part of the abstract "Does spontaneous blinking increase iris-lens contact?" by R. Amini and V.H. Barocas, Proceedings of the ASME 2010 Summer Bioengineering Conference (SBC2010), June 16-19, Grande Beach Resort, Naples Florida, USA (American Society of Mechanical Engineers as the copyright holder is acknowledged))

5.1.Summary

The purpose of this work was to study how iris root rotation due to spontaneous blinking can lead to reverse pupillary block and change the iris contour and aqueous humor flow by using a computational model. In Chapter 2, we showed theoretically that applying pressure on corneoscleral surface can lead to iris root rotation. In this study, we hypothesized that repeated posterior iris rotation, by virtue of the long recovery times seen in Chapter 4, could lead to opening of the angle and posterior displacement of the iris in the dynamic steady state. To test this hypothesis, we modified our finite-element model of the anterior segment (discussed in Chapter 4) to show how the iris root rotation due to blinking changes the iris contour and the aqueous humor flow. We used geometry of an idealized case based on average values of ocular dimensions. We also developed a subject-specific model based on an OCT image of a healthy volunteer. The mechanical parameters of the model were based on published data. Blinking was modeled by posteriorly rotating the iris root in 80 ms and returning it back to the anterior in 200 ms. The frequency of blinking was one blink at every three seconds. To see the effect of rotation angle, four sets of simulation with maximum rotations of 2°,

4°, 6°, and 8° were performed. The iris-lens contact and pressure difference between the anterior and posterior chambers were calculated from the simulation.

When the peak iris root rotation was 2°, the maximum iris-lens contact increased gradually from 0.28 to 0.34 mm in the idealized model and from 0.36 to 0.46 mm in the subject-specific model within eight blinks. After the eighth blink, the repetition of blinking did not make a significant change in the maximum value of the iris-lens contact. When the iris root was rotated 6° and 8° in the idealized model, the pressure difference between the anterior and posterior chambers dropped from a positive value (1.23 Pa) to negative values (-0.86 and -1.93 Pa) indicating the existence of reverse pupillary block. Clinical studies have shown that prevention of blinking leads to anterior drifting of the iris. In our work, we showed that the repetition of iris root rotation caused by blinking may be a possible mechanism to maintain the iris in a more posterior position under normal circumstances.

5.2.Introduction

During every spontaneous blink, the lower eyelid is stationary, and the closure is done by the higher eyelid [135]. In Chapter 2, we showed that applying pressure on the corneoscleral surface led to changes in the anterior chamber angle. In addition, it has been shown clinically [100,133] that, in eyes with pigmentary glaucoma [100,133], narrow angles [100], and healthy controls [100], when blinking was prevented by the presence of an eye cup for UBM examination, the iris bowed to the anterior. These clinical observations suggest that blinking provides a mechanism to push the iris

towards the posterior. Considering all different cases of corneoscleral indentation, one might conclude that during each blink, pressurizing the corneoscleral surface by the lower eyelid leads to iris root rotation and subsequent changes in the aqueous humor flow and the iris contour.

As discussed in Chapter 4, due to reverse pupillary block, even an extremely short change in the iris root location (~ms) can lead to a long recovery time (~min). Spontaneous blinking occurs on a similar time scale to that of the corneoscleral indentation, but a normal individual blinks every 2-4 seconds [183-185] much shorter than full recovery time. Therefore, prior to a full recovery, a new blink rotates the iris root to the posterior. We hypothesize that continuous blinking prevents the full recovery of the iris-aqueous-humor system and keeps the iris more towards the posterior. Therefore, prevention of blinking would allow the iris-aqueous-humor system to recover fully and consequently would lead to anterior drift of the iris. In this chapter we explore this hypothesis by modifying the anterior segment model introduced in Chapter 4.

5.3.Methodology

The finite-element model of aqueous-humor-iris interaction, introduced in Chapter 4, was modified to simulate blinking. The governing equations and all of the boundary conditions except for the iris root rotation were identical in both models. The changes made in the model are discussed in the following sections.

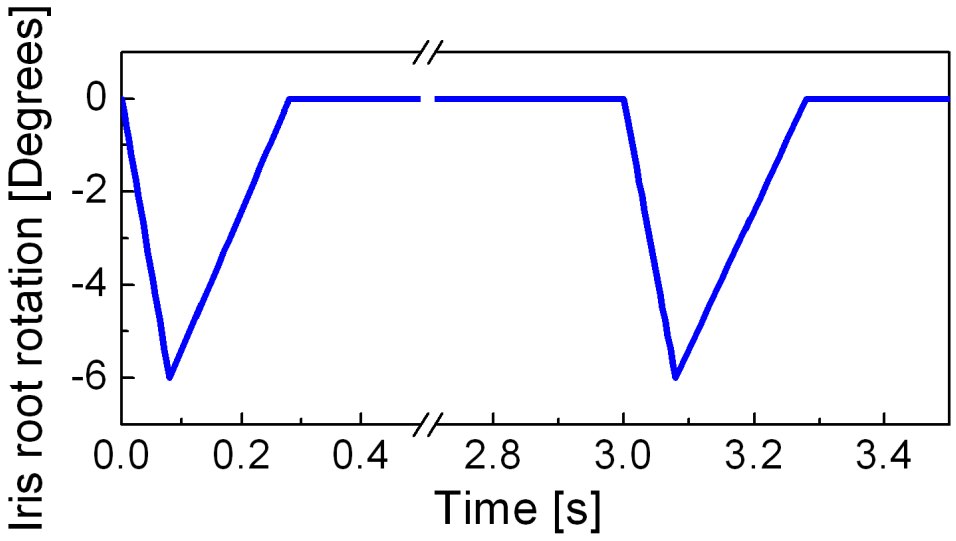

Figure 5.1 Iris root angle during blinking simulation for a typical case of -6 degree rotation (negative sign indicates posterior location). The iris was rotated towards the posterior in 80 ms, rotated back in 200 ms, and held for almost 2720 ms. Blinking was repeated every 3 seconds

5.3.1. Boundary condition on the iris root and subsequent parametric studies

Based on published data [183-185], we simulated each blink as 80 ms closing, no hold, and 200 ms opening, with frequency of one blink per every 3 seconds by imposing the following iris root boundary (Figure 5.1):

Step 1. The rotation angle was imposed as a Drichlet boundary condition to the iris root in 80 ms.

Step 2. The iris root was then rotated back to the pre-blinking (non-rotated) location in 200ms.

Step 3. The iris root was hold at the pre-blinking (non-rotated) configuration for another 2.720 s.

Step 4. Steps 1 to 3 were repeated.

We performed a parametric study of the effect of rotation angle. We repeated the simulation for four different iris root rotation angles. The maximum iris root rotation in the four cases studied were 2°, 4°, 6°, and 8°.

We calculated the iris-lens contact and pressure difference between the anterior and posterior chambers based on the definition discussed in previous chapter.

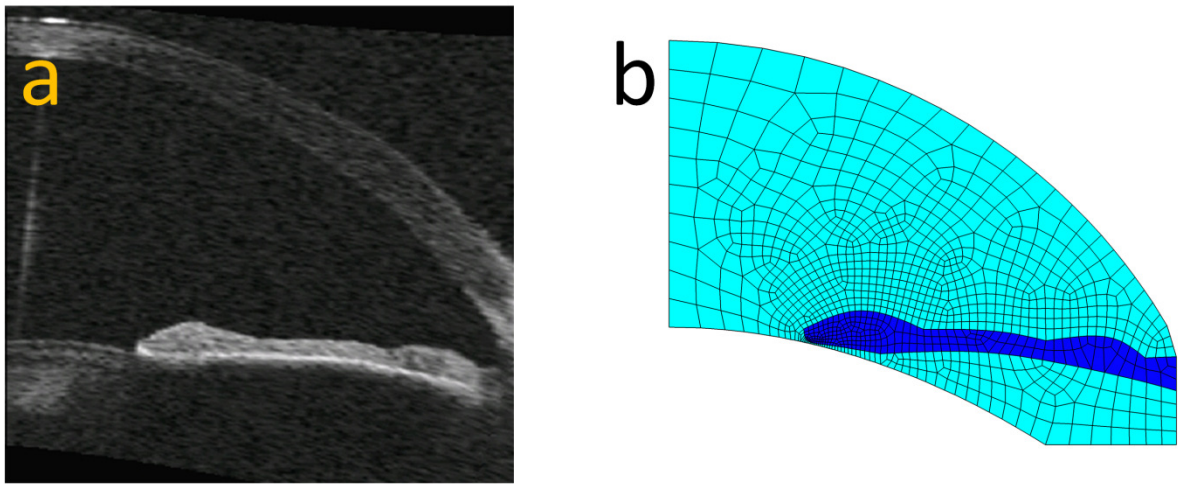

Figure 5.2 A subject specific model was created by converting the domain geometry of the anterior segment of a 42-year-old healthy volunteer taken from (a) an OCT image into (b) finite-element mesh created in Gambit (Fluent, Lebanon, NH) (OCT image from Robert Ritch, New York Eye and Ear Infirmary).

5.3.2. Domain geometry

In addition to the idealized geometry discussed in section 4.3.1 (also shown in Figures 4.1 and 4.2) a subject-specific domain was created based on OCT images of the left eye of a 42-year-old male volunteer (Figure 5.2a). We found the corneal axis by bisecting the line that connects the iris tip on the nasal and temporal sides. The iris boundary and the corneal surface were traced using the image processing software ImageJ [186]. The lenticular surface was created by fitting a quadratic function to three points on the lens: one at the corneal apex, one at proximity of the iris-lens gap, and one at halfway point between the first and second points. The remaining geometrical parameters which were not detectable from the OCT images were taken from the average values listed in Table 4.1. As shown in Figure 5.2b, the paving mesh generation scheme was used to create the finite element meshes using commercial software Gambit (Fluent, Lebanon, NH).

To make the outcome of both subject-specific and idealized models comparable, we required one of the initial parameters to be roughly the same in both models. The parameter chosen was ΔP, aqueous pressure difference between the posterior and anterior chambers, at the steady state when no blinking was present. As the result of different geometry in the two models and same steady state ΔP, the no-blinking iris-lens contact was different in the two models: 0.28 mm in the idealized model and 0.36 in the subject-specific model.

5.1.Results

Figures 5.3 and 5.4 show the iris-lens gap before blinking and immediately after the 10th blink. In both the idealized and subject-specific models, the iris tip became closer to the lens and the iris-lens gap narrowed as blinking continued.

As shown in Figure 5.5, during blinking simulation in the idealized model, both ΔP (aqueous pressure difference between the posterior and anterior chambers, Figure 5.5a) and apparent iris-lens contact (Figure 5.5b) reached to a pseudo-steady-state regime after a few blinks. This trend is shown in Figure 5.5 with dashed line. In particular, when the iris root was rotated 6° and 8° to the posterior, ΔP dropped from 1.23 Pa to -0.86 and -1.93 Pa, indicating the existence of reverse pupillary block.

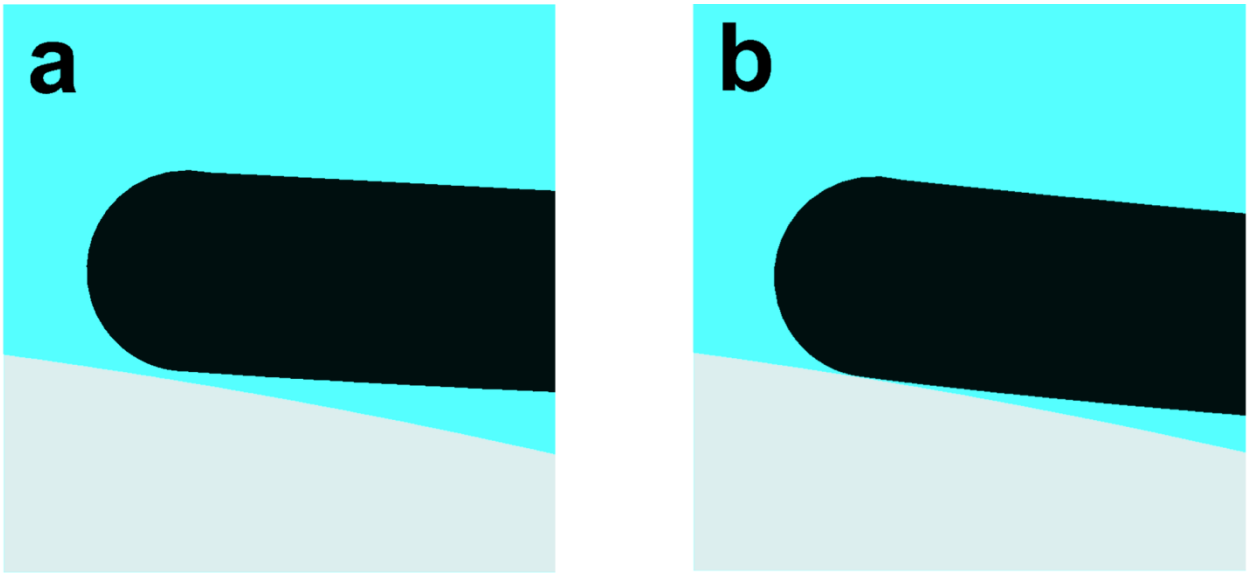

Figure 5.3 Iris-lens gap without blinking (a) and after 10 blinks (b) simulated in an idealized model (6° iris root rotation)

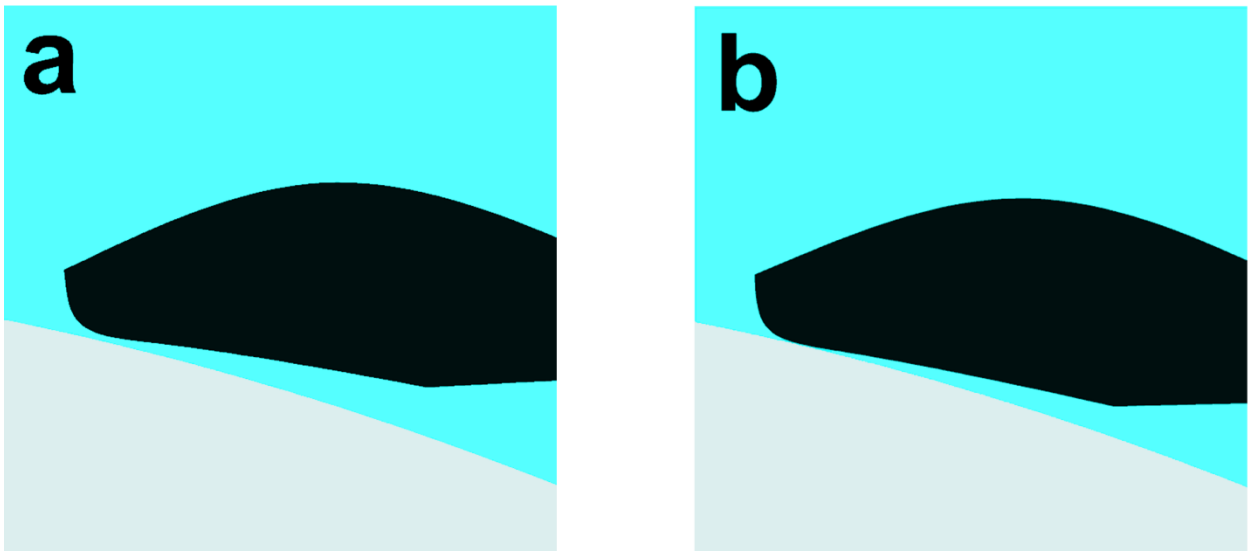

Figure 5.4 The iris-lens gap without blinking (a) and after 10 blinks (b) simulated in a subject-specific model (6° iris root rotation)

Similar to the idealized model, both ΔP and apparent iris-lens contact reached a pseudo-steady-state regime during blinking in the subject-specific model (Figure 5.6). The model predicted a drop in ΔP from 1.07 Pa (without blinking) to -1.03, -2.60, and -4.12 Pa (right after the 10^{th} blinks) when the iris root was rotated 4°, 6°, and 8°, respectively. The higher pressure in the anterior chamber showed the existence of the reverse pupillary block.

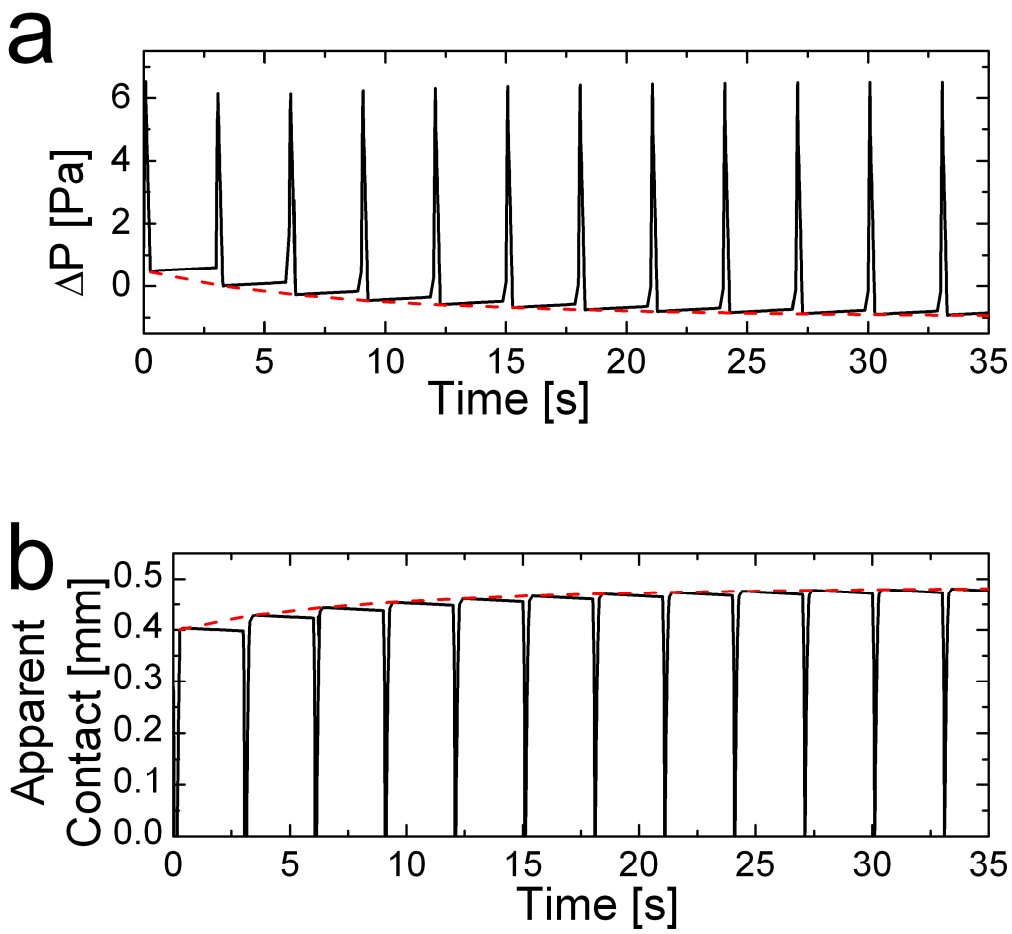

Figure 5.5 **Idealized model.** (a) ΔP, AH pressure difference between the posterior and the anterior chambers, and (b) apparent iris-lens contact as blinking prolongs (6° iris root rotation). The dashed lines show that the values after each blink reaches pseudo-steady-state after a few blinks.

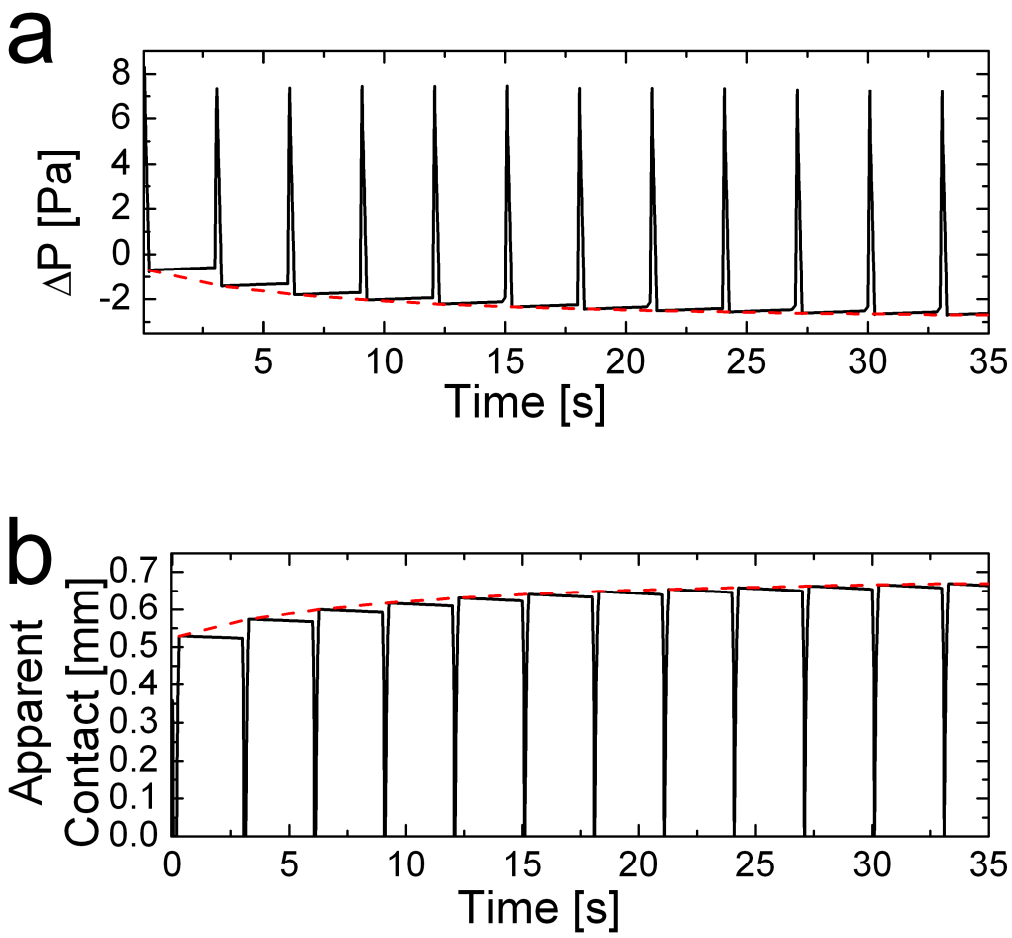

Figure 5.6 **Subject-specific model.** (a) ΔP, AH pressure difference between the posterior and the anterior chambers, and (b) apparent iris-lens contact as blinking prolongs (6° iris root rotation). The dashed lines show that the values after each blink reaches pseudo-steady-state after a few blinks.

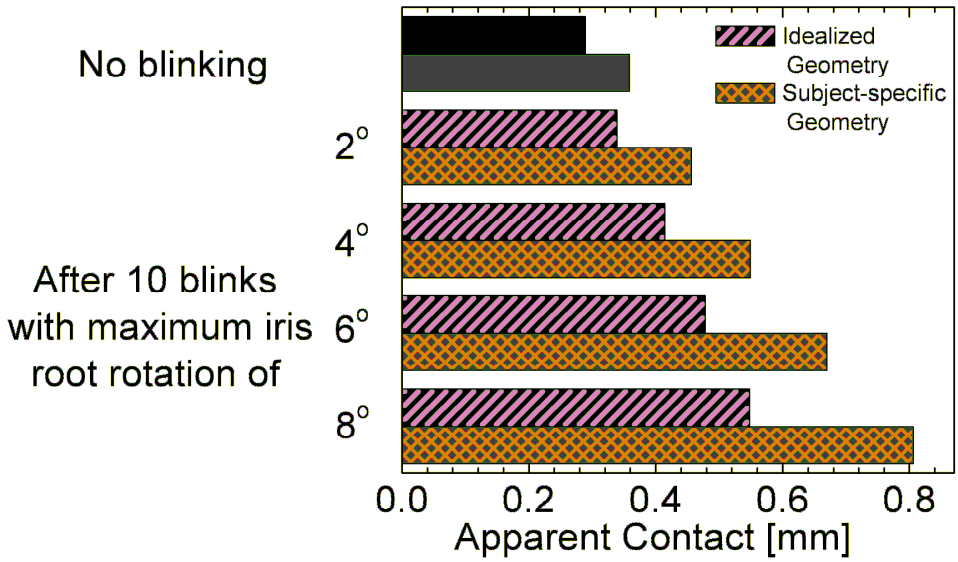

Figure 5.7 The apparent iris-lens contact after 10 blinks when blinking was modeled using different iris root rotations (sparse bars) in comparison to the contact without blinking (solid bars) in idealized (solid black and spare black-pink bars) and subject-specific (solid gray and spare gray-orange bars) models.

Figure 5.7 shows the results of parameterization studies when blinking was modeled. In both idealized and subject-specific models, prolonged blinking led to an increase in the iris root rotation. In the idealized model, when 2°, 4°, 6°, and 8° iris root rotations were simulated, the apparent iris-lens contact increased from 0.28 to 0.34, 0.41, 0.47, and 0.54 mm respectively. In the subject specific model, the apparent iris-lens contact increased from 0.36 to 0.46, 0.55, 0.67, and 0.81 mm when 2°, 4°, 6°, and 8° iris root rotations were simulated, respectively. As summarized in Table 5.1, the increase in the apparent iris-lens contact was more pronounced in the subject-specific model.

Table 5.1 Increase in the iris-lens contact after 10 blinks compared for the simulations using idealized and patient-specific geometries

Iris root rotation	Increase in the iris-lens contact after 10 blinks	
	Idealized geometry	Patient-specific geometry
2	17.2%	27.2%
4	43.7%	53.2%
6	65.5%	86.7%
8	89.9%	124.8%

5.2.Discussion

Our computational model showed that apparent iris-lens contact increased following blinking. Increased iris-lens contact indicated that the iris (at least at the pupillary and mid-periphery margins) was more posteriorly displaced. As long as an individual is awake and conscious, spontaneous blinking occurs every 2-4 seconds, and the iris stays more toward the posterior. We suggest that in the absence of blinking, similar to initial condition of our model, the iris is more anteriorly located. Therefore, when blinking is prevented [100,133], the aqueous-humor-iris system returns to its blink-free steady-state, and the iris drifts forward.

As discussed in Chapter 2, we were not able to model the globe deformation during blinking due to the lack of quantitative experimental data for the blinking-

induced eyelid pressure on the corneoscleral shell. We expected that, similar to other cases of corneal indentation (e.g. indentation gonioscopy), the iris root would rotate to the posterior when the corneoscleral surface is pressurized by lower eyelid during each blink. Our parameterization studies, presented herein, showed that regardless of how much the iris-root was rotated, the iris-lens contact increased. Our blinking results, therefore, should be interpreted qualitatively rather than quantitatively. Based on our model prediction, the apparent iris-lens contact increases following prolonged blinking but the exact amount of increase requires further knowledge of specific experimental data currently unavailable.

Comparison between the subject-specific and idealized models showed that although both models had a similar ΔP initially, the subject specific model had a larger drop in ΔP after 10 blinks. In addition, the relative increase in the iris-lens contact following blinking was more pronounced in the subject-specific model. While quantitative interpretation is rendered impossible by the lack of a precise boundary condition on the iris root in both models, the difference between the two models shows the sensitivity of the problem outcomes to specific geometries. In particular, we conclude that if one's purpose is to predict the qualitative response of the aqueous-humor-iris interaction in the anterior segment, an idealized model is sufficient. If, however, the simulation is intended to predict clinically meaningful numbers, the use of subject-specific models is essential. As it stated previously, the subject-specific models require a better estimate on the boundary condition.

Based on our model prediction, the iris contour and aqueous humor flow are closely related to spontaneous blinking. There may exist a correlation between abnormal blinking and some glaucomatous eyes, in which the irides are positioned abnormally. For example, some functional and/or anatomical abnormalities may lead to increased iris root rotation during each blink. Increased rotation may subsequently lead to abnormal posterior positioning of the iris a risk factor for pigmentary glaucoma.

Chapter 6: Functional Importance of Detailed Iris Structure

(This work was part of the paper "On the quantification of iris concavity" by R. Amini, J.E. Whitcomb, T.S. Prata, S. Dorairaj, J.M. Liebmann, R. Ritch and V.H. Barocas, J Ophthalmic Vis Res, In press, and the abstract "The effect of the Posterior Location on the Iris Concavity During Dilation" by R. Amini , J.E. Whitcomb, M.K. Al-Qaisi, T. Akkin , and V.H. Barocas, Proceedings of the ASME 2009 Summer Bioengineering Conference (SBC2009),June 17-21, Lake Tahoe, California, USA (American Society of Mechanical Engineers as the copyright holder is acknowledged))

(The analysis of the experimental data presented in this chapter was performed independently by Julie E Whitcomb.)

6.1.Summary

The purpose of this study was to examine the effect of the dilator location on iris concavity during dilation in a computational model and an *ex vivo* porcine model. We hypothesized that during pupil dilation, anterior bowing of the iris can be caused by the posterior location of the dilator muscle even in the absence of aqueous humor pressure. Isolated porcine irides 6 hours post mortem were secured at the periphery and immersed in an oxygenated buffer. The dilator was pharmaceutically stimulated with 2.5% phenylephrine and 1% tropicamide. Images of the iris were taken before and after dilation by optical coherence tomography (OCT). A finite element model of a typical pupil dilation experiment was developed. The geometry of the iris and location of the dilator were based on the initial OCT image. The iris was modeled as a neo-Hookean solid, and the active muscle component was applied only to the dilator region.

As expected the pupil diameter increased significantly after the dilator muscle was activated. The OCT images showed an increase in the concavity and a decrease in the chord length after dilation. The computational model agreed with the experiment, showing an increase in the pupil diameter, an increase in the concavity, and a decrease in the chord length. When the simulations were repeated with the dilator distributed over the entire iris thickness, unlike the correct posteriorly located dilator, the iris concavity decreased following dilation. We conclude that the posterior location of the dilator can cause anterior bowing of the iris during dilation even in the absence of aqueous humor flow. This result suggests that the location of the dilator muscle may cause anterior bowing of the iris after aqueous humor pressure has been equalized between the anterior and posterior chambers, for example, as a result of laser iridotomy.

6.2.Introduction

As discussed in Chapter 1, anterior bowing of the iris, resulting in a narrow or closed angle, is often attributed to pupillary block [187,188] even though it is recognized that the angle can close by multiple mechanisms, some independent of pupillary block. In particular, the mechanism by which the iris bows anteriorly during dilation [189] is unclear. It has been shown theoretically [99] that the pressure increase from blocking the steady flow of aqueous cannot explain the increased anterior bowing when the pupil dilates, and Woo [189] reported that the anterior bowing during dilation occurs within seconds, far too quickly for aqueous humor to build up in the posterior chamber.

Yamamoto *et al.* [190] reported that when rabbits with a peripheral iridotomy were dilated, the aqueous flowed *posteriorly*, not anteriorly, which would imply that the anterior-chamber pressure was, in fact, higher. In a human subject with peripheral laser iridotomy, following dilation, the angle narrowed and the iris bowed forward (Figure 6.1). Finally, it has been recently reported [35,36] that iris cross-sectional area and volume changes with dilation are different in narrow-angle patients vs. controls. Taken together, these observations require that non-pupillary-block mechanisms for anterior iris bowing, especially during dilation, be considered. In this chapter, we explore the hypothesis that the anatomy of the iris, specifically the posterior position of the dilator muscle within the iris, leads to spontaneous anterior curvature of the iris during dilation independent of pupillary block**.**

6.3.Methodology

This work included three concurrent studies:

- *In vivo* experiments, in which the curvature of the iris was measured before and after dilation for a set of subjects, all of whom had had laser peripheral iridotomies, eliminating any pupillary block.

- *In vitro* experiments, in which the isolated porcine iris was dilated pharmacologically and imaged via OCT to determine the iris contour.

- *In silico* computer simulations, in which the *in vitro* experiments were modeled using realistic histological geometry and dilator placement.

The *in vivo* experiments were performed by our collaborators Dr. T.S. Prata and Dr. S. Dorairaj at New York Eye and Ear Infirmary and were not part of the work done at the University of Minnesota. They are, however, briefly discussed in the chapter's appendix (section 6.6) due to their relevance to this chapter. The other two methods are discussed in the following sections.

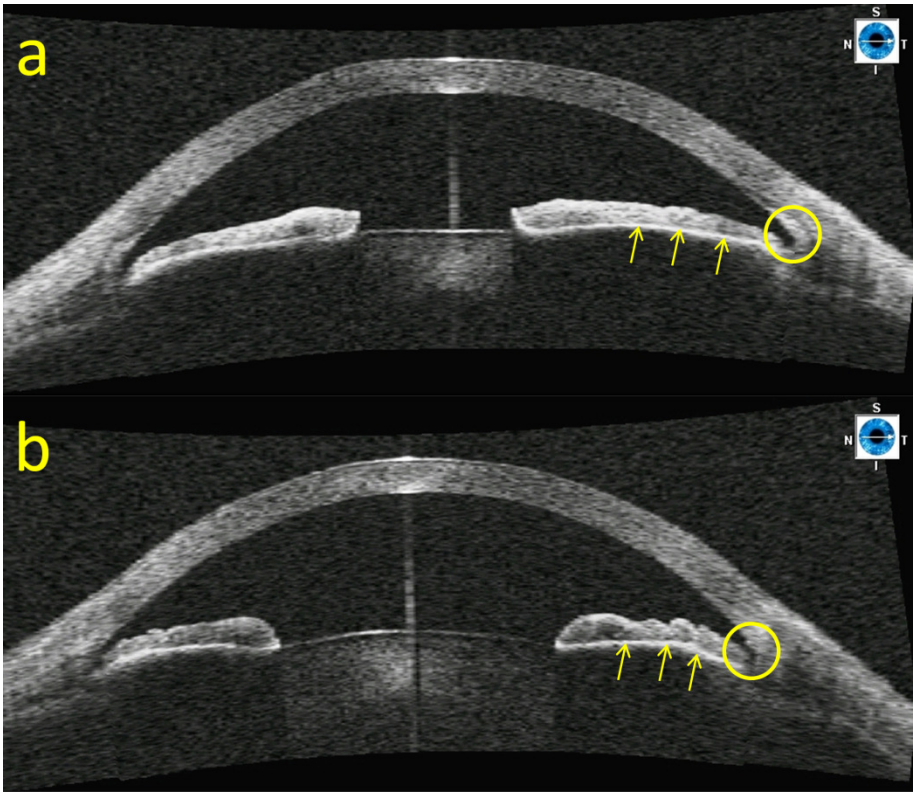

Figure 6.1 Optical coherence tomography (OCT) images of the left eye of a 56-year old Caucasian male with peripheral laser iridotomy, in (a) the light and (b) the dark show the abnormally curved configuration during dilation and narrowing of the anterior chamber angle (images are from Dr. R. Ritch and Dr. T. Prata, New York Eye and Ear Infirmary)

6.3.1. *In vitro* experiments

Experiments were performed on the isolated porcine iris within 6 hours post mortem and prepared as described earlier [37]. The enucleated irides were pinned at two locations on the periphery of the tissue in a Petri dish with a silicone based polymer lining. They were immersed at room temperature in 5 mL of oxygenated Krebs-Ringer buffer to maintain a physiological pH of 7.4. Reference images of the iris were taken via a fiber-based swept source optical coherence tomography (SS-OCT) [191] before the dilation occurred. Figure 6.2 shows the experimental set up used.

Once the initial set-up was complete, 40 µL of 2.5% phenylephrine and 40 µL of 1% tropicamide were introduced into the bath to activate the dilator. Images of the dilation process were taken every 40 seconds. The samples were immersed in the drug solution for 10 – 15 minutes. The initial and final images were subsequently analyzed using ImageJ [186] to calculate the change in pupil diameter, chord length, concavity, and the concavity ratio (described in section 6.3.3). Results were compared using a two-sided paired t-test with equal variance.

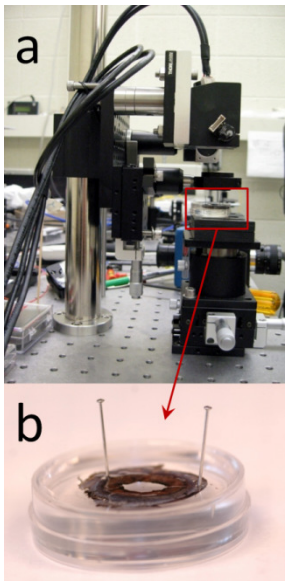

Figure 6.2 Experimental set up (a) OCT imaging system (b) an iris sample pinned in the Petri dish

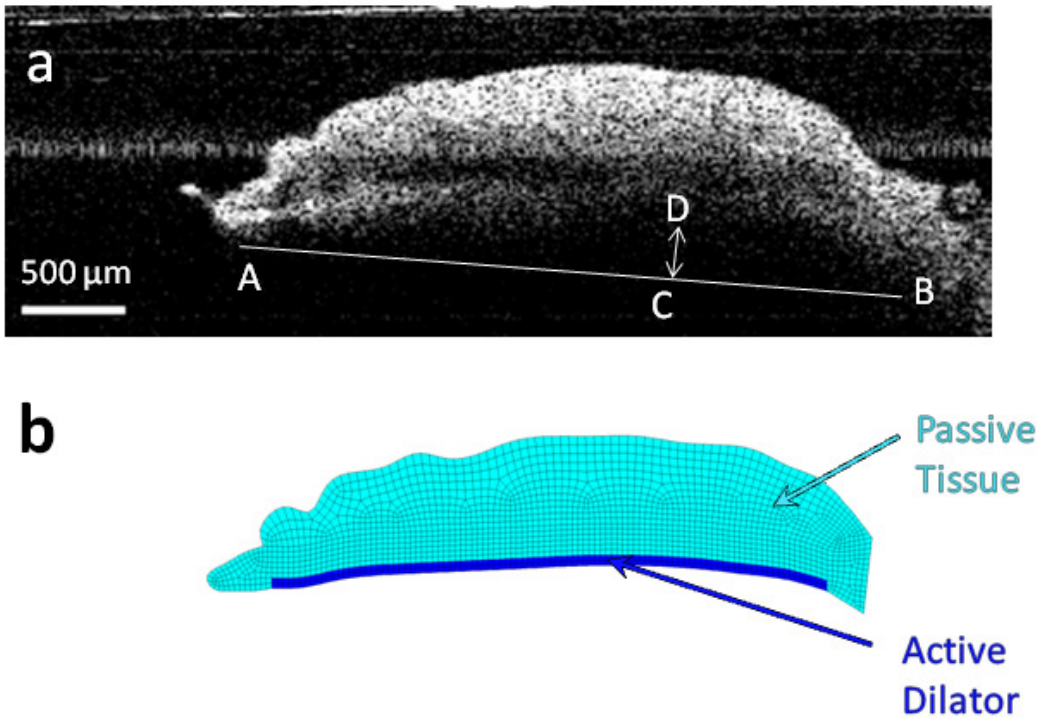

Figure 6.3 (a) OCT image of the iris before dilator is activated. Iris chord length (AB) is defined as the distance from the tip of the iris to the periphery and, iris concavity (CD) is defined as the longest distance between the iris chord length and posterior epithelium (b) Finite element model based on the OCT image of the iris before dilation. The region modeled as the active dilator muscle is marked with the darker color.

6.3.2. *In silico* computer simulations

A realistic finite-element mesh of the iris (Figure 6.3) was constructed based on the initial OCT image. Based on histology of the porcine iris (Figure 1.4), a dilator region, localized to the posterior iris, was constructed.

In the axisymmetric finite-element model, the iris was modeled as a nearly incompressible neo-Hookean solid governed by balance of linear momentum:

$$\nabla \cdot \boldsymbol{\sigma} = 0 \tag{6.1}$$

where $\boldsymbol{\sigma}$ was the Cauchy stress tensor. The derivatives of the stress were taken with respect to the current (moving) coordinate system. The Cauchy stress tensor was defined by neo-Hookean, $\boldsymbol{\sigma}_{\mathrm{NH}}$, and dilator, $\boldsymbol{\sigma}_{\mathrm{D}}$, contributions:

$$\boldsymbol{\sigma} = \boldsymbol{\sigma}_{\mathrm{NH}} + \boldsymbol{\sigma}_{\mathrm{D}} \tag{6.2}$$

The neo-Hookean stress was defined by

$$\boldsymbol{\sigma}_{\mathrm{NH}} = \frac{\mathrm{G}}{\det \mathbf{F}}(\mathbf{B} - \mathbf{I}) + \frac{2\mathrm{G}\nu}{(1-2\nu)\det \mathrm{F}} \ln(\det \mathbf{F})\mathbf{I} \tag{6.3}$$

where, G (= 9 kPa [33]) and ν (= 0.49 [33]) were the shear modulus and Poisson's ratio, and $\mathbf{I}$ was the identity tensor. The deformation gradient $\mathbf{F}$ and left Cauchy-Green deformation tensors $\mathbf{B}$ were defined by

$$\mathbf{F} = \frac{\partial \mathbf{x}}{\partial \mathbf{X}} \tag{6.4}$$

$$\mathbf{B} = \mathbf{F}\mathbf{F}^{\mathrm{T}} \tag{6.5}$$

with $\mathbf{x}$ being the current position of a material point and $\mathbf{X}$ being its rest position. The dilator term $\boldsymbol{\sigma}_{\mathrm{D}}$ was applied only in the dilator region (marked with a dark color in Figure 6.3b). To ensure that the muscle contraction was always in the direction of the non-deformed dilator muscle, $\boldsymbol{\sigma}_{\mathrm{D}}$was defined by σ_{Act}, the scalar muscle contraction stress, and $\mathbf{e_s}$, unit vector representing the direction of non-deformed dilator muscle:

$$\boldsymbol{\sigma}_{\mathrm{D}} = \sigma_{Act}\,(\mathbf{F}\mathbf{e_s}) \otimes (\mathbf{F}\mathbf{e_s}) \tag{6.6}$$

To calculate $\mathbf{e_s}$, natural cubic splines [192] representing the non-deformed dilator were defined based on the coordinates of the points on dilator exported from the finite element mesh. During the simulation, at each point within the dilator domain, $\mathbf{e_s}$ was defined by

$$\mathbf{e_s} = \left(\mathbf{e_r} + \frac{dz}{dr}\mathbf{e_z}\right)\left(\frac{1}{\sqrt{1+\left(\frac{dz}{dr}\right)^2}}\right) \tag{6.7}$$

where $\mathbf{e_r}$ and $\mathbf{e_z}$ are the unit vectors in the r and z direction and $\frac{dz}{dr}$ is calculated from the cubic splines with the same r as the point of interest in the dilator. The traction-free condition was imposed naturally to all of the domain boundaries.

The Galerkin finite element method was employed for spatial discretization of the mathematical model. Biquadratic basis functions were used and the weak form of equation (6.1) was created using the methods discussed in section 4.3.3.1. GAMBIT

(FluentInc., Lebanon, NH) paving mesh generator software was used to generate finite element meshes. The nonlinear algebraic equation was solved using Newton-Raphson iteration and direct solver MUMPS [180].

The model was used to simulate spontaneous contraction of the dilator muscle *in vitro*, based on the experiments described above. The pupil diameter was increased from 5.0 mm to 7.0 mm by applying a muscle contraction stress σ_{Act} in the model.

To assess the importance of the location of the dilator muscle, three simulations were performed. In the first case, the dilator muscle was located on the posterior iris based on the measurements from the histological porcine images. In the second case, to show the importance of the dilator posterior locations, the dilator layer was artificially positioned more towards the anterior iris. Finally, in the third case, the whole thickness of the iris was modeled as the active dilator muscle.

6.3.3. Quantification of the iris concavity

In both experimental and computational studies, we calculated the changes in the iris concavity and iris chord length (Figure 6.3a). The measurement of the iris concavity and iris chord length was previously discussed in section 4.3.4. While iris concavity is an easy measurement to make and provides the necessary basis for comparing two iris contours, it suffers from some significant drawbacks. Because the measurement has units of length, it is dependent on accurate conversion from pixels to

distance, which is not necessarily trivial, especially when images obtained by different modalities (e.g., OCT vs. ultrasound) are to be compared. An additional consequence is that images of the same shape but different size yield different measures (Figure 6.4a and 6.4c). Finally, because only the length of the perpendicular is considered, contours of different curvature can still generate the same concavity (Figure 6.4a 6.4b).

A natural alternative would be the mathematical definition of curvature, namely the inverse of the radius of the circle passing through three points along the contour. This definition would eliminate some of the problems, but it remains a scale-dependent measurement (units of inverse distance). We propose that the best choice is the ratio of the perpendicular length (defining the concavity in current methods) to the chord length. This ratio, which we define as the *concavity ratio*, is independent of scale and thus holds no bias for large vs. small iris size. An additional benefit is that the concavity ratio can be calculated directly from the image without calibration of the pixel size.

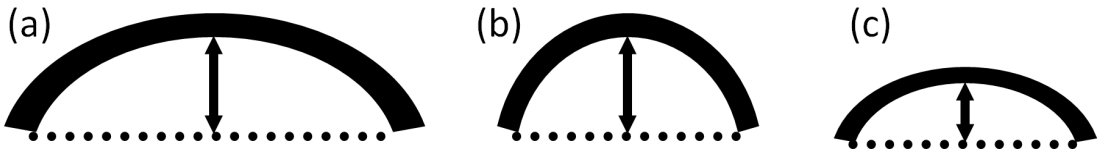

Figure 6.4 Curves (a) and (b) have the same concavity even though (b) is clearly of more pronounced curvature. Curves (a) and (c) are of identical shape except that (c) is smaller, resulting in a lower concavity for curves of comparable curvature. The ratio of concavity to chord length for (a) and (c) is 0.27, and for (c) it is 0.44.

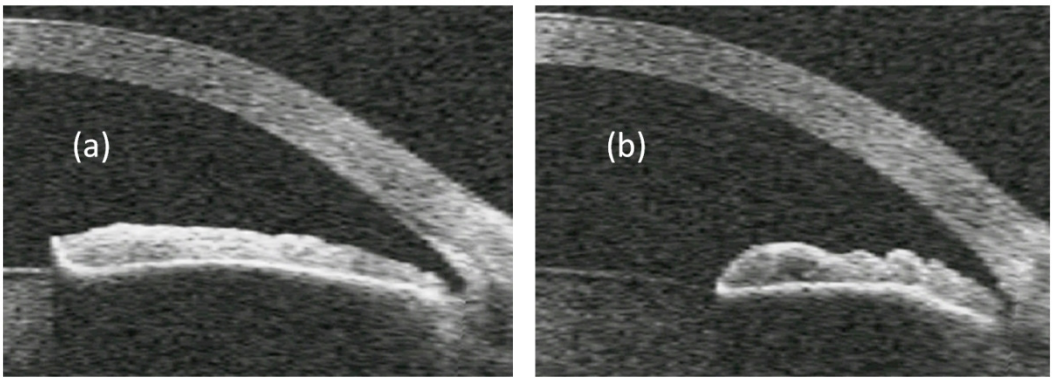

Figure 5.5 OCT image of the iris before and after dilation (details in text). (a) When the pupil is constricted, the iris is bowed slight to the anterior. (b) When the pupil is dilated, the iris becomes more sharply curved, but the concavity changes very little since the main change is in the chord length. The ratio of concavity to chord length, however, increases by 30% (images from R. Ritch, New York Eye and Ear Infirmary).

An example of the proposed measure is given in Figure 6.5, which shows OCT images of a 56-yr-old man who had received a peripheral laser iridotomy for a narrow angle. The image taken in the dark (Figure 6.5b) shows a more sharply curved iris but measures roughly the same concavity (15.4 vs. 15.0 pixels, a difference of 3%). When the concavity ratio is calculated by taking the ratio of concavity to chord length, the difference in shape emerges, with a concavity ratio of 0.063 for Figure 6.5a and 0.082 for Figure 6.5b, a difference of 30%.

Since our experiments were performed on the irides before and after dilation, measurement of iris concavity ratio was beneficial to better analyze our experimental data as discussed in the next section. In general, if one's intent were to quantify displacement, then the iris concavity would be the appropriate measurement. If,

however, one's intent is to quantify changes in shape, then a scale-independent measure of shape, such as the concavity ratio, should be used.

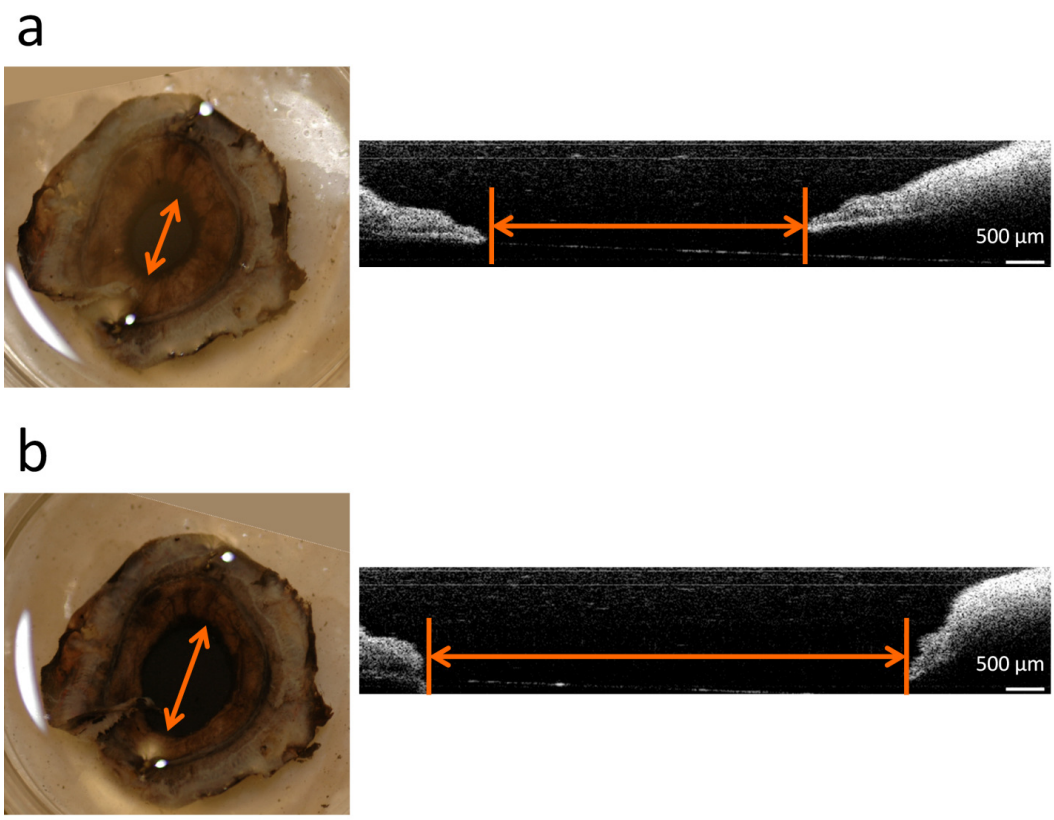

Figure 6.6 Images taken (a) before and (b) after adding 40 µL of 2.5% phenylephrine and 40 µL of 1% tropicamide to the bath solution showed that in both imaging the anterior side of the iris using a digital camera (left) and the cross sectional area of the iris using OCT imaging system (right) the pupil diameter (showed with arrows) have increased following the addition of the drugs.

6.4.Results

Figure 6.6 shows a typical iris before (Figure 6.6a) and after (Figure 6.6b) the drugs were added to the bath. The pupil diameter was clearly increased in this experiment (as shown with arrows both in top view and OCT cross-sectional view) indicating the activation of dilator muscle and possibly the relaxation of the sphincter muscle. As shown in Figure 6.7, pupil diameter increased from 2.82 ± 0.1607 mm (mean ± 95 % CI, n = 30) to 3.72± 0.210 mm ($p < 0.001$) following addition of the 40 µL of 2.5% phenylephrine and 40 µL of 1% tropicamide to the bath solution.

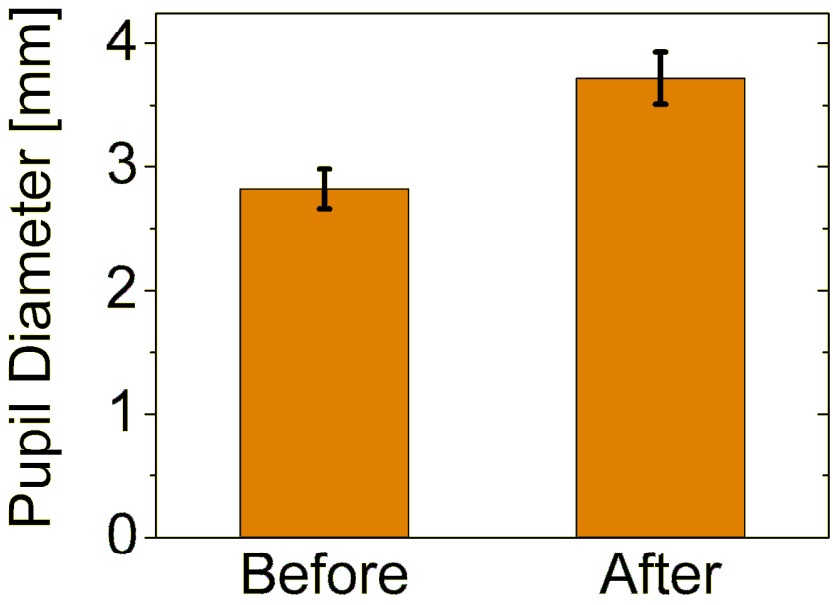

Figure 6.7 Pupil diameter before and after stimulation. The diameter was significantly increased ($p < 0.001$ for two-sided paired t-test) indicating the activation of the dilator muscle (bars are 95% confidence interval, n = 30).

Iris concavity (Figure 6.8a) increased from 0.176 ± 0.072 mm (mean ± 95 % CI, n = 30) to 0.1856 ± 0.0129 mm (p = 0.4966) and iris chord length (Figure 6.8b) decreased from 2.68 ± 0.21 mm (mean ± 95 % CI, n = 30) to 1.1697 ± 0 .0703 mm (p < 0.001) following activation of the dilator muscle. As shown in Figure 6.8c, the iris concavity ratio increased from 0.126 ± 0.013 mm (mean ± 95 % CI, n = 30) to 0.17 ± 0.008 mm (p =0.0036) following the addition of the drugs to the bath.

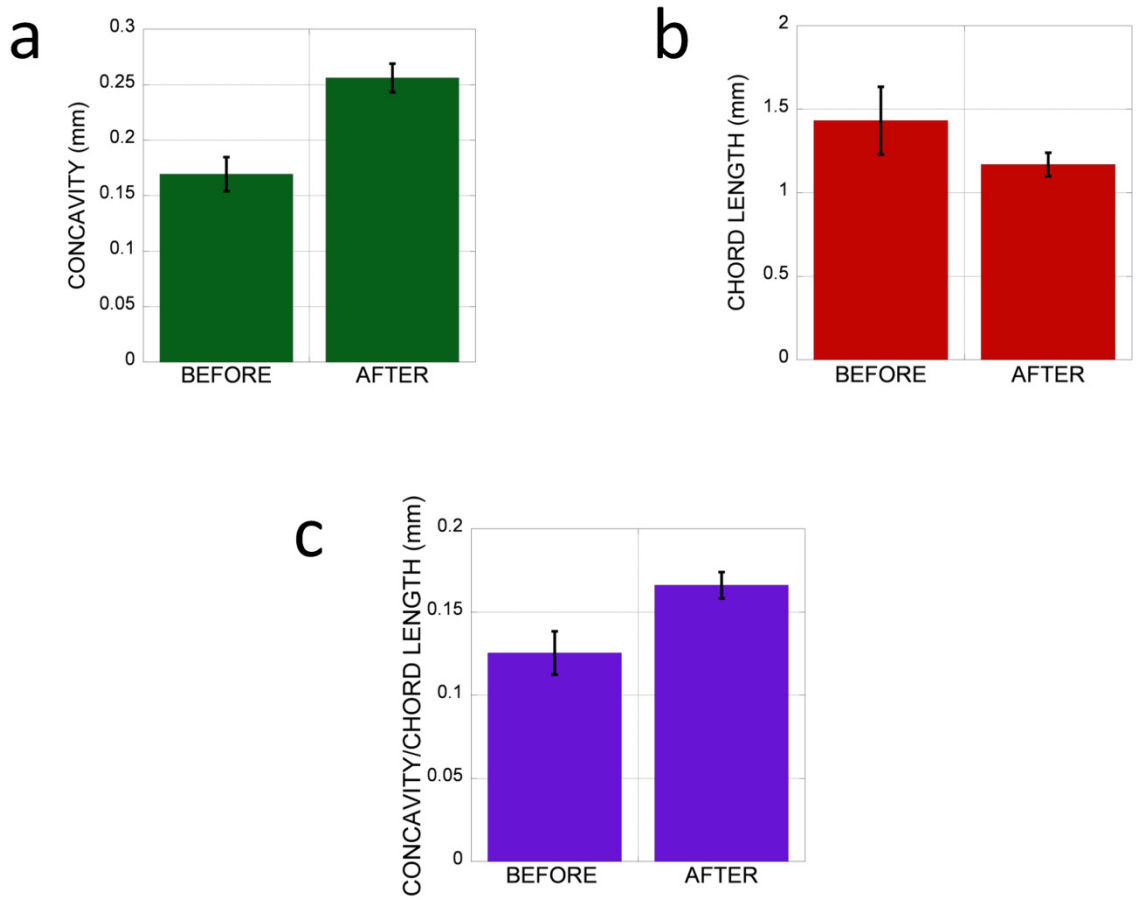

Figure 6.8 (a) Iris concavity did not change significantly (p= 0.043) after dilation. (b) Iris chord length decreased significantly after dilation (p<0.001). The change in (c) iris concavity ratio was more significant (p= 0.004) than iris concavity (bars are 95% confidence interval, n = 25).

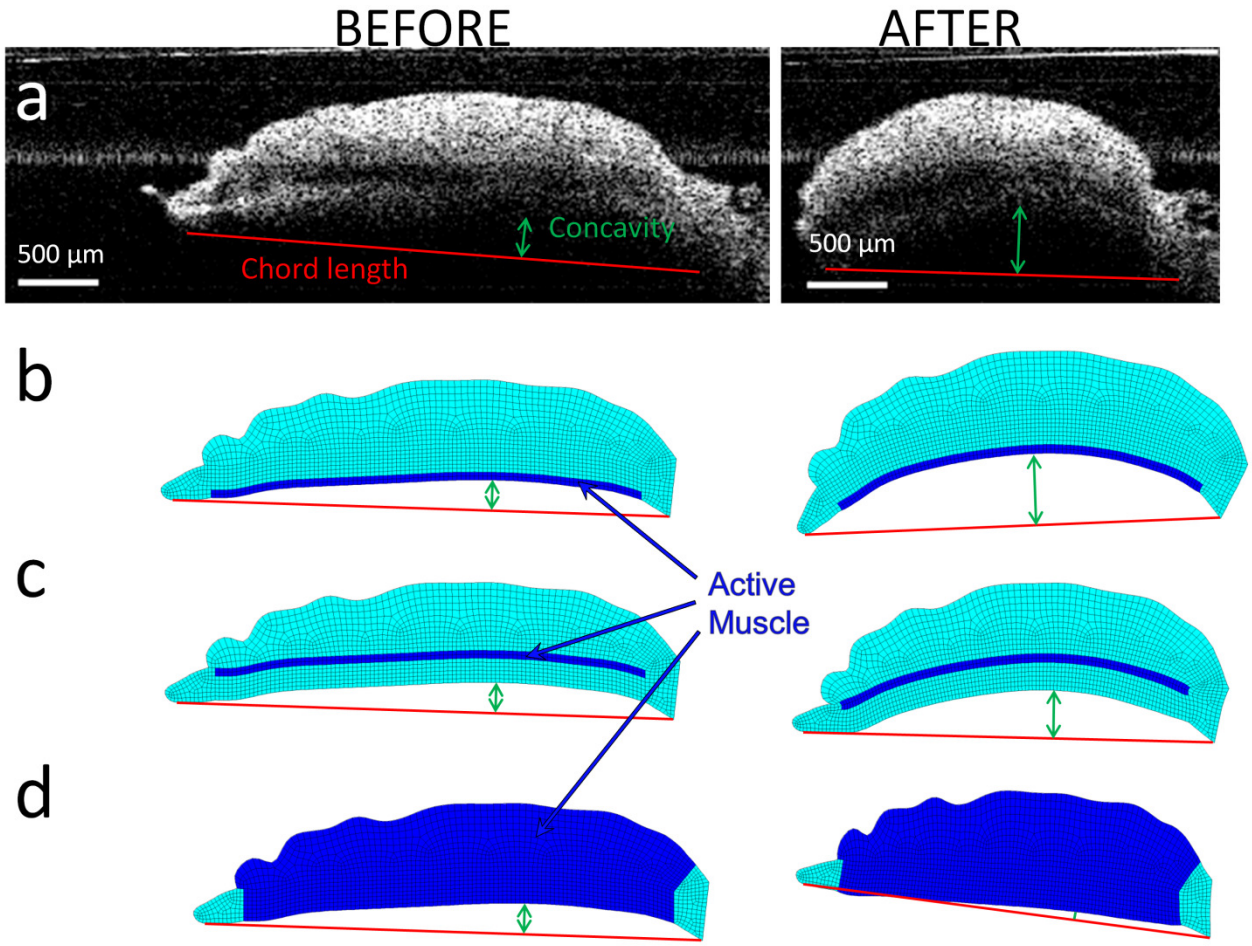

Figure 6.9 Iris chord length and concavity before (left) and after (right) dilation in (a) a typical experiment, (b) a realistic model of the iris with the dilator muscle in the posterior, (c) an artificial model in which the dilator was positioned anteriorly, and (d) an artificial model in which the dilator was thickened.

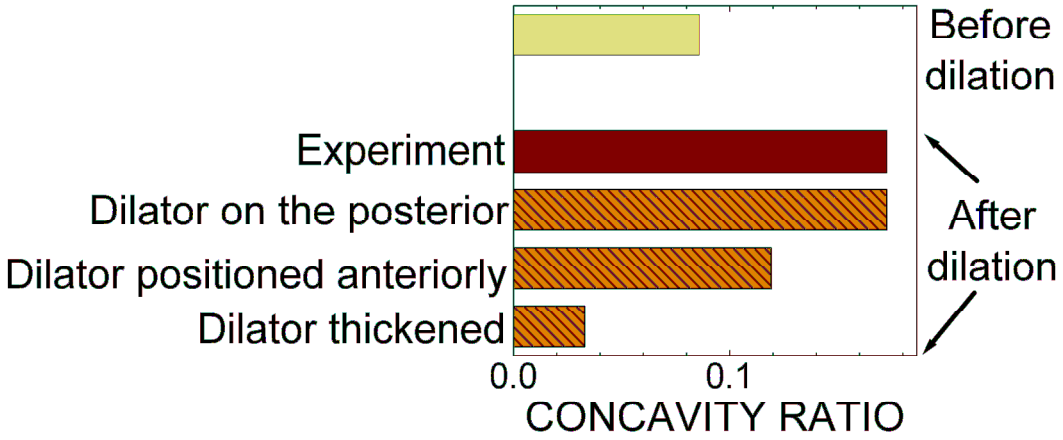

Figure 6.10 Iris concavity ratio before and after dilation in a typical experiment and three models based on the geometry of the experiment (shown in Figure 6.9). In the realistic model, the iris concavity was similar to that of the experiment. Anteriorly positioning or thickening of the dilator muscle in the artificial models led to a predicted concavity inconsistent with the experimental data.

Figure 6.9 shows the iris deformation following dilation in a typical *in vitro* experiment compared with the three *in silico* scenarios created based on the non-deformed geometry of the experimental case. Both in the experiment (Figure 6.9a) and the realistic model, in which the dilator muscle is positioned on the posterior side of the iris (Figure 6.9b), the iris concavity increased and the iris chord length decreased. The artificial models, however, were not able to predict the experimental results correctly. Positioning the dilator anteriorly on the iris muscle led to a smaller increase in the iris concavity following dilation (Figure 6.9c). Simulating the whole thickness of the iris as the active muscle led to a decrease in the iris concavity. Based on the simulation results (Figure 6.10), the realistic model was the only one that predicted the iris concavity following dilation consistent with the experimental results.

6.5. Discussion

The most important conclusion of this study was that the posterior location of the dilator can cause anterior bowing of the iris during dilation even in the absence of aqueous humor flow. We suggest that in patients with peripheral laser iridotomy, for whom the aqueous humor pressure is equalized between the anterior and posterior chambers, the location of the dilator muscle on the iris causes anterior bowing of the iris following dilation.

In regards to the quantitative methods of iris concavity measurements, our *in vitro* experimental results along with clinical data showed that iris concavity ratio was a better measurement of the iris shape change following dilation. In addition, iris concavity ratio, due to its scale-independence, is a more convenient way of comparing data measured in different imaging modalities (e.g. OCT vs. UBM) and does not require the pixel-to-distance ratio.

In our experimental study, we isolated the irides and pinned them in Petri dishes. In choosing such methodology, our intention was to create an equal pressure on the anterior and posterior surfaces of the iris in the bath and eliminate the effect of aqueous humor pressure difference (present *in vivo*). Pinning the iris at two opposite sites is neither an axisymmetric nor a physiologically realistic boundary condition. To create an axisymmetric boundary, we conducted experiments using non-pinned floating irides which led to rigid body movement of the irides and failure of imaging system. Consequently, we had to pin the irides to eliminate their rigid body movements. Our

axisymmetric computational model, however, showed that in both cases of free floating iris and fixed root iris, following dilation, iris bowed anteriorly.

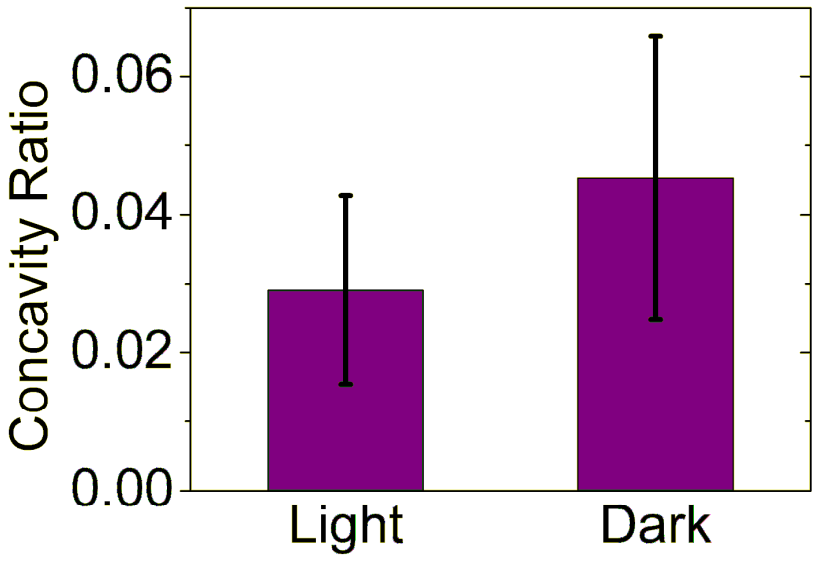

Figure 6.11 Iris concavity of patients with peripheral laser iridotomy in the light and dark (bars are 95% confidence interval, n = 11).

6.6.Appendix- *In Vivo* Experiments

(The *in vivo* experimental studies were performed by our collaborators T.S. Prata and S. Dorairaj at New York Eye and Ear Infirmary and were not part of the work done at the University of Minnesota. This work is presented here only for its relevance to the Chapter)

6.6.1. Methodology

Patients diagnosed with anatomically narrow angles were imaged with Slit Lamp Optical Coherence Tomography (SLOCT) in light and dark conditions. All included patients had undergone laser iridotomy. SLOCT has an optical axial image resolution <25µm and lateral resolution of 20–100 µm (Heidelberg Engineering, GmbH, Dossenheim, Germany). Initially, a total of 5 high-quality cross-sectional images were taken from each patient in dark conditions in the sitting posture. Subsequently, images were acquired under standardized lighting conditions (300 lux), using a 5 x 1mm light beam set at the maximum intensity of the device. Patients were instructed to blink normally and to fixate with the non-imaged eye on a target 1 meter from the device to reduce accommodation. All images were taken horizontally through the center of the pupil to avoid interference from the lid margins, and iris crypts were avoided whenever possible. Quality control parameters were defined as a well-centered image, clearly defined scleral spur, and absence of artifacts. Patients diagnosed with exfoliation syndrome, uveitis, pigmentary glaucoma, and with previous intraocular surgery were excluded. Patients who were on a systemic alpha 1-adrenergic receptor antagonists (such as Flomax) or on topical medications that are known to alter the iris configuration

were not included. Whenever both eyes were eligible, one randomly selected eye was included in the analysis.

Images were subsequently analyzed using the ImageJ [186]. Chord length and iris concavity were calculated as described previously, as was the concavity ration as described in section 6.3.3. Results were compared using a two-sided paired t-test with equal variance.

6.6.2. Results

All of the parameter measured changed following dilation. In particular, pupil diameter was increased from 141.38 ± 10.7 pixels in light (mean ± 95 % CI, n = 11) to 237.2 ± 24.0 pixel in dark ($p < 0.001$). Iris chord length decreased from 245.6 ± 16.3 pixels in light (mean ± 95 % CI, n = 11) to 194.9 ± 12.7 pixel in dark ($p < 0.001$), and iris concavity changed from 6.8 ± 3.5 pixels in light (mean ± 95 % CI, n = 11) to 8.5 ± 4.0 pixel in dark ($p = 0.19$). As shown in Figure 6.11, iris concavity ratio was increased from 0.029 ± 0.013 in light (mean ± 95 % CI, n = 11) to 0.045 ± 0.020 in dark ($p = 0.032$).

Chapter 7: Conclusions and Future Work

7.1.Conclusion

This thesis presents computational studies of the eye at three different levels: ocular globe, anterior segment, and the iris along with the experimental studies on the detailed structure of the iris. Our main focus in these studies was the mechanics of the iris in relation to the physiology and pathophysiology of the eye. The iris shape and configuration play key roles in open angle glaucoma and angle-closure glaucoma. In this work, we showed that the iris configuration could be affected by deformation of the ocular globe, hydrodynamics of the aqueous humor, and activity of the iris muscles.

In the study of whole ocular globe deformation, we found that the limbus, due to its mechanical anisotropy, plays an important role in the biomechanics of the eye. Although we used a simple isotropic linear elastic model for the cornea, sclera, and iris and an anisotropic linear elastic model for the limbus, we were able to predict the results of numerous clinical and experimental observations. Our simulation showed that deformation of the ocular globe due to corneoscleral indentation may lead to changes in the anterior chamber angle and iris root rotation.

Our anterior segment fluid-structure interaction studies showed that a short-term phenomenon such as pushing an indenter against the corneal surface and removing the indenter in a few milliseconds may lead to a much longer change in the iris

contour. Our model showed that due the onset of reverse pupillary block, the aqueous-humor-iris system reached its pre-indentation steady-state long after removal of the indenter. We subsequently showed that the long recovery (~ min) from iris root rotation combined with frequent changes (every 2-4 seconds) in the in the iris root due blinking, might explain why the iris drifts forward when blinking is prevented. In particular, we showed that with each blink, the iris was positioned more posteriorly and since the time for the recovery was longer than the blinking frequency, the iris never fully recovered. We suggest that prevention of blinking allows the iris to completely recover and drifts forward.

While we modeled the iris as a passive rubber-like material in both whole-globe and anterior segment models, our study of pupil dilation showed that the constituent smooth muscles of the iris were important in its mechanical deformation. In particular, our combined experimental and computational studies showed that, even in the absence of the aqueous humor pressure, the iris would bow anteriorly following dilation due to the position of the thin layer of active dilator muscle on the posterior iris.

While not directly concerned with iris biomechanics, we were also able to employ our ocular globe model in predicting IOP increases in presence of intraocular gas bubbles following an altitude increase. Based on our model outcomes, the adaptive change of the aqueous humor volume helped mitigate the potential fluctuation in IOP of an eye partially filled with gas when changing altitude. We showed that certain medications could amplify this effect by increasing the aqueous humor outflow facility

or decreasing the aqueous humor inflow rate. Our model predicted that in both cases, the maximum IOP after ascending to high altitude would decrease. Therefore, they may be beneficial by eliminating patients discomfort and minimizing future glaucoma-related risks. The major potential disadvantage is that after rapid return to low altitude, the eyes may become hypotonic.

7.2.Future Work

As discussed in Chapter 6, detailed structure of the iris is important in physiology and pathophysiology of the eye. Whitcomb *et al.* [37] have experimentally shown that the mechanical properties of the iris depend on the activation of different iris constituting muscles. In addition, in our recent studies (discussed in Appendix A and Ref. [182]) we showed that local mechanical properties of the iris are different on the anterior and posterior surfaces, indicating a mechanical difference among the iris constituting tissues. Finally, recent experimental studies [35,36] have shown that the iris volume changes following dilation proving that the iris is, in fact, not completely incompressible.

In our current models, we treated the iris as a rubber-like incompressible (or nearly incompressible) material. Modifying the mechanical models of the iris using more realistic parameters of iris tissues would be beneficial to better understand the pathophysiology of the eye. Quigley *et al*. [35], for example, have showed that changes in the iris volume due to dilation could serve as an identifying angle-closure glaucoma risk factor. Our modeling system of the anterior segment can be modified by employing

more complex models of the iris, accounting for the incompressibility of the tissue. Such models can be used to study the mechanism by which the iris mechanical properties would be related to glaucoma risk factors.

Bibliography

1. Quigley HA, Broman AT. The number of people with glaucoma worldwide in 2010 and 2020. Br J Ophthalmol 2006; 90:262-267.

2. Epstein DL, Allingham RR, Schuman JS. In: Chandler and Grant's Glaucoma. Baltimore, MD: Williams & Wilkins, 1997:3.

3. Pepose JS, Ubels JL. The cornea. In: Adler's physiology of the eye. St. Louis: Mosby-Year Book, 1992.

4. Goldman JN, Benedek GB. The relationship between morphology and transparency in the nonswelling corneal stroma of the shark. Invest Ophthalmol 1967; 6:574-600.

5. Maurice DM. The structure and transparency of the cornea. J Physiol 1957; 136:263-286.

6. Kaye GI. Stereologic measurement of cell volume fraction of rabbit corneal stroma. Arch Ophthalmol 1969; 82:792-794.

7. Birk DE, Fitch JM, Babiarz JP, Linsenmayer TF. Collagen type I and type V are present in the same fibril in the avian corneal stroma. J Cell Biol 1988; 106:999-1008.

8. Meek KM, Fullwood NJ. Corneal and scleral collagens--a microscopist's perspective. Micron 2001; 32:261-272.

9. Bryant MR, Szerenyi K, Schmotzer H, McDonnell PJ. Corneal tensile strength in fully healed radial keratotomy wounds. Invest Ophthalmol Vis Sci 1994; 35:3022-3031.

10. Hjortdal JO. Regional elastic performance of the human cornea. J Biomech 1996; 29:931-942.

11. Nyquist GW. Rheology of the cornea: experimental techniques and results. Exp Eye Res 1968; 7:183-188.

12. Nguyen TD, Jones RE, Boyce BL. A nonlinear anisotropic viscoelastic model for the tensile behavior of the corneal stroma. J Biomech Eng 2008; 130:041020.

13. Boyce BL, Jones RE, Nguyen TD, Grazier JM. Stress-controlled viscoelastic tensile response of bovine cornea. J Biomech 2007; 40:2367-2376.

14. Woo SL, Kobayashi AS, Schlegel WA, Lawrence C. Nonlinear material properties of intact cornea and sclera. Exp Eye Res 1972; 14:29-39.

15. Hoeltzel DA, Altman P, Buzard K, Choe K. Strip extensiometry for comparison of the mechanical response of bovine, rabbit, and human corneas. J Biomech Eng 1992; 114:202-215.

16. Shin TJ, Vito RP, Johnson LW, McCarey BE. The distribution of strain in the human cornea. J Biomech 1997; 30:497-503.

17. Jonas JB, Holbach L. Central corneal thickness and thickness of the lamina cribrosa in human eyes. Invest Ophthalmol Vis Sci 2005; 46:1275-1279.

18. Jonas JB, Berenshtein E, Holbach L. Lamina cribrosa thickness and spatial relationships between intraocular space and cerebrospinal fluid space in highly myopic eyes. Invest Ophthalmol Vis Sci 2004; 45:2660-2665.

19. Jonas JB, Berenshtein E, Holbach L. Anatomic relationship between lamina cribrosa, intraocular space, and cerebrospinal fluid space. Invest Ophthalmol Vis Sci 2003; 44:5189-5195.

20. Olsen TW, Aaberg SY, Geroski DH, Edelhauser HF. Human sclera: Thickness and surface area. American Journal of Ophthalmology 1998; 125:237-241.

21. Downs JC, Ensor ME, Bellezza AJ et al. Posterior scleral thickness in perfusion-fixed normal and early-glaucoma monkey eyes. Invest Ophthalmol Vis Sci 2001; 42:3202-3208.

22. Ethier CR, Johnson M, Ruberti J. Ocular biomechanics and biotransport. Annu Rev Biomed Eng 2004; 6:249-273.

23. Downs JC, Suh JK, Thomas KA et al. Viscoelastic characterization of peripapillary sclera: material properties by quadrant in rabbit and monkey eyes. J Biomech Eng 2003; 125:124-131.

24. Battaglioli JL, Kamm RD. Measurements of the compressive properties of scleral tissue. Invest Ophthalmol Vis Sci 1984; 25:59-65.

25. Kobayashi AS, Woo SL, Lawrence C, Schlegel WA. Analysis of the corneo-scleral shell by the method of direct stiffness. J Biomech 1971; 4:323-330.

26. Sigal IA, Ethier CR. Biomechanics of the optic nerve head. Exp Eye Res 2009; 88:799-807.

27. Aghamohammadzadeh H, Newton RH, Meek KM. X-ray scattering used to map the preferred collagen orientation in the human cornea and limbus. Structure 2004; 12:249-256.

28. Boyce BL, Grazier JM, Jones RE, Nguyen TD. Full-field deformation of bovine cornea under constrained inflation conditions. Biomaterials 2008; 29:3896-3904.

29. Asejczyk-Widlicka M, Srodka DW, Kasprzak H, Pierscionek BK. Modelling the elastic properties of the anterior eye and their contribution to maintenance of image quality: the role of the limbus. Eye 2007; 21:1087-1094.

30. Pierscionek BK, Asejczyk-Widlicka M, Schachar RA. The effect of changing intraocular pressure on the corneal and scleral curvatures in the fresh porcine eye. Br J Ophthalmol 2007; 91:801-803.

31. Pavlin C, Harasiewicz K, Foster F. Ultrasound biomicroscopy analysis of the anterior segment in normal and glaucomatous eyes. Am J Ophthalmol 1992; 113:381-389.

32. Thompson HS. The pupil. In: Adler's physiology of the eye. St. Louis: Mosby-Year Book, 1992;412-441.

33. Heys J, Barocas VH. Mechanical characterization of the bovine iris. J Biomech 1999; 32:999-1003.

34. Lei Y, Zhang K, Chen C et al. Experimental research on the mechanical properties of porcine iris. Clin Biomech (Bristol, Avon) 2008; 23 Suppl 1:S83-7.

35. Quigley HA, Silver DM, Friedman DS et al. Iris cross-sectional area decreases with pupil dilation and its dynamic behavior is a risk factor in angle closure. J Glaucoma 2009; 18:173-179.

36. Aptel F, Denis P. Optical coherence tomography quantitative analysis of iris volume changes after pharmacologic mydriasis. Ophthalmology 2010; 117:3-10.

37. Whitcomb JE, Barnett VA, Olsen TW, Barocas VH. Ex vivo porcine iris stiffening due to drug stimulation. Exp Eye Res 2009; 89:456-461.

38. Yamaji K, Yoshitomi T, Usui S, Ohnishi Y. Mechanical properties of the rabbit iris smooth muscles. Vision Res 2003; 43:479-487.

39. Patterson CA, Delamere NA. The lens. In: Adler's physiology of the eye. St. Louis: Mosby-Year Book, 1992;348-390.

40. Weekers R, Delmarcelle Y, Collignon J, Luyckx J. Optical measurement of the depth of the anterior chamber. Clinical applications. Doc Ophthalmol 1973; 34:413-434.

41. Fontana ST, Brubaker RF. Volume and depth of the anterior chamber in the normal aging human eye. Arch Ophthalmol 1980; 98:1803-1808.

42. Koretz JF, Handelman GH. Model of the accommodative mechanism in the human eye. Vision Res 1982; 22:917-927.

43. Crawford KS, Kaufman PL, Bito LZ. The role of the iris in accommodation of rhesus monkeys. Invest Ophthalmol Vis Sci 1990; 31:2185-2190.

44. Rohen J. Scanning electron microscopic studies of the zonular apparatus in human and monkey eyes. Invest Ophthalmol Vis Sci 1979; 18:133-144.

45. Krag S, Andreassen TT. Mechanical Properties of the Human Posterior Lens Capsule. Invest Ophthalmol Vis Sci 2003; 44:691-696.

46. Wollensak G, Sporl E, Pham DT. Biomechanical changes in the anterior lens capsule after trypan blue staining. J Cataract Refract Surg 2004; 30:1526-1530.

47. Heistand MR, Pedrigi RM, Delange SL, Dziezyc J, Humphrey JD. Multiaxial mechanical behavior of the porcine anterior lens capsule. Biomech Model Mechanobiol 2005; 4:168-177.

48. Fisher RF. Elastic constants of the human lens capsule. J Physiol 1969; 201:1-19.

49. Danielsen CC. Tensile mechanical and creep properties of Descemet's membrane and lens capsule. Exp Eye Res 2004; 79:343-350.

50. Caprioli J. The ciliary epithelia and aqueous humor. In: Hart W ed. Adler's Physiology of the Eye . St. Louis: Mosby, 1992.

51. Forrester JV, Dick AD, McMenamin PG, Roberts F. Anatomy of the eye and orbit. In: The eye: basic sciences in practice: WB Saunders Co, 2008;1-107.

52. Scott JA. A finite element model of heat transport in the human eye. Phys Med Biol 1988; 33:227-241.

53. Beswick JA, McCulloch C. Effect of hyaluronidase on the viscosity of the aqueous humour. Br J Ophthalmol 1956; 40:545-548.

54. Carel RS, Korczyn AD, Rock M, Goya I. Association between ocular pressure and certain health parameters. Ophthalmology 1984; 91:311-314.

55. Hogan MJ, Alvarado JA, Weddell JE. Histology of the Human Eye: An Atlas and Textbook: WB Saunders Company, 1971.

56. Sit AJ, Nau CB, McLaren JW, Johnson DH, Hodge D. Circadian variation of aqueous dynamics in young healthy adults. Invest Ophthalmol Vis Sci 2008; 49:1473-1479.

57. Epstein DL, Allingham RR, Schuman JS. Segmental Nature of Outflow: Implication for Angle Closure Glaucoma. In: Chandler and Grant's Glaucoma. Baltimore, MD: Williams & Wilkins, 1997;20-21.

58. Davson H. A comparative study of the aqueous humour and cerebrospinal fluid in the rabbit. J Physiol 1955; 129:111-133.

59. Friedenwald JS. The formation of the intraocular fluid. Am J Ophthalmol 1949; 32 Pt. 2:9-27.

60. Green K, Pederson JE. Contribution of secretion and filtration to aqueous humor formation. Am J Physiol 1972; 222:1218-1226.

61. Green K, Pederson JE. Aqueous humor formation. Exp Eye Res 1973; 16:273-286.

62. Weinbaum S, Langham ME, Goldgraben JR, Green K. The role of secretion and pressure-dependent flow in aqueous humor formation. Exp Eye Res 1972; 13:266-277.

63. Bonting SL, Becker B. Studies on Sodium-Potassium Activated Adenosinetriphosphatase. Xiv. Inhibition of Enzyme Activity and Aqueous Humor Flow in the Rabbit Eye After Intravitreal Injection of Ouabain. Invest Ophthalmol 1964; 3:523-533.

64. Cole DF. Secretion of the aqueous humour. Exp Eye Res 1977; 25 Suppl:161-176.

65. Garg LC, Oppelt WW. The effect of ouabain and acetazolamide on transport of sodium and chloride from plasma to aqueous humor. J Pharmacol Exp Ther 1970; 175:237-247.

66. Bill A. The role of ciliary blood flow and ultrafiltration in aqueous humor formation. Exp Eye Res 1973; 16:287-298.

67. Bill A. Blood circulation and fluid dynamics in the eye. Physiol Rev 1975; 55:383-417.

68. Forrester JV, Dick AD, McMenamin PG, Roberts F. Secretion of aqueous humor. In: The eye: basic sciences in practice: WB Saunders Co, 2008;224.

69. Brown JD, Brubaker RF. A study of the relation between intraocular pressure and aqueous humor flow in the pigment dispersion syndrome. Ophthalmology 1989; 96:1468-1470.

70. Beneyto Martin P, Fernandez-Vila PC, Perez TM. Determination of the pseudofacility by fluorophotometry in the human eye. Int Ophthalmol 1995; 19:219-223.

71. Kaskel D, Arens E. Determination of pseudofacility in man. Graefe's Archive for Clinical and Experimental Ophthalmology 1979; 210:187-192.

72. Hart WM. Intraocular Pressure. In: Adler's physiology of the eye. St. Louis: Mosby-Year Book, 1992;248-267.

73. Toris CB, Yablonski ME, Wang YL, Camras CB. Aqueous humor dynamics in the aging human eye. Am J Ophthalmol 1999; 127:407-412.

74. Sultan M, Blondeau P. Episcleral venous pressure in younger and older subjects in the sitting and supine positions. J Glaucoma 2003; 12:370-373.

75. Bill A. Conventional and uveo-scleral drainage of aqueous humour in the cynomolgus monkey (Macaca irus) at normal and high intraocular pressures. Exp Eye Res 1966; 5:45-54.

76. Bill A. Further Studies on the Influence of the Intraocular Pressure on Aqueous Humor Dynamics in Cynomolgus Monkeys. Invest Ophthalmol Vis Sci 1967; 6:364-372.

77. Sebag J. The vitreous. In: Hart W ed. Adler's physiology of the eye. St. Louis: Mosby, 1992;268-347.

78. Brubaker RF, Riley FC,Jr. Vitreous body volume reduction in the rabbit. Effect of surgical opening of the anterior chamber in the normal eye. Arch Ophthalmol 1972; 87:438-442.

79. Epstein DL, Hashimoto JM, Anderson PJ, Grant WM. Experimental perfusions through the anterior and vitreous chambers with possible relationships to malignant glaucoma. Am J Ophthalmol 1979; 88:1078-1086.

80. Araie M, Sugiura Y, Sakurai M, Oshika T. Effect of systemic acetazolamide on the fluid movement across the aqueous-vitreous interface. Exp Eye Res 1991; 53:285-293.

81. Quigley HA. Glaucoma: macrocosm to microcosm the Friedenwald lecture. Invest Ophthalmol Vis Sci 2005; 46:2662-2670.

82. Thylefors B, Negrel AD. The global impact of glaucoma. Bull World Health Organ 1994; 72:323-326.

83. Leske MC, Connell AMS, Wu SY, Hyman LG, Schachat AP. Risk factors for open-angle glaucoma: the Barbados Eye Study. Arch Ophthalmol 1995; 113:918.

84. Munoz B, West SK, Rubin GS et al. Causes of blindness and visual impairment in a population of older Americans: The Salisbury Eye Evaluation Study. Arch Ophthalmol 2000; 118:819-825.

85. Bengtsson B, Heijl A. A long-term prospective study of risk factors for glaucomatous visual field loss in patients with ocular hypertension. J Glaucoma 2005; 14:135-138.

86. Heijl A, Leske MC, Bengtsson B et al. Reduction of intraocular pressure and glaucoma progression: results from the Early Manifest Glaucoma Trial. Arch Ophthalmol 2002; 120:1268-1279.

87. Leske MC, Heijl A, Hussein M et al. Factors for glaucoma progression and the effect of treatment: the early manifest glaucoma trial. Arch Ophthalmol 2003; 121:48-56.

88. Weinreb RN, Khaw PT. Primary open-angle glaucoma. Lancet 2004; 363:1711-1720.

89. Anderson DR, Drance SM, Schulzer M, Collaborative Normal-Tension Glaucoma Study Group. Natural history of normal-tension glaucoma. Ophthalmology 2001; 108:247-253.

90. The Advanced Glaucoma Intervention Study (AGIS): 7. The relationship between control of intraocular pressure and visual field deterioration.The AGIS Investigators. Am J Ophthalmol 2000; 130:429-440.

91. Karickhoff JR. Reverse pupillary block in pigmentary glaucoma: follow up and new developments. Ophthalmic Surg 1993; 24:562-563.

92. Farrar SM, Shields MB. Current concepts in pigmentary glaucoma. Surv Ophthalmol 1993; 37:233-252.

93. Sugar HS. Pigmentary glaucoma. A 25-year review. Am J Ophthalmol 1966; 62:499-507.

94. Murphy CG, Johnson M, Alvarado JA. Juxtacanalicular tissue in pigmentary and primary open angle glaucoma. The hydrodynamic role of pigment and other constituents. Arch Ophthalmol 1992; 110:1779-1785.

95. Tello C, Tran HV, Liebmann J, Ritch R. Angle closure: classification, concepts, and the role of ultrasound biomicroscopy in diagnosis and treatment. Semin Ophthalmol 2002; 17:69-78.

96. Congdon NG, Friedman DS. Angle-closure glaucoma: impact, etiology, diagnosis, and treatment. Curr Opin Ophthalmol 2003; 14:70-73.

97. Quigley HA, Friedman DS, Congdon NG. Possible mechanisms of primary angle-closure and malignant glaucoma. J Glaucoma 2003; 12:167-180.

98. Mapstone R. Mechanics of pupil block. Br J Ophthalmol 1968; 52:19-25.

99. Huang EC, Barocas VH. Active iris mechanics and pupillary block: Steady-state analysis and comparison with anatomical risk factors. Ann Biomed Eng 2004; 32:1276-1285.

100. Dorairaj S, Oliveira C, Fose AK et al. Accommodation-induced changes in iris curvature. Exp Eye Res 2008; 86:220-225.

101. Heys JJ, Barocas VH. Modeling of passive iris deformation during blinking and accommodation 2001; 50:571-572.

102. Liebmann JM, Ritch R. Laser iridotomy. Ophthalmic Surg Lasers 1996; 27:209-227.

103. Caronia RM, Liebmann JM, Stegman Z, Sokol J, Ritch R. Increase in iris-lens contact after laser iridotomy for pupillary block angle closure. Am J Ophthalmol 1996; 122:53-57.

104. Liebmann JM, Ritch R. Laser surgery for angle closure glaucoma. Semin Ophthalmol 2002; 17:84-91.

105. Breingan PJ, Esaki K, Ishikawa H et al. Iridolenticular contact decreases following laser iridotomy for pigment dispersion syndrome. Arch Ophthalmol 1999; 117:325-328.

106. Heys J, Barocas V, May M, Taravella M. Modeling passive iris deformation with application to pigmentary glaucoma. Ann Biomed Eng 2000; 28:-44.

107. Huang EC, Barocas VH. Accommodative microfluctuations and iris contour. J Vis 2006; 6:653-660.

108. Pandolfi A, Holzapfel GA. Three-dimensional modeling and computational analysis of the human cornea considering distributed collagen fibril orientations. J Biomech Eng 2008; 130:061006.

109. Pinsky PM, van der Heide D, Chernyak D. Computational modeling of mechanical anisotropy in the cornea and sclera. J Cataract Refract Surg 2005; 31:136-145.

110. Margulies S, Coats B, Christian C, Forbes B, Duhaime AC. What can we learn from computational model studies of the eye?. J AAPOS 2009; 13:332.

111. Sigal IA, Flanagan JG, Ethier CR. Factors Influencing Optic Nerve Head Biomechanics. Invest Ophthalmol Vis Sci 2005; 46:4189-4199.

112. Srodka W, Iskander DR. Optically inspired biomechanical model of the human eyeball. J Biomed Opt 2008; 13:044034.

113. Srodka W, Pierscionek BK. Effect of material properties of the eyeball coat on optical image stability. J Biomed Opt 2008; 13:054013.

114. Friedland AB. A hydrodynamic model of aqueous flow in the posterior chamber of the eye. Bulletin of Mathematical Biology 1978; 40:223-235.

115. Tiedeman JS. A physical analysis of the factors that determine the contour of the iris. Am J Ophthalmol 1991; 111:338-343.

116. Silver DM, Quigley HA. Aqueous flow through the iris-lens channel: estimates of differential pressure between the anterior and posterior chambers. J Glaucoma 2004; 13:100-107.

117. Kumar S, Acharya S, Beuerman R, Palkama A. Numerical solution of ocular fluid dynamics in a rabbit eye: parametric effects. Ann Biomed Eng 2006; 34:530-544.

118. Fitt AD, Gonzalez G. Fluid mechanics of the human eye: aqueous humour flow in the anterior chamber. Bull Math Biol 2006; 68:53-71.

119. Kapnisis K, Doormaal MV, Ross Ethier C. Modeling aqueous humor collection from the human eye. J Biomech 2009; 42:2454-2457.

120. Heys JJ, Barocas VH, Taravella MJ. Modeling passive mechanical interaction between aqueous humor and iris. J Biomech Eng 2001; 123:540-547.

121. Heys JJ, Barocas VH. Computational evaluation of the role of accommodation in pigmentary glaucoma. Invest Ophthalmol Vis Sci 2002; 43:700-708.

122. Heys JJ, Taravella MJ, Barocas VH. Biomechanics of the aqueous humor and iris in pigmentary glaucoma. American Society of Mechanical Engineers, Bioengineering Division (Publication) BED 1999; 42:201-202.

123. Amini R, Barocas VH. Anterior chamber angle opening during corneoscleral indentation: the mechanism of whole eye globe deformation and the importance of the limbus. Invest Ophthalmol Vis Sci 2009; 50:5288-5294.

124. Ritch R, Shields MB, Krupin T. Gonioscopy. In: The Glaucomas. St. Louis, MI: Mosby-Year Book, Inc., 1996;462-464.

125. Bruno CA, Alward WL. Gonioscopy in primary angle closure glaucoma. Semin Ophthalmol 2002; 17:59-68.

126. Forbes M. Gonioscopy with corneal indentation. A method for distinguishing between appositional closure and synechial closure. Arch Ophthalmol 1966; 76:488-492.

127. Ishikawa H, Inazumi K, Liebmann JM, Ritch R. Inadvertent corneal indentation can cause artifactitious widening of the iridocorneal angle on ultrasound biomicroscopy. Ophthalmic Surg Lasers 2000; 31:342-345.

128. Matsunaga K, Ito K, Esaki K et al. Evaluation of eyes with relative pupillary block by indentation ultrasound biomicroscopy gonioscopy. American Journal of Ophthalmology 2004/3; 137:552-554.

129. Masselos K, Bank A, Francis IC, Stapleton F. Corneal indentation in the early management of acute angle closure. Ophthalmology 2009; 116:25-29.

130. Anderson DR. Corneal indentation to relieve acute angle-closure glaucoma. Am J Ophthalmol 1979; 88:1091-1093.

131. Teichmann KD. Corneal indentation to relieve glaucoma. Am J Ophthalmol 1980; 90:434-435.

132. Takanashi T, Masuda H, Tanito M et al. Scleral indentation optimizes visualization of anterior chamber angle during goniosynechialysis. J Glaucoma 2005; 14:293-298.

133. Liebmann JM, Tello C, Chew SJ, Cohen H, Ritch R. Prevention of blinking alters iris configuration in pigment dispersion syndrome and in normal eyes. Ophthalmology 1995; 102:446-455.

134. Campbell DG, Vela A. Modern goniosynechialysis for the treatment of synechial angle-closure glaucoma. Ophthalmology 1984; 91:1052-1060.

135. Kaufman PL, Alm A. Adler's physiology of the eye. In: : Mosby, 2003;18.

136. Percicot CL, Schnell CR, Debon C, Hariton C. Continuous intraocular pressure measurement by telemetry in alpha-chymotrypsin-induced glaucoma model in the rabbit: effects of timolol, dorzolamide, and epinephrine. J Pharmacol Toxicol Methods 1996; 36:223-228.

137. Collins CC. Miniature passive pressure transensor for implanting in the eye. IEEE Trans Biomed Eng 1967; 14:74-83.

138. Bellezza AJ, Hart RT, Burgoyne CF. The optic nerve head as a biomechanical structure: initial finite element modeling. Invest Ophthalmol Vis Sci 2000; 41:2991-3000.

139. Sigal IA, Flanagan JG, Tertinegg I, Ethier CR. Finite element modeling of optic nerve head biomechanics. Invest Ophthalmol Vis Sci 2004; 45:4378-4387.

140. Burgoyne CF, Downs JC, Bellezza AJ, Suh JK, Hart RT. The optic nerve head as a biomechanical structure: a new paradigm for understanding the role of IOP-related stress and strain in the pathophysiology of glaucomatous optic nerve head damage. Prog Retin Eye Res 2005; 24:39-73.

141. Sander EA, Downs JC, Hart RT, Burgoyne CF, Nauman EA. A cellular solid model of the lamina cribrosa: mechanical dependence on morphology. J Biomech Eng 2006; 128:879-889.

142. Daxer A, Fratzl P. Collagen fibril orientation in the human corneal stroma and its implication in keratoconus. Invest Ophthalmol Vis Sci 1997; 38:121-129.

143. Asejczyk-Widlicka M, Pierscionek BK. The elasticity and rigidity of the outer coats of the eye. Br Med J 2008; 92:1415.

144. Schoemaker I, Hoefnagel PPW, Mastenbroek TJ et al. Elasticity, viscosity, and deformation of orbital fat. Invest Ophthalmol Vis Sci 2006; 47:4819-4826.

145. Hashin Z, Rosen BW. The elastic moduli of fiber-reinforced materials. Journal of Applied Mechanics 1964; 31:223-232.

146. McMonnies CW. Intraocular pressure spikes in keratectasia, axial myopia, and glaucoma. Optom Vis Sci 2008; 85:1018-1026.

147. Coleman DJ, Trokel S. Direct-recorded intraocular pressure variations in a human subject. Arch Ophthalmol 1969; 82:637-640.

148. Buzard KA. Introduction to biomechanics of the cornea. Refract Corneal Surg 1992; 8:127-138.

149. Olsen TW, Sanderson S, Feng X, Hubbard WC. Porcine sclera: thickness and surface area. Invest Ophthalmol Vis Sci 2002; 43:2529-2532.

150. Hogan MJ, Alvarado JA, Weddell JE. The Limbus. In: Histology of the human eye. Philadelphia, PA: WB Saunders Company, 1971;112-180.

151. Marchini G, Pagliarusco A, Toscano A et al. Ultrasound biomicroscopic and conventional ultrasonographic study of ocular dimensions in primary angle-closure glaucoma. Ophthalmology 1998; 105:2091-2098.

152. Lee DA, Brubaker RF, Ilstrup DM. Anterior chamber dimensions in patients with narrow angles and angle-closure glaucoma. Arch Ophthalmol 1984; 102:46-50.

153. Yamaguchi T, Negishi K, Yuki K et al. Alterations in the anterior chamber angle after implantation of iris-fixated phakic intraocular lenses. J Cataract Refract Surg 2008; 34:1300-1305.

154. Yi JH, Hong S, Seong GJ et al. Anterior chamber measurements by pentacam and AS-OCT in eyes with normal open angles. Korean J Ophthalmol 2008; 22:242-245.

155. Tham CCY, Lai JSM, Lam DSC. Changes in AC angle width and depth after IOL implantation in eyes with glaucoma. Ophthalmology 2001; 108:428-429.

156. Alm A. Ocular Circulation. In: Hart W ed. Adler's Physiology of the Eye . St. Louis: Mosby, 1992;198-227.

157. Ytteborg J. The role of intraocular blood volume in rigidity measurements on human eyes. Acta Ophthalmol (Copenh) 1960; 38:410-436.

158. Lane JI, Watson RE,Jr, Witte RJ, McCannel CA. Retinal detachment: imaging of surgical treatments and complications. Radiographics 2003; 23:983-994.

159. Ai E, Gardner TW. Current patterns of intraocular gas use in North America. Arch Ophthalmol 1993; 111:331-332.

160. Chan CK, Lin SG, Nuthi AS, Salib DM. Pneumatic retinopexy for the repair of retinal detachments: a comprehensive review (1986-2007). Surv Ophthalmol 2008; 53:443-478.

161. Cekic O, Ohji M. Intraocular gas tamponades. Semin Ophthalmol 2000; 15:3-14.

162. Thompson JT. Kinetics of intraocular gases. Disappearance of air, sulfur hexafluoride, and perfluoropropane after pars plana vitrectomy. Arch Ophthalmol 1989; 107:687-691.

163. Kokame GT, Ing MR. Intraocular gas and low-altitude air flight. Retina 1994; 14:356-358.

164. Fang IM, Huang JS. Central retinal artery occlusion caused by expansion of intraocular gas at high altitude. Am J Ophthalmol 2002; 134:603-605.

165. Hart RH, Vote BJ, Borthwick JH, McGeorge AJ, Worsley DR. Loss of vision caused by expansion of intraocular perfluoropropane (C(3)F(8)) gas during nitrous oxide anesthesia. Am J Ophthalmol 2002; 134:761-763.

166. Lincoff H, Weinberger D, Reppucci V, Lincoff A. Air travel with intraocular gas. I. The mechanisms for compensation. Arch Ophthalmol 1989; 107:902-906.

167. Sommer A. Glaucoma risk factors observed in the Baltimore Eye Survey. Curr Opin Ophthalmol 1996; 7:93-98.

168. Mills MD, Devenyi RG, Lam WC et al. An assessment of intraocular pressure rise in patients with gas-filled eyes during simulated air flight. Ophthalmology 2001; 108:40-44.

169. Lincoff H, Weinberger D, Stergiu P. Air travel with intraocular gas. II. Clinical considerations. Arch Ophthalmol 1989; 107:907-910.

170. Atmosphere USS. US Government Printing Office, Washington, DC. Available in hard copy from the National Technical Information Office, Springfield, Virginia (Product Number: ADA-035-6000).The Fortran code can be obtained from Public Domain Aeronautical Software.A DOS executable and turbo pascal source code i(TRUNCATED) 1976.

171. Perlman JI, Delany CM, Sothern RB et al. Relationships between 24h observations in intraocular pressure vs blood pressure, heart rate, nitric oxide and age in the medical chronobiology aging project. Clin Ter 2007; 158:31-47.

172. Liu JH, Bouligny RP, Kripke DF, Weinreb RN. Nocturnal elevation of intraocular pressure is detectable in the sitting position. Invest Ophthalmol Vis Sci 2003; 44:4439-4442.

173. Silver DM, Geyer O. Pressure-volume relation for the living human eye. Curr Eye Res 2000; 20:115-120.

174. Liu J, He X. Corneal stiffness affects IOP elevation during rapid volume change in the eye. Invest Ophthalmol Vis Sci 2009; 50:2224.

175. Kaufman PL. Enhancing trabecular outflow by disrupting the actin cytoskeleton, increasing uveoscleral outflow with prostaglandins, and understanding the pathophysiology of presbyopia interrogating Mother Nature: asking why, asking how, recognizing the signs, following the trail. Exp Eye Res 2007.

176. Sander EA, Downs JC, Hart RT, Burgoyne CF, Nauman EA. A cellular solid model of the lamina cribrosa: mechanical dependence on morphology. J Biomech Eng 2006; 128:879-889.

177. Marchini G, Pagliarusco A, Toscano A et al. Ultrasound biomicroscopic and conventional ultrasonographic study of ocular dimensions in primary angle-closure glaucoma. Ophthalmology 1998; 105:2091-2098.

178. Lowe RF. Anterior lens curvature. Comparisons between normal eyes and those with primary angle-closure glaucoma. Br J Ophthalmol 1972; 56:409-413.

179. Sackinger P, Schunk P, Rao R. A Newton-Raphson Pseudo-Solid Domain Mapping Technique for Free and Moving Boundary Problems: A Finite Element Implementation. Journal of Computational Physics 1996; 125:83-103.

180. Amestoy PR, Duff IS, L'Excellent J-. Multifrontal parallel distributed symmetric and unsymmetric solvers. Computer Methods in Applied Mechanics and Engineering, 2000; 184:501-520.

181. Amini R, Whitcomb JH, Al-Qaisi MK, Akkin T, Barocas VH. The effect of the posterior location of the dilator on the iris concavity 2009.

182. Whitcomb JE, Amini R, Simha N, Barocas VH. Assessment of the Mechanical Properties of the Iris Dilator and Stroma Using Nanoindentation. Invest Ophthalmol Vis Sci 2009; 50:4907.

183. Sun WS, Baker RS, Chuke JC et al. Age-related changes in human blinks. Passive and active changes in eyelid kinematics. Invest Ophthalmol Vis Sci 1997; 38:92-99.

184. Karson CN. Spontaneous eye-blink rates and dopaminergic systems. Brain 1983; 106 (Pt 3):643-653.

185. Karson CN, Berman KF, Donnelly EF et al. Speaking, thinking, and blinking. Psychiatry Res 1981; 5:243-246.

186. Abramoff MD, Magalhaes PJ, Ram SJ. Image processing with ImageJ. Biophoton Int 2004; 11:36-43.

187. Mandell MA, Pavlin CJ, Weisbrod DJ, Simpson ER. Anterior chamber depth in plateau iris syndrome and pupillary block as measured by ultrasound biomicroscopy. Am J Ophthalmol 2003; 136:900-903.

188. Nonaka A, Iwawaki T, Kikuchi M et al. Quantitative evaluation of iris convexity in primary angle closure. Am J Ophthalmol 2007; 143:695-697.

189. Woo EK, Pavlin CJ, Slomovic A, Taback N, Buys YM. Ultrasound biomicroscopic quantitative analysis of light-dark changes associated with pupillary block. Am J Ophthalmol 1999; 127:43-47.

190. Yamamoto Y, Uno T, Shisida K et al. Demonstration of aqueous streaming through a laser iridotomy window against the corneal endothelium. Arch Ophthalmol 2006; 124:387-393.

191. Stubbe R, Sahlgren B. Swept-source optical coherence tomography 2007; 05106529.0.

192. Dunn SM, Constantinides A, Moghe PV. Spline Interpolation. In: Numerical methods in biomedical engineering. London, UK: Elsevier Academic Press, 2006;192-193.

193. Costa KD, Yin FC. Analysis of indentation: implications for measuring mechanical properties with atomic force microscopy. J Biomech Eng 1999; 121:462-471.

194. Ruben GC, Yurchenco PD. High resolution platinum-carbon replication of freeze-dried basement membrane. Microsc Res Tech 1994; 28:13-28.

195. Barnard K, Gathercole LJ. Short and long range order in basement membrane type IV collagen revealed by enzymic and chemical extraction. Int J Biol Macromol 1991; 13:359-365.

196. Kelley PB, Sado Y, Duncan MK. Collagen IV in the developing lens capsule. Matrix Biol 2002; 21:415-423.

197. Fisher RF. The deformation matrix theory of basement membrane: a study of water flow through elastic and rigid filaments in the rat. J Physiol 1988; 406:1-14.

198. Sundaramoorthy M, Meiyappan M, Todd P, Hudson BG. Crystal structure of NC1 domains. Structural basis for type IV collagen assembly in basement membranes. J Biol Chem 2002; 277:31142-31153.

199. Donaldson P, Kistler J, Mathias RT. Molecular solutions to mammalian lens transparency. News Physiol Sci 2001; 16:118-123.

200. Gerometta R, Zamudio AC, Escobar DP, Candia OA. Volume change of the ocular lens during accommodation. Am J Physiol Cell Physiol 2007; 293:C797-804.

201. Pirie A. Difference in swelling and opacity formation between young and old lenses. Nature 1967; 216:503-504.

202. Peczon BD, Peczon JD, Cintron C, Hudson BG. Changes in chemical composition of anterior lens capsules of cataractous human eyes as a function of age. Exp Eye Res 1980; 30:155-165.

203. Bredrup C, Matejas V, Barrow M et al. Ophthalmological aspects of Pierson syndrome. Am J Ophthalmol 2008; 146:602-611.

204. Fisher RF. Changes in the permeability of the lens capsule in senile cataract. Trans Ophthalmol Soc U K 1977; 97:100-103.

205. Colville DJ, Savige J. Alport syndrome. A review of the ocular manifestations. Ophthalmic Genet 1997; 18:161-173.

206. LeBleu VS, Macdonald B, Kalluri R. Structure and function of basement membranes. Exp Biol Med (Maywood) 2007; 232:1121-1129.

207. Miosge N. The ultrastructural composition of basement membranes in vivo. Histol Histopathol 2001; 16:1239-1248.

208. Danysh BP, Duncan MK. The lens capsule. Exp Eye Res 2009; 88:151-164.

209. Kalluri R. Basement membranes: structure, assembly and role in tumour angiogenesis. Nat Rev Cancer 2003; 3:422-433.

210. Krag S, Andreassen TT. Biomechanical measurements of the porcine lens capsule. Exp Eye Res 1996; 62:253-260.

211. Ziebarth NM, Borja D, Arrieta E et al. Role of the lens capsule on the mechanical accommodative response in a lens stretcher. Invest Ophthalmol Vis Sci 2008; 49:4490-4496.

212. David G, Pedrigi RM, Heistand MR, Humphrey JD. Regional multiaxial mechanical properties of the porcine anterior lens capsule. J Biomech Eng 2007; 129:97-104.

213. Mela MJ. Elastic-Mathematical Theory of Cells and Mitochondria in Swelling Process: The Membranous Stresses and Modulus of Elasticity of the Egg Cell of Sea Urchin, Strongylocentrotus purpuratus. Biophys J 1967; 7:95.

214. Mlekoday H. Osmotic water permeability of the human red cell. Dependence on direction of water flow and cell volume. J Gen Physiol 1983; 81:213-220.

215. Vinogradova OI. Mechanical properties of polyelectrolyte multilayer microcapsules. Journal of Physics, Condensed Matter 2004; 16.

216. Cosgrove D. Biophysical Control of Plant Cell Growth. Annual Reviews in Plant Physiology 1986; 37:377-405.

217. Wolfe J, Dowgert MF, Steponkus PL. Mechanical study of the deformation and rupture of the plasma membranes of protoplasts during osmotic expansions. J Membr Biol 1986; 93:63-74.

218. Zimmermann U, Steudle E. The pressure-dependence of the hydraulic conductivity, the membrane resistance and membrane potential during turgor pressure regulation in Valonia utricularis. J Membr Biol 1974; 16:331-352.

219. Philip JR. The Osmotic Cell, Solute Diffusibility, and the Plant Water Economy. Plant Physiol 1958; 33:264-271.

220. Jacob TJ, Duncan G. Osmotic influences on lens membrane characteristics. Exp Eye Res 1980; 31:505-512.

221. Cotlier E, Kwan B, Beaty C. The lens as an osmometer and the effects of medium osmolarity on water transport, 86Rb efflux and 86Rb transport by the lens. Biochim Biophys Acta 1968; 150:705-722.

222. Patterson JW, Fournier DJ. The effect of tonicity on lens volume. Invest Ophthalmol 1976; 15:866-869.

223. Wang H, Gao J, Sun X et al. The effects of GPX-1 knockout on membrane transport and intracellular homeostasis in the lens. J Membr Biol 2009; 227:25-37.

224. Young MA, Tunstall MJ, Kistler J, Donaldson PJ. Blocking chloride channels in the rat lens: localized changes in tissue hydration support the existence of a circulating chloride flux. Invest Ophthalmol Vis Sci 2000; 41:3049-3055.

225. Crank J. The mathematics of diffusion. Oxford, Eng: Clarendon Press, 1975; 414.

226. Fowler AC, Krantz WB. A generalized secondary frost heave model. SIAM J Appl Math 1994; 54:1650-1675.

227. Fedors RF. Osmotic effects in water absorption by polymers. Polymer 1980; 21:207-212.

228. Gere JM, Goodno BJ. Spherical Pressure Vessels. In: Mechanics of Materials. Toronto, Canada: Cengage Learning, 2009;621-626.

229. Kedem O, Katchalsky A. Thermodynamic analysis of the permeability of biological membranes to non-electrolytes. 1958. Biochim Biophys Acta 1989; 1000:413-430.

230. Bartels EM, Elliott GF. The effect of ATP on the Donnan potential and protein fixed charge in bovine lens fibres. JOURNAL OF PHYSIOLOGY-LONDON THEN CAMBRIDGE-1993; 467:279P.

231. Plonsey R, Roger CB. Donnan Equilibrium. In: Bioelectricity A Quantitative Approach. New York: Plenum Press, 1988;44-47.

232. Paterson CA. Distribution and movement of ions in the ocular lens. Doc Ophthalmol 1972; 31:1-28.

233. Lachish U. Osmosis and thermodynamics. American Journal of Physics 2007; 75:997.

234. Shampine LF, Reichelt MW. The matlab ode suite. SIAM journal on scientific computing 1997; 18:1-22.

235. Krag S, Andreassen TT. Mechanical properties of the human lens capsule. Prog Retin Eye Res 2003; 22:749-767.

236. Danysh BP, Czymmek KJ, Olurin PT, Sivak JG, Duncan MK. Contributions of mouse genetic background and age on anterior lens capsule thickness. Anat Rec (Hoboken) 2008; 291:1619-1627.

237. Barraquer RI, Michael R, Abreu R, Lamarca J, Tresserra F. Human lens capsule thickness as a function of age and location along the sagittal lens perimeter. Invest Ophthalmol Vis Sci 2006; 47:2053-2060.

238. Lagarias JC, Reeds JA, Wright MH, Wright PE. Convergence properties of the Nelder-Mead simplex method in low dimensions. SIAM Journal on Optimization 1999; 9:112-147.

239. Ross SM. Peirce's criterion for the elimination of suspect experimental data. Journal of Engineering Technology 2003; 20:38-41.

240. Shapiro HN, Moran J. Universal Gas Constant, R. In: Fundamentals of engineering thermodynamics: John Wiley & Sons, Inc., 2004;102.

241. Draper NR, Smith H. Applied regression analysis: John Wiley and Sons Inc, New York, 1981; 709.

242. Roveri N, Ripamonti A, Bigi A, Volpin D, Giro MG. X-ray diffraction study of bovine lens capsule collagen. Biochim Biophys Acta 1979; 576:404-408.

243. Ateshian GA, Likhitpanichkul M, Hung CT. A mixture theory analysis for passive transport in osmotic loading of cells. J Biomech 2006; 39:464-475.

244. Haider MA, Schugart RC, Setton LA, Guilak F. A mechano-chemical model for the passive swelling response of an isolated chondron under osmotic loading. Biomech Model Mechanobiol 2006; 5:160-171.

245. Heistand MR, Pedrigi RM, Dziezyc J, Humphrey JD. Redistribution of strain and curvature in the porcine anterior lens capsule following a continuous circular capsulorhexis. J Biomech 2006; 39:1537-1542.

246. Fitch JM, Mayne R, Linsenmayer TF. Developmental acquisition of basement membrane heterogeneity: type IV collagen in the avian lens capsule. J Cell Biol 1983; 97:940-943.

247. Zhang JJ, Jacob TJ. Volume regulation in the bovine lens and cataract. The involvement of chloride channels. J Clin Invest 1996; 97:971-978.

248. Candiello J, Balasubramani M, Schreiber EM et al. Biomechanical properties of native basement membranes. FEBS J 2007; 274:2897-2908.

Appendix A – Computational simulation of the iris indentation

(Experiments presented in this section were done independently by Julie E Whitcomb.)

Indentation of the iris has been used as a method to illustrate locally different mechanical properties of the tissue [182]. Figure A.1 shows results of a typical iris nano-indentation experiment. As shown in this figure, the load-displacement curve is much steeper when the posterior surface is indented (red circles) in comparison to anterior surface indentation (blue square). The results, at least intuitively, suggest that the iris is stiffer on the posterior side.

It has been established [193] that the indentation of multilayered structures yields different results depending on the arrangement of the layers. The complexity of the iris precludes a detailed model, but we can use a simple model to examine the role of the different components and examine the interactions among them.

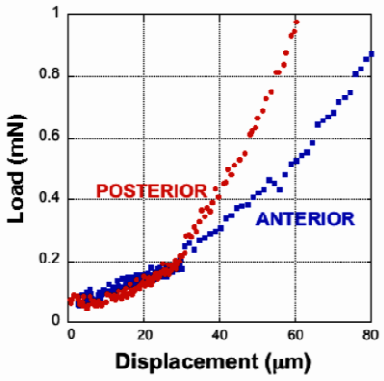

Figure A.1 Typical load-displacement curve at a constant load rate of1.0 mN/s for the anterior (square) and posterior (circle) surfaces.

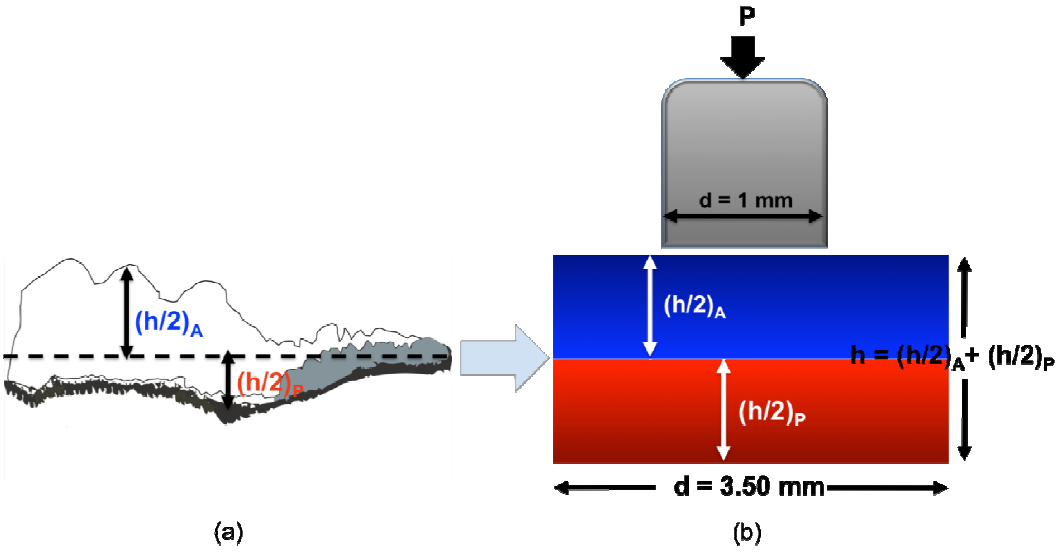

Figure A.2 (a) A cartoon cross section of the iris divided into anterior and posterior sections, which then was simplified into a (b) bilayer model. The dimensions used for the thickness were an experimental pair of indentations for the anterior (h_A) and posterior (h_P) surfaces. These values were halved and then summed, $h = (h/2)_A + (h/2)_P$, to create the respective thickness of the bilayer model, h = 692 µm. The iris section had a 3.50 mm diameter and the indenter tip a 1 mm diameter, which was displaced at the center of the section.

The detailed structure and complex shape of the iris were idealized using ABAQUS (SIMULIA, Providence, RI) into a two-layer 3.5-mm diameter cylindrical slab, as shown in Figure A.2. The slab consisted of an anterior layer (representing the stroma) and a posterior layer (representing the dilator, the pigment epithelium, and any portion of the sphincter deformed by the indentation). The sample height (h) was specified as typical experimental thickness values for paired anterior and posterior indentation tests. Both layers were assumed to be linear elastic and incompressible, and the axisymmetric indentation experiment was simulated by applying a displacement to obtain the load

values found experimentally (Figure A.1) in a region 1 mm diameter in the center of the slab (Figure A.2b).

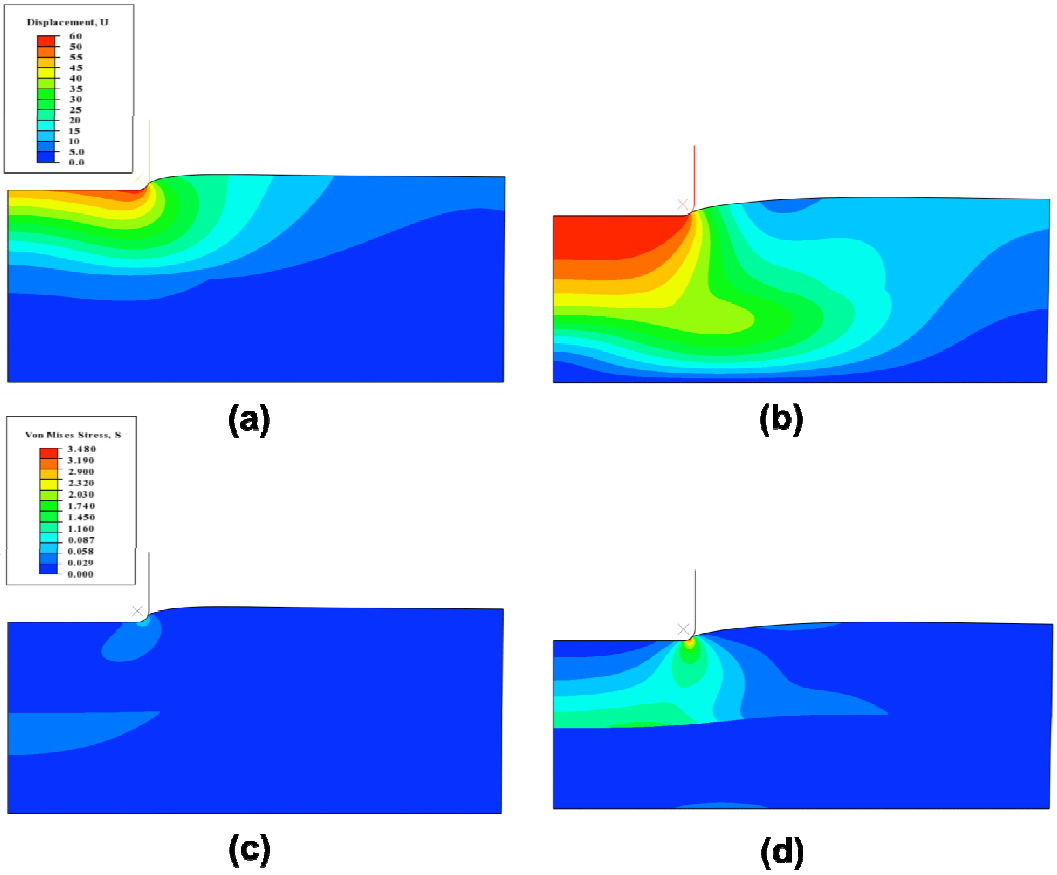

Figure A.3 Simplified bilayer model results. Displacement (a,b) and von Mises stress (c,d) fields showed marked differences between the anterior (a,c) and posterior (b,d) simulated indentations. A displacement of 60 µm was imposed for both surfaces and as expected the posterior moduli values were significantly higher than that of the anterior. The scale for displacement (U) is µm and the von Mises stress (S) is MPa.

This geometry is obviously an extreme simplification of the true iris, but it provides a model problem to explore the anterior-posterior asymmetry and illustrate the importance of indenter location. Indentation was simulated to a depth of 80 μm. The simulated indentation was performed on both surfaces, and the moduli of the anterior and posterior layers were modified to best match the experimentally calculated E values. As expected, it was found that the posterior modulus had to be significantly higher than the anterior modulus, 14.18 kPa vs. 1.87 kPa (Figure A.3). The effect of this difference is seen clearly in Figure A.4.

When the anterior surface is indented, the more compliant anterior layer experiences much more strain, and the posterior layer is largely undeformed. The result is a relatively low stress, but the support of the posterior layer amplifies the effect of the indenter on the anterior layer, producing an effective modulus that is higher than that of pure anterior layer. When the posterior layer is indented, the compliant anterior layer is compressed, reducing the effective modulus to a value below that of the posterior layer. As a result, *the asymmetry in the measured effective modulus is less pronounced than the true material asymmetry*, with a 2:1 ratio in effective modulus corresponding to a 7.6:1 ratio in the material moduli for the layers.

This result is merely illustrative and does not account for many factors in the real system, but it emphasizes the mechanical heterogeneity of the iris.

Appendix B – Mechanical Properties of the Porcine Lens Capsule

(This work was part of the paper "Elasticity of the Porcine Lens Capsule as Measured by Osmotic Swelling" by T.A. Powell, R. Amini, A. Oltean, V.A. Barnett, K.D. Dorfman, Y. Segal, and V.H. Barocas, J. Biomech. Eng., In Press)

(The error analysis of the experimental data presented in this section was performed independently by Tracy A Powell.)

Appendix B.1. Summary

The purpose of this study was to assess mechanical properties of the porcine lens capsule by using optical tracking of passive osmotic swelling. A simple model was developed accounting for the permeability of the lens fiber cells and capsule to water, the concentration of fixed charges in the fiber cells, and the capsule's resistance to the swelling of fiber cells. Fitting the model solution to experimental data provided an estimate of the elastic modulus of the lens capsule under the assumption of linear isotropic elasticity.

The calculated elastic modulus at a fixed charge density of 20 $mol \cdot m^{-3}$ was 2.0±0.5 MPa (mean ± 95% confidence interval; n=15) for 0.1% saline solution, 0.64±0.3 MPa (n=10) for 0.2% saline solution, and 0.28±0.5 MPa (n=6) for 0.5% saline solution. These values are comparable to previously reported moduli of elasticity for the porcine lens capsule at small strains (<10%), and the slight increase with hypotonicity is consistent with the nonlinear mechanical behavior of the lens capsule. Although limited by being a single measurement on a heterogeneous tissue, osmotic swelling provides a quantitative assessment of the stiffness of the lens capsule without requiring dissection

or manipulation of the lens. Thus, the new method could be useful for small animal models

Appendix B.2. Introduction

Basement membranes are planar extracellular matrices that are ubiquitous within tissues and serve roles in the organization, support, and regulation of resident cell populations. The capsule surrounding the lens of the eye is experimentally accessible accounting for its wide use as a model in studies of basement membrane biochemistry, structure, permeability and mechanics [194-198]. The lens capsule is itself a mechanical element regulating lens shape and a permeability barrier serving integrated mechanisms of ion and water transport [47,199,200]. Changes in the lens capsule have been implicated in pathological conditions including cataracts and morphologic abnormalities in genetic disorders of basement membranes [201-205].

The mechanical properties of basement membranes arise from their detailed molecular structures. While highly diverse, basement membranes are formed from a palette of constituents that includes interwoven networks of type IV collagen and laminin, in which are embedded additional specialized components [206-209]. Indeed, growing knowledge of genetic disorders of basement membranes, coupled with genetic mouse models, affords new opportunities to relate the mechanical properties of basement membranes including the lens capsule to their molecular constituents.

Our long-term goal is to use mechanical behavior to provide insight into the organization of different basement membranes by exploring how they are affected by the loss of one or more constituent proteins. The purpose of this work was to evaluate a testing method that utilizes osmotic pressure as a driving force to measure the elasticity of the porcine lens capsule. The elasticity for the porcine model has been determined through conventional mechanical techniques (summarized in Table 1.1), giving our model a basis for validity. Unlike previously employed methods of determining the elasticity of the lens capsule [48,210-212], osmotic swelling involves minimal manipulation of the lens, which is desirable when using smaller animal models, such as the mouse.

Osmotic swelling has been used to measure mechanical and transport properties of cellular and subcellular membranes in animals and plants. For example, Mela [213], used a steady-state osmotically induced swelling model to measure the elasticity of the cellular and mitochondrial membranes of the eggs of sea urchin. Mlekoday *et al*. [214] measured the permeability coefficient of human red cells by employing transient osmotically induced swelling models, neglecting the mechanical contribution of the cell membrane. Osmotic swelling and osmotic bucking tests, along with atomic force microscopy (AFM) were also used to measure the mechanical properties of the nanoengineered microstructures [215]. In plant cells, osmotic swelling has been used to study the mechanics of the cell both in presence [216] and absence [217] of the cell walls. Similar to our model for the lens capsule, plant models have been developed that

use osmotic pressure as the expansive force and mechanical pressure of the cell wall as the resistive force to cellular swelling [218,219].

Osmotic swelling of the isolated lens is also well established [201,220-222], primarily as a tool to explore lens physiology. The potential has been established for osmotic swelling as a tool to explore lens capsule stiffness [201]; however, there has been no previous osmotic-based determination of the lens capsule modulus of elasticity.

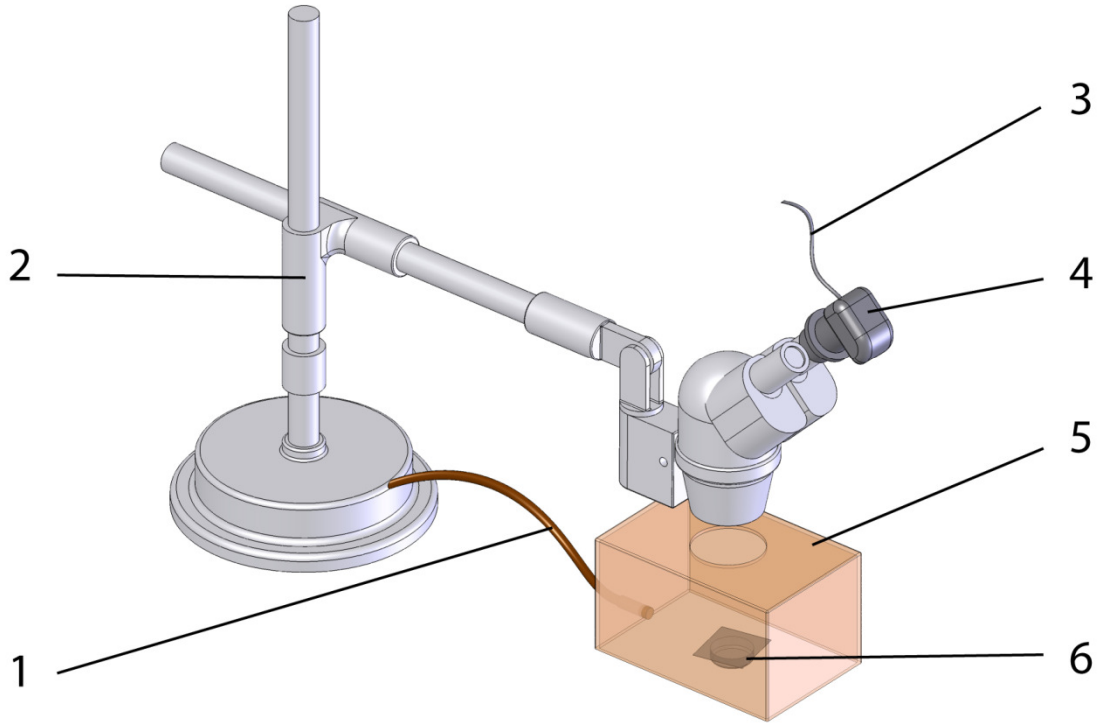

Figure B.1 Schematic of the experimental setup with (1) a fiber optic light source, (2) a dissection microscope, (3) a USB connection to the computer (not shown), (4) a digital camera, (5) a box to eliminate the ambient light, and (6) a Petri dish containing the specimen

Appendix B.3. Methodology

Appendix B.3.1. Experimental system

Porcine lenses were dissected from euthanized animals 1 to 8 hours post mortem (Visible Heart Laboratory and Experimental Surgical Services at the University of Minnesota) and transferred anterior side-down to a closed chamber containing 0.1%,

0.2%, or 0.5% (w/v) NaCl and no energy source. Figure B.1 shows the schematic of the experimental set up. Lenses thus subjected to osmotic challenge were digitally imaged every 5 to 10 minutes for 10 hours. Lens diameter was determined as the maximum distance between two points on the perimeter using MATLAB routines (Figure B.2) and lens volume calculated assuming spherical geometry.

The pixel to metric conversion was achieved using a picture of a calibrated circle taken under the experimental microscope setting for each data set. This picture was not obtained in some early experiments, so the initial lens radius for those cases (n=5) was taken to be 4600 m, the average of those measured (n=26) after the methodology was corrected. A sensitivity study on the initial radius showed that r=4500 µm or 4700 µm yielded less than 3% difference in the fitted parameters.

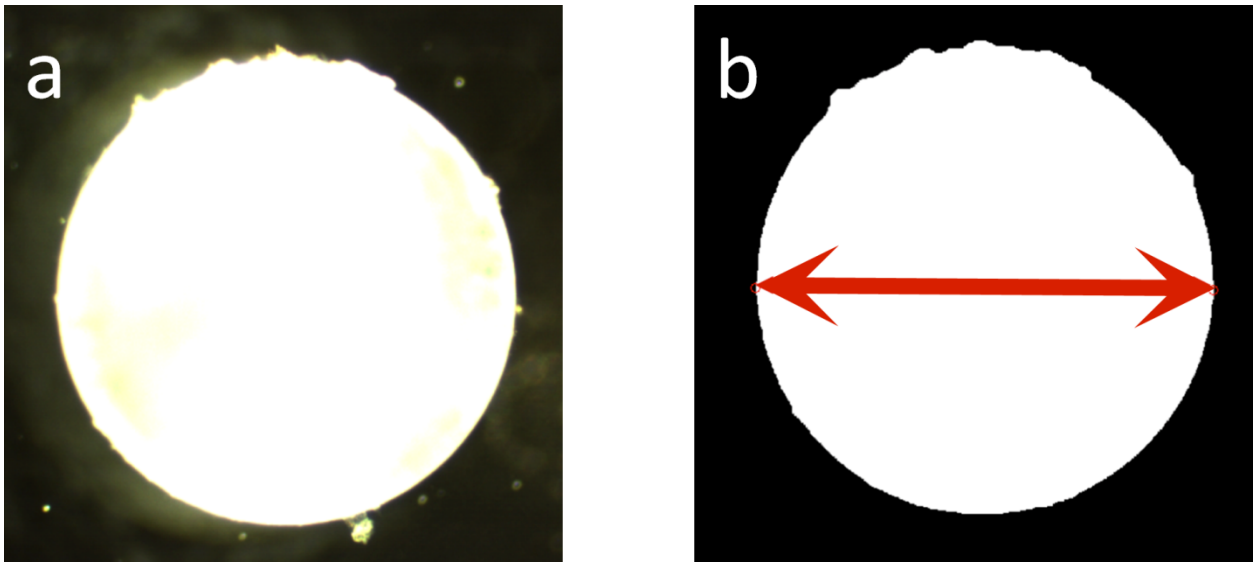

Figure B.2 Image of a lens (a) captured from camera during experiment and (b) after binomial conversion in MATLAB. Arrow indicates points from which the diameter was calculated, depicted as small circles. The radius is 4.66 mm.

Appendix B.3.2. Mathematical model

The lens capsule surrounds the cellular lens, which has three regions (Figure B.3a): a central nucleus of mature fibers, surrounded by a cortex of differentiating fibers, which are separated from the lens capsule by epithelial cells along the anterior surface [223]. Water accumulation has been shown to occur in the epithelial and underlying lens fiber regions when placed in hypotonic solutions [221,224]. A water front is created as the lens swells radially inward in layers; each layer appears to reach a fully swollen state before the next layer of fibers begins to swell [224]. This is expected, as the permeability to water molecules should increase significantly as the water content within the tissue increases. The water front in the lens capsule is similar to the immobilizing reaction modeled by Crank [225], and mathematical models have been constructed to determine the advancement of other naturally occurring fronts [226,227].

In our model, we consider passive transport only, neglecting the lens epithelial cells and dividing the lens fibers into two distinct regions. The *mushy zone* arises by osmotic swelling from the outer portion of the lens and is comprised of the swollen fibers (Figures B2.b and B2.c). The *core* represents the remaining inner portion of the cellular lens that has not been reached by the water front.

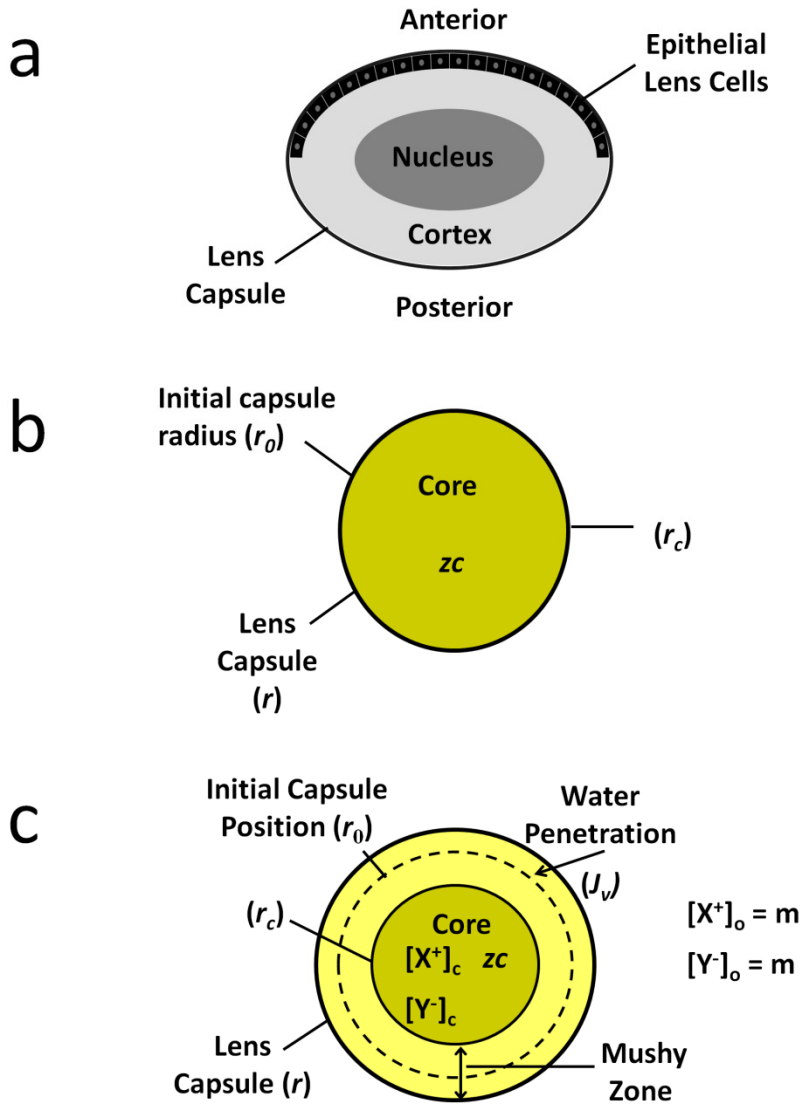

Figure B.3 (a) Anatomy of ocular lens. (b) Model schematic of ocular lens before placement in hypotonic solution and (c) after some time in hypotonic solution. The subscripts *c* and *o* refer to the core of the lens and the outside bath, respectively. Initially the lens is not swollen and a mushy zone does not exist. After placement in hypotonic solution, water penetrates the lens capsule and the lens fibers swell in layers. The swollen fibers constitute the mushy zone, and the interface between the mushy zone and the core marks the water front. The difference in osmolarity between the core and outside bath is the driving force for lens expansion, which is opposed by mechanical pressure from the stretched lens capsule

Appendix B.3.2.1. Model features

- The lens capsule is modeled as a thin, spherical shell of uniform thickness with linear elastic properties described by the mechanical theory of membranes [228] and water flux described by the Kedem-Katchalsky equation [229].

- The cellular lens is modeled as two regions: the mushy zone and the core. Water transport through the mushy zone is described empirically by Darcy's law.

- Without an energy source, transport through the lens is passive. Although multicellular, the mushy zone and core are each lumped and regarded as homogeneous.

- Two forms of charged species are present in the system. Biomacromolecules (including, for example, crystallins) have a constant fixed charge density *zc* within the core [230] and exert a Donnan effect [231]. Small ions (e.g. Na^+, Cl^-) are represented as monovalent and freely permeate [232].

- The osmotic pressure difference between the mushy zone and the outside bath is balanced by the mechanical pressure exerted by the stretching lens capsule due to the presence of a distinct water front [224].

- The osmotic pressure difference between the core and the outside bath drives water penetration and thus expansion of the mushy zone, which continues until the osmotic pressure is balanced by the mechanical pressure from the stretched lens capsule.

- The bath concentration is constant, and unstirred layer effects are neglected.

- A pressure gradient cannot be supported within the lens, resulting in an equilibrated hydrostatic pressure between the mushy zone and core:

$$P_{mushy} = P_{core} \tag{B.1}$$

Appendix B.3.2.2. Water flux from bath into the lens

The osmotic pressure difference between the core and the bath is the driving force for water movement through the lens capsule and the mushy zone. The lens increases in volume from the water influx until the osmotic pressure is balanced by the mechanical pressure exerted by the lens capsule. The solvent flux J_v is related to the spherical lens expansion:

$$J_v = \frac{1}{A}\frac{dV}{dt} = \frac{dr}{dt} \tag{B.2}$$

where V and A are the total volume and the surface area of the spherical lens, respectively. The flux across the lens capsule and the mushy zone is specified by the Kedem–Katchalsky equation [229]:

$$J_v = K_T(\Delta\pi_{c-o} - \Delta P_{c-o}) \quad \text{(B.3)}$$

where K_T is the total hydraulic conductivity of the system (mushy zone and capsule) and $\Delta\pi_{c-o}$ and ΔP_{c-o} are the osmotic and hydrostatic pressure differences between the outside bath and the core, respectively.

Appendix B.3.2.3. Hydraulic conductivity

Water must cross both the lens capsule and the mushy zone to reach the core. As the mushy zone increases in thickness, further swelling occurs more slowly due to the increased travel distance required for water to reach the core. Water moves through the lens capsule and the mushy zone in series, which results in the following expression for total hydraulic conductivity:

$$K_T = \left(\frac{1}{L_p} + \frac{r - r_c}{K_m}\right)^{-1} \quad \text{(B.4)}$$

The hydraulic conductivity of the lens capsule, L_p, is reported as velocity per unit pressure difference. The Darcy hydraulic conductivity of the mushy zone, K_m is in velocity per unit pressure gradient and is one of the two parameters regressed by the experimental data. The parameters r and r_c are the radius of the lens and the radius of the core as functions of time.

Appendix B.3.2.4. Hydrostatic pressure difference between core and bath

For a spherical isotropic, linear elastic shell with thickness h << radius r, the pressure difference across the shell is given by [228]:

$$\Delta P_{c-o} = \frac{2Eh\varepsilon}{r(1-\nu)} \tag{B.5}$$

where E is the modulus of elasticity of the lens capsule, the second parameter regressed by the experimental data; h is the thickness of the lens capsule, obtained from literature [46]; r is the radius of the lens in time, obtained from experimental data; and ν is Poisson's ratio of the lens capsule, obtained from literature [42,48]. The circumferential strain ε can be written in terms of r and the initial radius r_0, obtained from experimental data:

$$\varepsilon = \frac{2\pi r - 2\pi r_0}{2\pi r_0} = \frac{r}{r_0} - 1 \tag{B.6}$$

Substituting equation (B.6) into equation (B.5) gives

$$\Delta P_{c-o} = \frac{2Eh}{r_0(1-\nu)}\left(1 - \frac{r_0}{r}\right) \tag{B.7}$$

Appendix B.3.2.5. Osmotic pressure difference between core and bath

The osmotic pressure difference between the core and the outside bath is modeled based on the assumption of a uniform, monovalent charge distribution within the core. As previously stated, two types of ions are present in the system: one group is the fixed charges with a charge density of zc, and the second group is the free ions. Free ions are lumped into a representative positive ion $[X^+]$ and a representative negative ion $[Y^-]$, both monovalent (Figure B.3c). The subscripts c and o refer to the core of the lens and the outside bath, respectively. Considering the fixed charges to be negative [39,230], electroneutrality inside the lens requires that the free charges equilibrate with the fixed charges in the lens fiber cells [231]:

$$[X^+]_c = [Y^-]_c + zc \tag{B.8}$$

Compared to the solvent, the free charges are assumed to transport quickly enough that the Donnan equilibrium [217] is achieved instantaneously:

$$[X^+]_c[Y^-]_c = [X^+]_o[Y^-]_o \tag{B.9}$$

Since the lens volume is approximately 100-fold smaller than the bath volume, the bath concentration of ions, m, is taken to remain unchanged during the course of experiment:

$$[X^+]_o = [Y^-]_o = m \tag{B.10}$$

Equation (B.9) is then rewritten using equation (B.10):

$$[Y^-]_c[X^+]_c = m^2 \tag{B.11}$$

Substituting equation (B.8) into equation (B.11) gives

$$([Y^-]_c + zc)[Y^-]_c = m^2 \tag{B.12}$$

or

$$[Y^-]_c{}^2 + (zc)[Y^-]_c - m^2 = 0 \tag{B.13}$$

Solving Equation (B.13) for $[Y^-]_c$ gives

$$[Y^-]_c = \frac{-zc \pm \sqrt{(zc)^2 + 4m^2}}{2} \tag{B.14}$$

Concentration must be a positive real number, so the valid solution is:

$$[Y^-]_c = \frac{-zc + \sqrt{(zc)^2 + 4m^2}}{2} \tag{B.15}$$

From equations (B.11) and (B.15) $[X^+]_c$ is calculated:

$$[X^+]_c = zc + \frac{-zc + \sqrt{(zc)^2 + 4m^2}}{2} = \frac{zc + \sqrt{(zc)^2 + 4m^2}}{2} \tag{B.16}$$

The total concentration of the free charges in the core C_c is the sum of the positive and negative free charges:

$$C_c = [Y^-]_c + [X^+]_c = 2\frac{\sqrt{(zc)^2+4m^2}}{2} = 2\sqrt{\frac{(zc)^2}{4} + m^2} \quad \text{(B.17)}$$

Similarly, the concentration of the free charges in the hypotonic bath solution C_o, with equation (B.9), gives

$$C_o = [X^+]_o + [Y^-]_o = 2m \quad \text{(B.18)}$$

The difference in concentration between the core and the bath solution ΔC is

$$\Delta C_{c-o} = C_c - C_o \quad \text{(B.19)}$$

Substituting equations (B.18) and (B.17) into equation (B.19) gives:

$$\Delta C_{c-o} = 2\sqrt{\frac{(zc)^2}{4} + m^2} - 2m \quad \text{(B.20)}$$

The osmotic pressure is calculated from the Van't Hoff relation [233]:

$$\Delta\pi = RT\Delta C \quad \text{(B.21)}$$

where R is the universal gas constant and T (=293 K) is the ambient temperature. Equation (B.21) is then rewritten using equation (B.20):

$$\Delta\pi_{c-o} = 2RT\left(\sqrt{\frac{(zc)^2}{4} + m^2} - m\right) \quad \text{(B.22)}$$

Appendix B.3.2.6. Derivation of osmotic pressure difference between mushy zone and bath

The fixed charges are associated with proteins and biomacromolecules (including, for example, crystallins) within the lens fiber cells that cannot cross the fiber cell membranes. As the fractional volume of water in the lens fibers increases, the concentration of the fixed charges decreases. The concentration of fixed charges in the mushy zone $zc_m(t)$ can be related to the initial fixed charge density zc, the change in volume of the mushy zone $V_m(t)$, and the volume which the lens cells in the mushy zone occupied before they became swollen $V_{m0}(t)$ (Figure B3; volumes associated with corresponding radii). Lens cells from the core are recruited to the mushy zone throughout swelling, which gives rise to the time dependence of the initial volume of the lens cells in the mushy zone $V_{m0}(t)$.

The following values change with time: the volume of the core $V_c(t)$, the volume of the mushy zone $V_m(t)$, the overall volume of the lens $V(t)$, and the volume which the lens cells in the mushy zone occupied before they became swollen $V_{m0}(t)$. V_0 is the initial volume of the lens before swelling, which is obtained from experimental data assuming spherical geometry. As more fibers are incorporated into the mushy zone from the core region, $V_{m0}(t)$ increases and $V_c(t)$ decreases. By definition, the transformation of fibers from the core to the mushy zone requires an increase in water

content, which increases the volume of the lens $V(t)$. The increase in volume occurs in the mushy zone, and thus $V_m(t)$, increases.

Choosing a specific point in time and assigning the total number of fixed charges within the mushy zone to $N(t)$:

$$zc_m(t) = \frac{N(t)}{V_m(t)} \tag{B.23}$$

Considering the lens fibers within the mushy zone at this point in time, before swelling began, the same fibers had a charge density of:

$$zc = \frac{N(t)}{V_{m0}(t)} \tag{B.24}$$

The number of charges has not changed within the specific zone because the number of lens fiber cells has not changed. Combining equation (B.23) and (B.24) gives:

$$\frac{zc_m(t)}{zc} = \frac{V_{m0}(t)}{V_m(t)} \tag{B.25}$$

or

$$zc_m(t) = zc\,\frac{V_{m0}(t)}{V_m(t)} \tag{B.26}$$

From section B.3.2.5, the concentration of ions within the core is:

$$C_c = [Y^-]_c + [X^+]_c = 2\,\frac{\sqrt{(zc)^2+4m^2}}{2} = 2\sqrt{\frac{(zc)^2}{4} + m^2} \tag{B.17}$$

The fixed charge density zc in the core is the concentration before swelling, which is the *in vivo* concentration. The concentration of ions within the mushy zone is give by the following equation, where $zc_M(t)$ is used in place of zc:

$$C_m = 2\sqrt{\frac{\left(zc_m(t)\right)^2}{4} + m^2} \tag{B.27}$$

Incorporating equation (B.26) into equation (B.27) gives

$$C_m = 2\sqrt{\left(\frac{V_{m0}(t)}{V_m(t)}\right)^2 \frac{(zc)^2}{4} + m^2} \tag{B.28}$$

In combination with equation (B.18):

$$C_{m-o} = 2\sqrt{\left(\frac{V_{m0}(t)}{V_m(t)}\right)^2 \frac{(zc)^2}{4} + m^2} - 2m \tag{B.29}$$

From the Van't Hoff relation (equation (B.21)), the osmotic pressure between the mushy zone and the bath is:

$$\Delta\pi_{m-o} = 2RT\left(\sqrt{\left(\frac{V_{m0}(t)}{V_m(t)}\right)^2 \frac{(zc)^2}{4} + m^2} - m\right) \tag{B.30}$$

Using the assumption that the lens is spherical, the geometry of the system (Figure B.4) gives:

$$V_c = V - V_m = V_0 - V_{m0} \tag{B.31}$$

$$V_{m0} = V_0 - V_c \tag{B.32}$$

$$V_m = V - V_c \tag{B.33}$$

$$\frac{V_{m0}}{V_m} = \frac{V_0 - V_c}{V - V_c} \tag{B.34}$$

Using the spherical relationship between volume and radius, equation (B.34) gives:

$$\frac{V_{m0}}{V_m} = \frac{r_0^3 - r_c^3}{r^3 - r_c^3} \tag{B.35}$$

Combining equations (B.30) and (B.35) gives

$$\Delta\pi_{m-o} = 2RT\left(\sqrt{m^2 + \frac{1}{4}\left(\frac{r_0^3 - r_c^3}{r^3 - r_c^3}\right)^2 (zc)^2} - m\right) \tag{B.36}$$

Appendix B.3.2.7. Radius of core with time

The change in core radius with time is needed for the computation of the total hydraulic conductivity. The osmolarity of the mushy zone never reaches that of the outside bath concentration due to the resistance to expansion of the lens capsule. The equilibrium of the hydrostatic and osmotic pressures between the mushy zone and the hypotonic solution gives:

$$\Delta\pi_{m-o} = \Delta P_{m-o} \tag{B.37}$$

Equation (B.1) can be incorporated into equation (B.7) to give the pressure difference between the bath and the mushy zone:

$$\Delta P_{m-o} = \frac{2Eh}{r_0(1-\nu)}\left(1-\frac{r_0}{r}\right) \tag{B.38}$$

Using equations (B.38) and (B.36), we can rewrite equation (B.37):

$$\frac{2Eh}{r_0(1-\nu)}\left(1-\frac{r_0}{r}\right) = 2RT\left(\sqrt{m^2+\frac{1}{4}\left(\frac{r_0^3-r_c^3}{r^3-r_c^3}\right)^2(zc)^2}-m\right) \tag{B.39}$$

Solving for the radius of the core, r_c gives

$$r_c = \sqrt[3]{\frac{r_0^3-\not{f}(E,r,zc)r^3}{1-\not{f}(E,r,zc)}} \tag{B.40}$$

where

$$\not{f}(E,r,zc) = \frac{2}{zc}\sqrt{\left[\frac{Eh}{r_0(1-\nu)RT}\left(1-\frac{r_0}{r}\right)+m\right]^2-m^2} \tag{B.41}$$

Appendix B.3.2.8. Governing equation of the system and numerical methods

Substituting equations (B.2), (B.4), (B.7), (B.22), and (B.40) into equation (B.3) yields a single governing ODE:

$$\frac{dr}{dt} = \left(\frac{1}{L_p}+\frac{r-\sqrt[3]{\frac{r_0^3-\not{f}(E,r,zc)r^3}{1-\not{f}(E,r,zc)}}}{K_m}\right)^{-1}\left[2RT\left(\sqrt{m^2+\frac{1}{4}(zc)^2}-m\right)-\frac{2Eh}{r_0(1-\nu)}\left(1-\frac{r_0}{r}\right)\right] \tag{B.42}$$

The numerical solution to equation (B.42) was obtained using the MATLAB *ode23s* routine [234]. The parameter values used in the modeling are listed in Table B.1. Recognizing that the thickness of the lens capsule is not uniform [235-237], we take an average thickness h of 58 μm determined for the anterior surface [46]. We investigate two values of the fixed charge density zc-10 and 20 mM-determined in bovine lens [230]. The values of the elastic modulus, E, and Darcy conductivity of mushy zone, K_m, were chosen to minimize the sum of squared error between the simulated and experimental r vs. t data using a MATLAB *fminsearch* routine [238]. Peirce's criterion [239] was used to evaluate the elastic modulus at each bath concentration.

Table B.1 Physical parameters used in the model

Parameter	Definition	Value	Unit	Reference
h	Capsule thickness	58	μm	[46]
L_P	Capsule hydraulic conductivity	7.5×10^{-11}	$m \cdot Pa^{-1} \cdot s^{-1}$	[204]
ν	Poisson's ratio	0.47		[42,48]
R	Universal gas constant	8.314	$m^3 \cdot Pa \cdot K^{-1} \cdot mol^{-1}$	[240]
T	Ambient temperature	293	K	

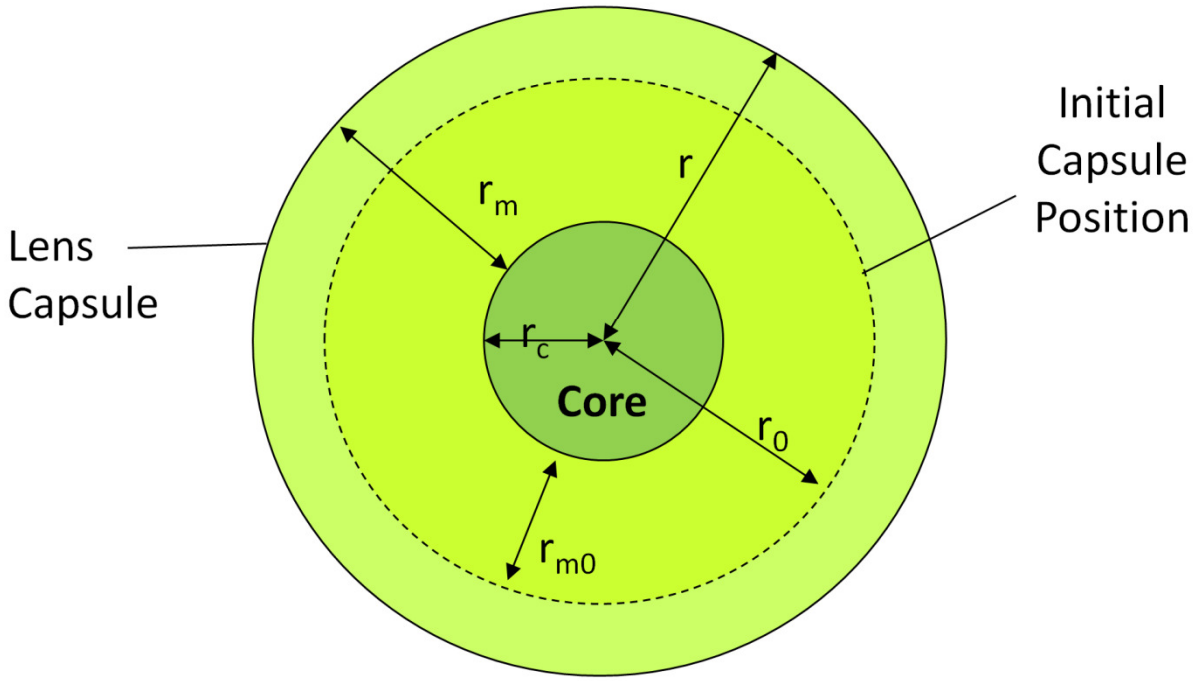

Figure B.4 Model volume definitions

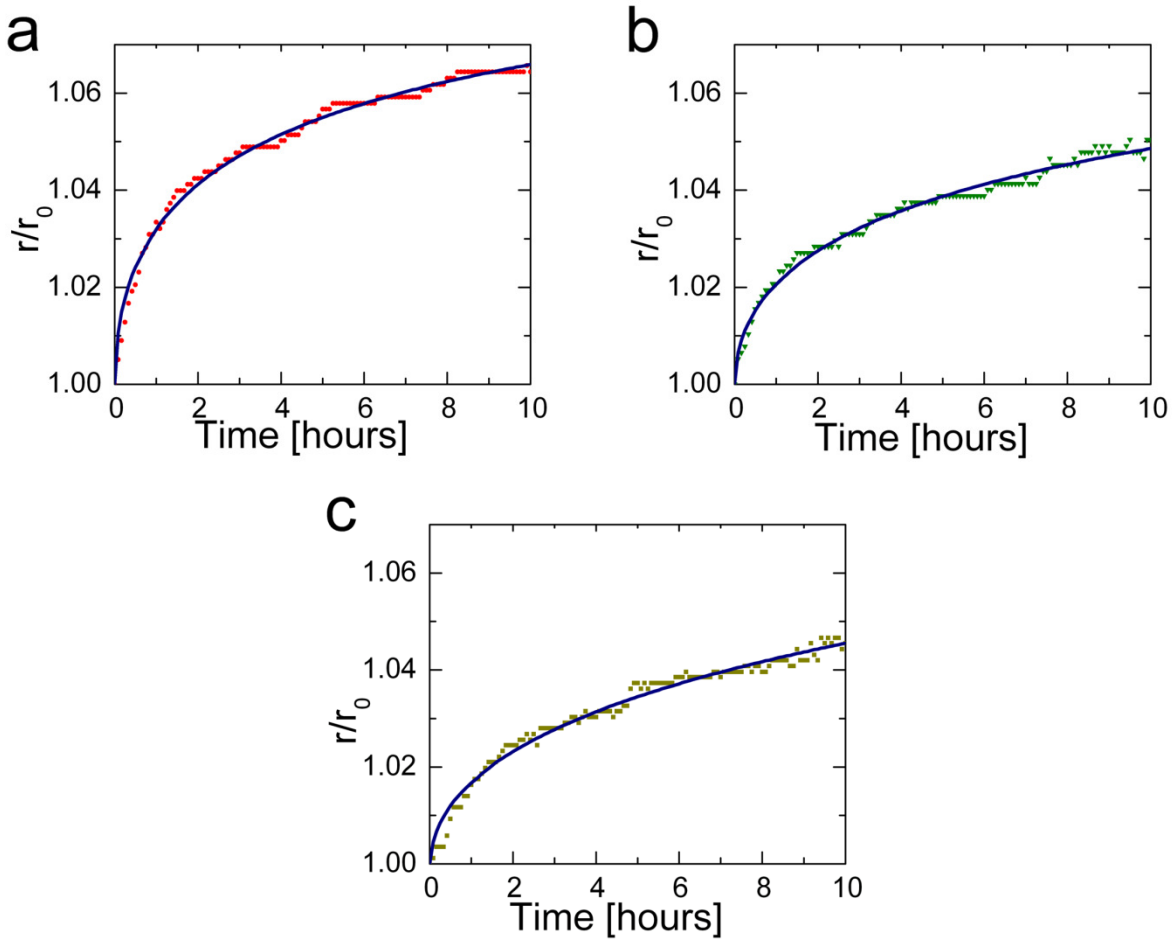

Figure B.5 Mathematical model (solid lines) fitted to the experimental data (symbols) for lens expansion in (a) 0.1%, (b) 0.2%, and (c) 0.5% NaCl with the fixed charge density, *zc*, set at 20 mol·m^{-3}. Discrete steps in the experimental data were caused by the limit of measurement resolution.

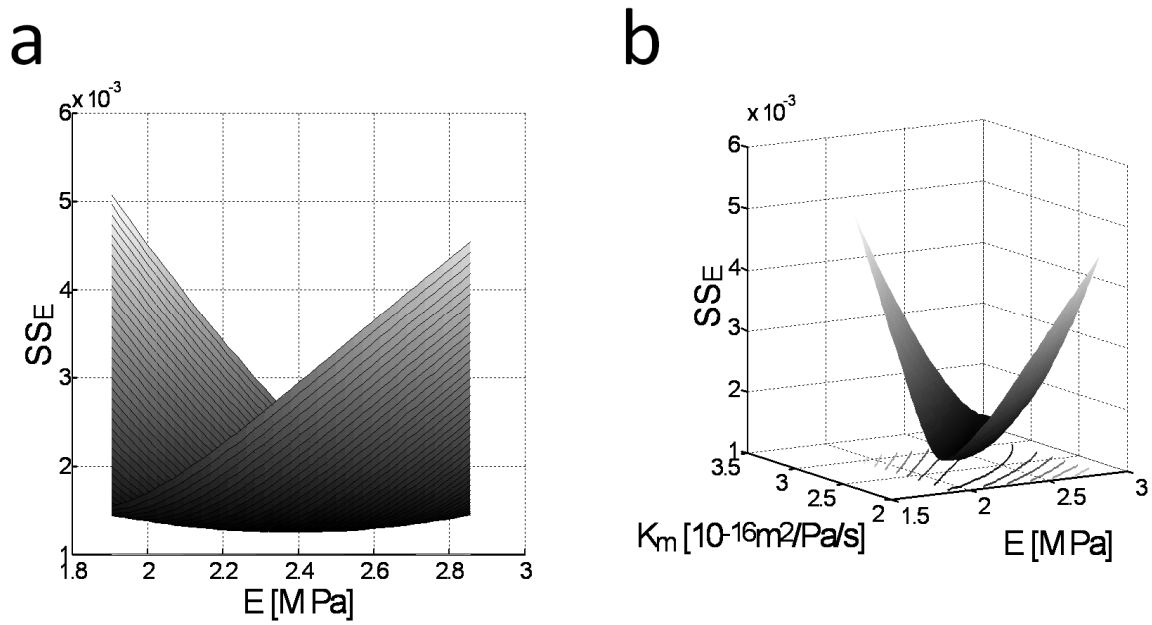

Figure B.6 Sum of squared error (SSE) (a) plotted vs. modulus of elasticity of the lens capsule, E, and (b) plotted vs. E and Darcy conductivity of the mushy zone, K_m. A shallow trough lies along the line E= K_m+.02, with units of MPa and 10^{-16} $m^2 \cdot Pa^{-1} \cdot s^{-1}$ for E and K_m respectively. Results are from a 0.1% NaCl bath and based on *zc* =20 $mol \cdot m^{-3}$.

Appendix B.4. Results

Figure B.5 shows the results of three representative experiments using bath compositions of 0.1, 0.2, and 0.5% NaCl with their numerical solution to equation B.42. The symbols represent experimental data, and the solid lines represent the numerical solutions, with modulus of elasticity, E, and Darcy conductivity of the mushy zone, K_m, as fitting parameters for each data set independently; the fixed charge density, *zc*, was set at 20 mol·m^{-3}.

The average initial radius of the lens was 4700±110 μm (mean ± 95% confidence interval) n=12 for the experiments with 0.1% saline bath concentration, 4500±120 μm n=9 for the 0.2% saline bath, and 4450±150 μm n=5 for the 0.5% saline bath. There was no significant difference among the initial lens radii of the three groups of experiments (p=0.38 by analysis of variance, ANOVA). Rotation of a single image (from -15° to 15° with 5° steps) and subsequent measurement of the equatorial diameter produced less than 1% error.

Typical sum-of-squared error (SSE) vs. E and K_m plots are given in Figure B.6. When E is increased and K_m decreased (or vice versa), the error rises rapidly, but if E and K_m both increase (or decrease), there is relatively little change in the error, as seen by the highly elliptical contours in Figure B.6a and the shallow trough in Figure B.5b. For a two-parameter model, a reasonable estimate of the 95% confidence ellipse on the fitted parameters is that $SSE_{95\%}$=1.17 SSE_{min} [241]. For the plot in Figure B.6b, SSE_{min}=.00125, giving $SSE_{95\%}$=.00146. The axes of the confidence ellipse do not coincide

with the E and K_m axes. The K_m that produced minimum error at each value of E was plotted against E (graph not shown), resulting in a nearly linear line with slope 1. This line plots the valley of the trough for the error contour graph in Figure B.6b. With an intercept of 0.2 and error determined from the 95% confidence ellipse, the rotated coordinates of the ellipse correspond to the following equations:

$$E - K = -0.2 \ +/- \ 0.05E_{min}, \text{ where } E_{min} = 2.38 \text{ MPa}$$

$$K - E = 0.2 \ +/- \ 0.26K_{min}, \text{ where } K_{min} = 2.56 \times 10^{-16} \text{ m}^2\cdot\text{Pa}^{-1}\cdot\text{s}^{-1}$$

As can be seen in Figure B.6b, the confidence ellipses have a long direction, yielding fairly large confidence intervals (roughly +/- 25%) when E and K_m are both allowed to vary. Thus we expect that the estimated values are within 25-30% of the true value. We observe that if E or K_m were known from some other measurement, the confidence intervals would be tightened considerably.

One data point was removed as an outlier from the 0.5% saline bath concentration dataset at zc=20 mol·m^{-3}. The average elastic modulus of the lens capsule at zc=20 mol·m^{-3} was 2.0±0.5 MPa (mean ± 95% confidence interval; n=15) for 0.1% saline solution, 0.64±0.3 MPa (n=10) for 0.2% saline solution, and 0.28±0.5 MPa (n=6) for 0.5% saline solution. For zc=10 mol·m^{-3}, the average elastic modulus was 0.58±0.1 MPa (n=15) for 0.1% saline solution, 0.20±0.08 MPa (n=10) for 0.2% saline solution, and 0.24±0.02 MPa (n=7) for 0.5% saline solution. The data are shown in Figure B.7 with reported literature values of the porcine lens elastic modulus for

comparison. It is noted that the Krag and Andreasson value is a secant modulus at 10% uniaxial strain (calculated from table III [210]) and may not be directly comparable to our measurement, which is primarily biaxial.

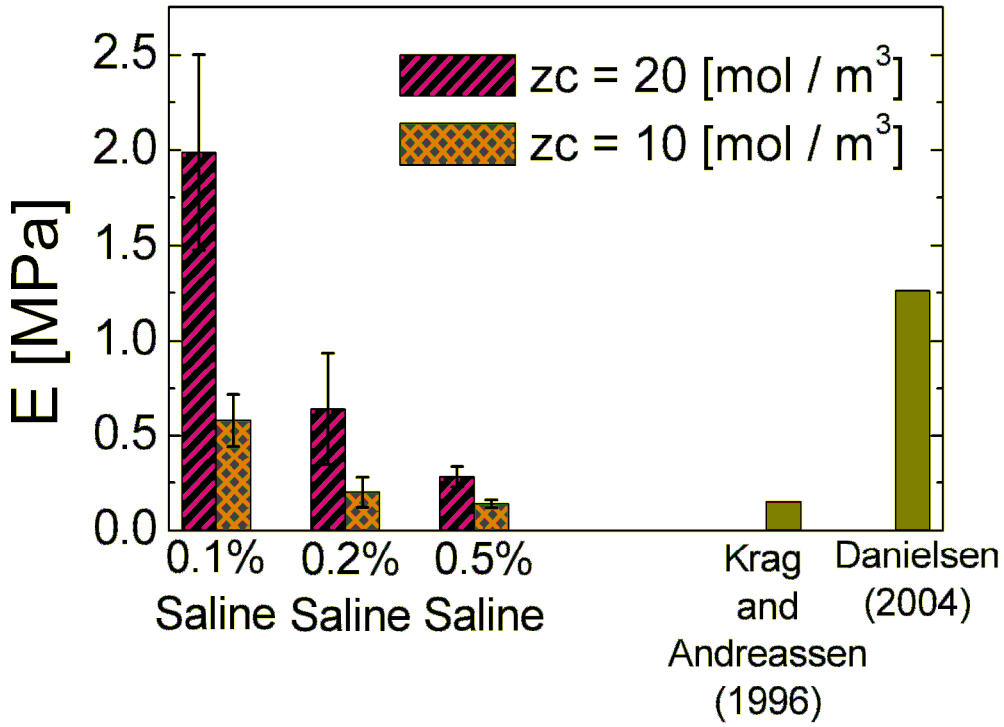

Figure B.7 Modulus of elasticity of the porcine lens capsule calculated in the current work and reported in the literature. Error bars are 95% confidence intervals.

Appendix B.5. Discussion

The osmotic swelling method developed here provides a quantitative assessment of the lens capsule modulus of elasticity without requiring dissection. Unlike traditional mechanical techniques, the minimal manipulation allows osmotic swelling to be extended to small animal models such as the mouse. The elastic modulus estimates are made at small strains (<10%), which are physiologically relevant, as this is where accommodation occurs [235].

The elastic modulus determined through the osmotic swelling model is comparable to previously reported values. The secant modulus calculated from Table III of Krag and Andreassen [210] was obtained from uniaxial extension tests of pre-strained capsule rings while the elasticity calculated by our model and by Danielsen [49], who utilized Fisher's biaxial method of inflation [48], came from multiaxial extension tests. Although the elasticity from Krag and Andreassen shown in Figure B.7 is calculated from pre-strained capsular rings, the alignment of the fibers is still likely to affect the elasticity. Under uniaxial loading, the collagen IV network initially straightens in the low strain region (<10%). Under biaxial loads, however, the collagen IV network does not experience the initial straightening [208]. X-ray diffraction has shown networks of randomly oriented collagen fibers in unstretched, air-dried bovine lens capsules and has demonstrated the reorientation of fibers parallel to the direction of applied stress in stretched collagen networks [242]. The effect of loading type has been shown with the human lens capsule. Fisher [48] reported values of 3-6 MPa using inflation, as

compared to 0.3-2.3 MPa measured by Krag and Andreassen 2003 [45] using uniaxial ring-pulling. Therefore, the higher modulus observed by our model and Danielson as compared to Krag and Andreassen is expected.

It is further noted that our data show a slight increase in modulus with hypotonicity. This is consistent with nonlinear material response, which is also expected given the nonlinear mechanical behavior of the tissue [210].

The simplification of the transport and thermodynamics within the lens to a lumped, well-mixed system containing only fixed charge and monovalent ions was made to simplify analysis of the data and minimize the number of empirical parameters, but it could lead to incorrect results. The validity of the lumped model can be assessed by calculating the characteristic diffusion time. For small ions, the diffusion coefficient is expected to be on the order of 0.001 $mm^2 \cdot s^{-1}$ [232]. Early in the experiment, the mushy zone is relatively thin (~ 0.5 mm at t ~ 2 hours), and the diffusion time scale is short (~ 5 min). At the end of the experiment, the mushy zone thickness is approximately 1.5 mm, which corresponds to a diffusion time scale of 40 min, which is rapid compared to the 10-hr experiment but long enough to be an issue.

In light of this concern, the following analysis is made. Since the volume change is not very large (~20% for 7% radial expansion), the chemical environment within the lens (i.e., the osmotic pressure driving water into the lens) does not change dramatically during the experiment. An increase in elastic modulus, E, reduces the equilibrium expansion of the lens, shifting the radius vs. time curve down. An increase in

permeability of the mushy zone, K_m, allows the system to equilibrate more quickly due to increased water mobility, shifting the radius vs. time curve to the left. Thus, the net effect of the combined increases in E and K_m is small, as seen in Figure B.5. It would be possible to separate the two parameters more effectively if the experiment were run to equilibrium, but we found that the tissue began to deteriorate after 10 hours, so we were not able to explore longer times. For a smaller lens, the equilibration time might be faster, so the method may work better in, e.g., the mouse.

The value of the fixed charge density zc was held constant, and two values were analyzed. Since our goal is to quantify the change in the elastic modulus as the composition of the basement membrane is altered through genetic manipulation, this model is appropriate for the intended use regardless of the chosen zc. It is observed, however, that an accurate measurement of the elastic modulus cannot be determined without knowing the value of the fixed charge density. Even if the fixed charge density were known, the electrochemistry of the lens is assuredly more subtle than a collection of only fixed charges and monovalent ions. We therefore reiterate that the modulus values calculated from our analysis of a swelling experiment are better suited to comparison between different lens capsules than to specific quantitative application. If more information about the charged species and the transport properties within the lens were to become available, a distributed model following those of Ateshian [243] and Haider [244] could be developed. Heistand *et al.* [47] have developed a novel method of determining multiaxial mechanical behavior of the lens capsule. While their

protocol can be used to determine more accurate and regional measurements of the modulus of elasticity, it is difficult to extend to the mouse lens due to its size.

There are many aspects of lens geometry and properties that are not captured by the approach we describe. These include variation in radius of curvature [245], capsule thickness [237], and collagen content [246] from the anterior to the posterior of the lens. Some insight into this problem could be drawn by mounting the lens so that a sagittal rather than a coronal plane is imaged, an experiment that should be possible with our system. It is also noted that no evidence of active volume control [247] was observed, most likely due to the lack of energy source and low temperature. The good reproducibility of the experiment and agreement with published data acquired from standard tests suggest that the approach is providing accurate results, but it is always possible that multiple simplifications/errors cancelled out to produce a correct result.

In spite of the concerns raised here, osmotic swelling has the potential to quantify changes in lens capsule mechanical properties in the mouse lens, providing access to the genetic manipulability of the mouse. Traditional test methods [47,48,210] require isolation and manipulation of the sample that will be complicated, if not impossible, to achieve with the mouse lens. Atomic force microscopy (AFM) has recently been applied to the mouse lens capsule basement membrane [248], but AFM involves more difficult isolation and a highly complex deformation (involving compression, tension, shear, and finite-thickness effects simultaneously). Osmotic

swelling offers a simpler approach, and this preliminary study suggests that it is a feasible method to assess prefailure lens capsule elasticity at small strains (<10%).